AD/A-001 570

THE IVORY CORAL PROGRAM ON IONOSPHERIC MODIFICATION

M. R. VanderLind

Stanford Research Institute

Prepared for:

Office of Naval Research
Defense Advanced Research Projects Agency

September 1974

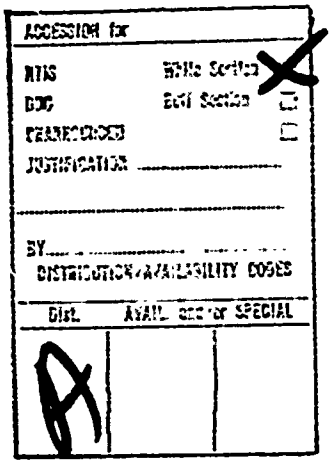

The views and conclusions contained in this document are those of the authors and should not be interpreted as necessarily representing the official policies, either expressed or implied, of the Defense Advanced Research Projects Agency, the Department of Commerce, or the U.S. Government.

REPORT DOCUMENTATION PAGE

READ INSTRUCTIONS BEFORE COMPLETING FORM

1. REPORT NUMBER	2. GOVT ACCESSION NO.	3. RECIPIENT'S CATALOG NUMBER

4. TITLE (and Subtitle)

TECHNICAL SUMMARY OF THE IVORY CORAL PROGRAM ON IONOSPHERIC MODIFICATION

5. TYPE OF REPORT & PERIOD COVERED

Technical Summary
Covering the period
October 1970 to December 1973

6. PERFORMING ORG. REPORT NUMBER

Technical Summary
SRI Project 8727

7. AUTHOR(s)

Compiled by M. R. VanderLind
(Battelle Columbus Laboratories)

8. CONTRACT OR GRANT NUMBER(s)

Contract N00014-70-C-0413

9. PERFORMING ORGANIZATION NAME AND ADDRESS

Stanford Research Institute
Menlo Park, California 94025

10. PROGRAM ELEMENT, PROJECT, TASK AREA & WORK UNIT NUMBERS

ARPA Order 1656
ONR NR 088-047

11. CONTROLLING OFFICE NAME AND ADDRESS

U.S. Department of Defense
Defense Advanced Research Projects Agency
Arlington, Virginia 22209

12. REPORT DATE

September 1974

13. NO OF PAGES

~~151~~ 149

14. MONITORING AGENCY NAME & ADDRESS (if diff. from Controlling Office)

Office of Naval Research, Code 464
Arlington, Virginia 22217

15. SECURITY CLASS. (of this report)

Unclassified

15a. DECLASSIFICATION/DOWNGRADING SCHEDULE

N/A

16. DISTRIBUTION STATEMENT (of this report)

Approved for public release; distribution unlimited

17. DISTRIBUTION STATEMENT (of the abstract entered in Block 20, if different from report)

18. SUPPLEMENTARY NOTES

19. KEY WORDS (Continue on reverse side if necessary and identify by block number)

Ionospheric modification
Ionospheric heating
Ionospheric irregularities
Ionospheric scatter propagation
Field-aligned scattering
Optical-emission modifications
Electron-density fluctuations
Plasma waves
Ion acoustic waves
Plasma instabilities

20. ABSTRACT (Continue on reverse side if necessary and identify by block number)

The IVORY CORAL program is an outgrowth of early ARPA over-the-horizon radar research. The primary objectives of the IVORY CORAL program were to modify the ionosphere in a controllable manner, to determine the characteristics of the modified volume, and to develop and verify models of the modified volume.

The results of the IVORY CORAL program clearly demonstrate that the ionosphere can be modified and characterized when illuminated with reasonable RF power

19. KEY WORDS (Continued)

20 ABSTRACT (Continued)

densities. Changes in the ionospheric electron density, electron temperature, and collision frequency have been observed and are reasonably well understood. Structuring of the modified volume has been observed using a variety of radio scattering and scintillation methods. An understanding of some of the mechanisms responsible for the structuring has been developed, although areas of uncertainty remain. Of particular interest are the theoretical descriptions of incoherent backscatter observations in terms of the excitation of plasma instabilities, and the observation of strong, field-aligned scattering at E- and F-region altitudes, for which a theoretical understanding is just now developing. Significant modifications of airglow have also been observed and some theoretical explanations have been offered.

The variety and richness of the scientific results of the IVORY CORAL program clearly demonstrate the validity of the concept of RF modification and characterization of the ionosphere. Numerous phenomena were observed and pursued in varying levels of detail. In some cases adequate theories were developed, while in other cases a full understanding does not yet exist. Numerous areas for fruitful experimental and theoretical work have been identified. In terms of technical accomplishment, the IVORY CORAL program stands as a milestone in ionospheric research, the full implications of which have not yet been realized.

A TECHNICAL SUMMARY OF THE

IVORY CORAL

PROGRAM OF IONOSPHERIC MODIFICATION

September 1974

Compiled by:

M. R. VanderLind
Battelle Columbus Laboratories
Columbus, Ohio

This research was sponsored by the Defense Advanced Research Projects Agency of the Department of Defense and was monitored by the Office of Naval Research under Contract No. N00014-70-C-0413 (NR 088-047); ARPA Order 1656, Program Code 4E30.

Sponsored by:

U.S. DEPARTMENT OF DEFENSE
DEFENSE ADVANCED RESEARCH PROJECTS AGENCY
ARPA ORDER NO. 1656

In Cooperation with:

U.S. DEPARTMENT OF COMMERCE
OFFICE OF TELECOMMUNICATIONS
INSTITUTE FOR TELECOMMUNICATION SCIENCES

Published by:

STANFORD RESEARCH INSTITUTE
MENLO PARK, CALIFORNIA

Copy No. 17

ABSTRACT

The IVORY CORAL program is an outgrowth of early ARPA over-the-horizon radar research. The primary objectives of the IVORY CORAL program were to modify the ionosphere in a controllable manner, to determine the characteristics of the modified volume, and to develop and verify models of the modified volume.

The results of the IVORY CORAL program clearly demonstrate that the ionosphere can be modified and characterized when illuminated with reasonable RF power densities. Changes in the ionospheric electron density, electron temperature, and collision frequency have been observed and are reasonably well understood. Structuring of the modified volume has been observed using a variety of radio scattering and scintillation methods. An understanding of some of the mechanisms responsible for the structuring has been developed, although areas of uncertainty remain. Of particular interest are the theoretical descriptions of incoherent backscatter observations in terms of the excitation of plasma instabilities, and the observation of strong, field-aligned scattering at E- and F-region altitudes, for which a theoretical understanding is just now developing. Significant modifications of airglow have also been observed and some theoretical explanations have been offered.

The variety and richness of the scientific results of the IVORY CORAL program clearly demonstrate the validity of the concept of RF modification and characterization of the ionosphere. Numerous phenomena were observed and pursued in varying levels of detail. In some cases adequate theories were developed, while in other cases a full understanding does not yet exist. Numerous areas for fruitful experimental and theoretical work have

been identified. In terms of technical accomplishment, the IVORY CORAL program stands as a milestone in ionospheric research, the full implications of which have not yet been realized.

CONTENTS

ILLUSTRATIONS

TABLES

FOREWORD

This report contains a summary of the technical results of the IVORY CORAL program. The program was managed by A. Van Every for the Defense Advanced Research Projects Agency in cooperation with W. F. Utlaut and the Department of Commerce/Institute for Telecommunication Sciences.

M. R. VanderLind (Battelle--Columbus Laboratories) compiled and integrated this summary report from the contributions of a number of the researchers who were associated with the program. The major authors and their contributions to the report are as follows:

- E. M. Allen and G. D. Thome (Raytheon Company) provided the description of the results of the HF phased-array experiments.
- D. Arnush (TRW Systems) provided the descriptions of the theoretical and experimental works associated with the Quiescent Ionospheric Plasma Simulator (QUIPS).
- S. A. Bowhill (Aeronomy Corporation) provided the descriptions of the experimental and analytical results of the satellite transmission experiments as well as some of the modeling analysis.
- P. A. Fialer (Stanford Research Institute) provided descriptions of experimental data on field-aligned scattering and ion-acoustic wave scattering as well as the general classification of experimental results.
- W. E. Gordon (Rice University) provided the descriptions of the work done in support of the IVORY CORAL program at the Arecibo Observatory.
- J. C. Haslett (National Oceanic and Atmospheric Administration) provided the descriptions of the theoretical and experimental work on the airglow changes produced by RF ionospheric modifications.

- G. Meltz (Raytheon Company), and F. W. Perkins (Princeton University) provided most of the descriptions of the theoretical work that was undertaken in support of the IVORY CORAL program.
- J. Minkoff (Riverside Research Institute) provided descriptions of the experimental data obtained with the VHF and UHF radars at the White Sands Missile Range as well as some of the field-aligned scattering analysis.
- P. B. Rao and G. D. Thome (Raytheon Company) provided the description of the modeling work performed in support of the IVORY CORAL program.
- L. E. Sweeney, Jr. (Stanford Research Institute) provided the consolidated description of the results of the experimental program and, in addition, the description of the scattering-model verification experiments.
- W. F. Utlaut (Institute for Telecommunication Sciences) provided descriptions of ionosonde and other measurements performed in the vicinity of the Boulder, Colorado facility.

Others too numerous to mention here have provided material used in this report. Their names will be found in the text and references.

I INTRODUCTION

The ionosphere has been investigated by scientists for many years. The early investigations were performed to promote understanding of the physics of the ionosphere. As this understanding progressed to the point where models of the gross characteristics of the ambient ionosphere were proposed and eventually verified, certain potential uses began to emerge. Early work sponsored by ARPA in this area advanced the state of the art to the point where practical uses of the ionosphere could be enhanced or degraded. One of these applications is over-the-horizon (OTH) radar. The IVORY CORAL program was an outgrowth of the early ARPA OTH research. The IVORY CORAL effort involved RF modification of the ionosphere and characterization of the modifications produced.

RF ionospheric modification was first theorized by Gurevich and Farley in 1967. Early in 1970 Meltz and LeLevier calculated electron density and temperature changes as a result of RF heating of the F2 layer of the ionosphere. This modification was verified in April 1970 by Utlaut at Platteville, and in October 1970 by Gordon at Arecibo. As a result of these successes, the IVORY CORAL program was expanded to develop an understanding of the generation and characterization of this modified volume. As the understanding and characterization of the modified volume developed, the technology was transferred to more user-oriented groups.

A. Program Objectives

The primary objectives of the IVORY CORAL program were as follows:

- Modify the ionosphere in a controllable manner. The controlled and reproducible generation of an RF modified volume in the ionosphere is required to perform systematic

experiments to determine its characteristics. In addition, eventual usefulness of the concept depends, in part, on its reproducibility.

- Determine the characteristics of the modified volume. The major physical characteristics of the modified volume were determined. Many of these characteristics are predicted by theory and verified by field experiment. However, many experimental results are not fully understood.
- Develop and verify models of the modified volume. The characteristics of the modified volume were used to generate practical models. These models are intended to facilitate the usefulness of the IVORY CORAL concepts.

B. Program Organization

The IVORY CORAL program is a technically broad-based program. Several different government agencies and contractors have been involved during the course of the program. In order to meet the above objectives in an efficient manner, theoretical, laboratory, and field experimentation groups were organized. The functional relationships among these groups are shown in Figure 1. As shown, one of the primary outputs of the program was the model of the modified ionosphere. An efficient exchange of technical information was achieved through frequent workshops and technical review meetings. A task force was formed from the three groups to generate the model.

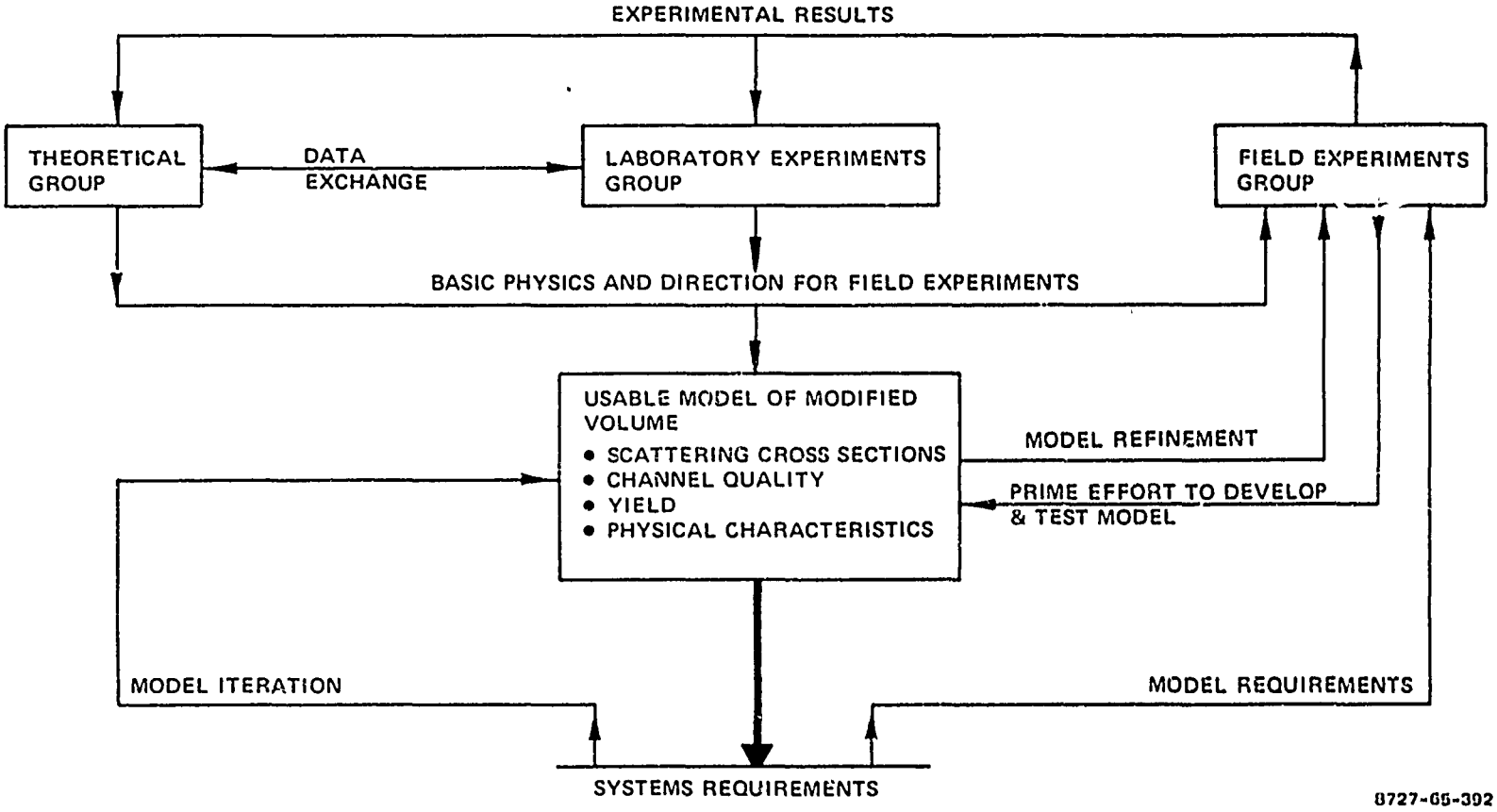

FIGURE 1 TECHNOLOGY EXCHANGE AMONG THE IVORY CORAL GROUPS

II SUMMARY

This report summarizes the technical results of the ARPA IVORY CORAL Program. The IVORY CORAL Program consists of the RF modification of the ionosphere and characterization of the modifications produced. The results of this program clearly demonstrate that the ionosphere can be modified when illuminated with reasonable RF power densities. Prior to the initiation of the IVORY CORAL Program, scientists and engineers primarily observed the ionosphere in its ambient condition. The perturbations that did occur were uncontrollable in time, magnitude, and resulting effect. The results of the IVORY CORAL Program clearly change that situation. The ionosphere can be modified with RF energy over a range of frequencies and power levels in a controllable manner. The implications of these positive results are that investigators can now treat the ionosphere as a "laboratory" in which reproducible scientific experiments can be conducted.

One of the desired outputs of any research program is the ability to predict experimental results from first principles and subsequently see this verified experimentally. In this regard, the IVORY CORAL Program was only partially successful. Many experimental results were predicted from theory; however, some were predicted and not observed. The reasons for these discrepancies are not known Several key experiments are recommended in Section VII of this report that may lead toward some resolution.

The richness of our scientific results will become evident as one reads this report. The results of major importance are very briefly summarized in the following:

- Field-normal scattering and refraction for wavenumbers (k) from 0.01 to 10 m^{-1} are well understood. Scattering during both day and night are observed, with strongest scattering occurring at night and weakest at 1400 ± 2 hours local time.
- In the E region, scattering drops off less rapidly for $k > 10\ m^{-1}$.
- Gross changes in electron density (N_e), electron temperature (T_e), and collision frequency (ν) have been produced and are understood in the F region. Generation and understanding of the corresponding quantities for D and E regions are beginning to emerge.
- Electron-density dependency on heater power has been determined to be

$$\overline{\left(\frac{\Delta N_e}{N_e}\right)^2} \propto P_H^n$$

  where $0.5 \leq n \leq 1.0$ for most cases.
- Characteristics of superthermal plasma waves (except parallel to the geomagnetic field) and electrons that are responsible for the generation of plasma lines, airglow, and parasitic plasma waves are understood. No inconsistencies exist between experimental observation of these quantities at Platteville and at Arecibo.
- The theory of plasma lines is partially understood; however, inconsistencies remain.
- Theory of low-wavenumber (0.01 to 1 m^{-1}) generation and characteristics is not understood. At present only suggested approaches exist.
- Theory of high-wavenumber ($> 1\ m^{-1}$) generation is only partially understood; the excitation is not clear.
- Radio-wave scattering and refraction aspects for center-line scattering are fully understood (limited only by our understanding of the scattering irregularities).
- Low wavenumbers (artificial spread F), which produce scintillation, appear through the topside of the F layer, and preliminary data suggest they may extend to the geomagnetic conjugate region.

- Finally, it has been concluded that most of the effects that are presently understood may be valid only at mid-geomagnetic latitudes under quiet and/or moderately disturbed ionospheric conditions. Extrapolations to other latitudes may be subject to question.

The IVORY CORAL concept--i.e., the RF modification and characterization of the ionosphere--has been clearly demonstrated in a technical sense. In terms of technical accomplishment, the IVORY CORAL Program stands as a milestone in ionospheric research, the full implications of which have not yet been realized.

III EXPERIMENTAL RESULTS

The field-experiment portion of the IVORY CORAL program has produced surprising results: the appearance of totally unanticipated effects, negative results in experiments that "should have seen something," and initial explanations that subsequently required complete revision. The basis for these surprises lies primarily in the richness and complexity of the processes of interaction between intense radio waves and the ionospheric plasma, and not in naiveté on the part of the experimenters involved.

The idea that provided the impetus for the construction of the Platteville, Colorado heating facility [and later for the heating capability at the Arecibo Observatory (AO)] was that deviative absorption of HF energy in the F-region could substantially alter the local electron temperature and density. It was anticipated that the electron-density changes might produce significant effects on radio waves propagating through the region. Systems that it was thought might be affected by ionospheric heating include: HF communication and radar systems that depend on the unique propagation properties of the ionosphere, satellite-ground radio links that must pass through the ionosphere, and infrared sensing systems that could be disturbed by substantial changes in the intensity of ionospheric infrared emissions.

The Platteville facility[1]* was constructed and operated by the Department of Commerce, Institute for Telecommunication Sciences (ITS). It makes use of a circular array of ten crossed dipoles approximately 600 m in diameter for operation in the frequency range of 5 to 10 MHz.

---

*References are listed at the end of the report.

At a lower frequency range, 2.7 to 3.3 MHz, five crossed dipoles are used, placed at the corners of a square with one located in the center. The nominal RF power output is 1.5 MW. Both O- and X-mode polarization are available. The antennas are steerable from 0° to 30° from zenith. The heating capability at AO^2 is provided by a single 150-kW transmitter driving a log-period feed that illuminates the 1000-ft reflector. The maximum effective radiated power (ERP) at AO is 4 to 6 dB less than the Platteville ERP. The size of the illuminated region is considerably smaller.

The Platteville facility was originally instrumented with several radio and optical diagnostics intended to detect the expected electron temperature and density changes. The incoherent-scatter radar at AO was capable of "mapping" the electron-temperature changes and of giving additional information on electron-density and neutral-temperature changes. As the heating experiments continued, additional diagnostics were frequently employed to clarify earlier results, and to investigate new effects observed or hinted at by existing diagnostics. Also, additional experiments were performed to explore newly conceived ideas about the processes involved in ionospheric heating that arose from the concurrent theoretical and laboratory components of the IVORY CORAL program.

Two examples of important and unexpected experimental observations are worth mentioning here. The first occurred during the initial operations of the Platteville facility (April 1970). A sensitive vertical-incidence ionospheric sounder was being operated near Platteville for the purposes of determining the parameters of the ambient ionosphere and of observing distortions in the F-region electron-density contours produced by heating. This diagnostic was plagued by "bad luck" in the form of spread-F echoes which made accurate measurements of the ionosonde data quite difficult. Fortunately, naturally occurring spread-F was relatively uncommon for the Platteville situation and it soon became

apparent that the heater was producing artificial spread-F (ASF). The appearance of this ASF led to the suggestion that field-aligned scattering (FAS), which is frequently observed in connection with natural spread-F, might also be produced by heating. In fact, FAS was observed and has proven to be one of the most interesting phenomena produced by ionospheric heating.

The second example occurred during the first heating tests at AO (October 1970). The incoherent-scatter radar, which was being used primarily to measure changes in the ionospheric electron temperature, can also detect the plasma line* when the line intensity is enhanced by solar photoelectrons. Typically, solar photoelectrons enhance the plasma line by about a factor of 10. During heating, the plasma line was observed to be enhanced by 4 or 5 orders of magnitude. This observation has markedly influenced our understanding of the role of plasma instabilities in ionospheric heating.

In the remainder of this section we will present:

- A classification of the types of effects that have been examined experimentally (including those with negative results).
- A brief listing of the objectives and methods of the major experimental efforts.
- The significant experimental results produced by the program.
- The current empirical explanations of the results.
- References to sources of more detailed information.

---

*The plasma line is a spectrally narrow return, shifted in frequency above and below the radar frequency by an amount equal to the local ionospheric plasma frequency.

A. Classification of Effects

The observable characteristics of the modified ionosphere may be described in terms of changes in the energy (temperature) and spatial distribution of ionospheric constituents. A major distinction applicable to the observable effects is whether the spatial characteristics of the effect are "global" or highly structured--i.e., whether spatial variations occur on a scale comparable to the size of the heated region or on a scale much smaller than the size of the region. For highly structured effects, further distinctions are made based on the predominant sizes and orientation of the structures. In Table 1, the major observable effects of ionospheric heating are summarized along with the main diagnostics used in studying each effect.

The classifications used in Table 1 will be used in describing the experimental results in the following sections, although in some cases a single experiment yields information relevant to more than one effect. An artificial distinction between D-region effects and E- and F-region effects has been made due to the dissimilarity of the applicable diagnostics.

B. Large-Scale Electron-Density Changes

Early theoretical work on heating indicated that substantial changes in the ambient F-region electron density would be produced near the height of reflection of the incident heating waves--i.e., where the refractive index for the heater-wave polarization equals zero. While such changes were of great interest early in the program, studies of this phenomenon are of limited scope due to changing emphasis of program objectives. Enough results are available, however, to conclude that the observed changes are in reasonable agreement with currently accepted theoretical explanations.

Table 1

SUMMARY OF POTENTIALLY OBSERVABLE PHENOMENA PRODUCED BY IONOSPHERIC HEATING

Phenomenon	Main Diagnostics and Characteristics
Global Effects	
Electron-density changes	Radio-wave refraction--focusing, defocusing, and angular deviation on HF paths propagating through the region Vertical-incidence reflection--changes in ionosonde records Incoherent-scatter radar--fine-scale mapping of electron-density changes Whistler receivers--modification of whistler ducts Magnetometers--changes in the geomagnetic field measured on the ground
Electron-energy changes	Incoherent-scatter radar-fin -scale mapping of electron-temperature changes (400 MHz) Optical emissions--measurements of temperature and/or energy distribution from observations of excited transitions
Neutral temperature and density changes	Radio-wave refraction--oblique HF paths not passing through the heated region affected by neutral disturbances traveling out of the region Infrasonic detection--acoustic detectors on the ground
D-region changes	Vertical-incidence-radar absorption--changes in strength of signals reflected above the D-region Partial-reflection radar--changes in turbulence structure in lower D region Riometer--D-region attenuation changes measured at 30 MHz Intermodulation--attenuation and phase changes of low-frequency signals propagating in the D region
Highly Structured Effects	
Field-aligned electron-density fluctuations--small scale sizes	Radio scattering--backscatter and oblique side-scatter at frequencies from ~10 to 2000 MHz
Field algined electron-density fluctuations--large scale sizes	Radio scattering--vertical-incidence backscatter at frequencies from ~5 to 10 MHz Radio-wave refraction--scintillations of satellite transmissions observed on the ground at frequencies of 100 to 400 MHz and scintillations of radar echoes of satellites viewed through the heated region at ~1000 MHz
Field-parallel electron-density fluctuations	Radio scattering--backscatter at ~400 MHz and sidescatter at ~60 MHz
Horizontal electron-density fluctuations	Radio scattering--backscatter at 350 MHz

1. Vertical-Incidence Ionosondes

Vertical-incidence (VI) ionosondes are located near both the Platteville and the AO heaters. These provide data on changes in the overhead electron-density profile, and, under conditions when multiple traces appear, can give some information on the horizontal spatial properties (tilts) of the heated region.

Estimates of the electron-density changes produced by O-mode heating[3,4] indicate that the electron-density is decreased on the order of 10% at the center of the affected region. The region extends horizontally over an area comparable to the beamwidth of the heating transmitter antenna, and vertically over a range of tens of kilometers, centered near the height where the local plasma frequency is equal to the heating frequency.

2. Sporadic-E Layers

In 1972 Utlaut and Violette[3] reported short-lived E-region echoes on ionograms from frequencies above $f_o F2$ in connection with RF ionosphere modification experiments at Boulder. The returns appeared to be from sporadic-E layers that blanket (obscure) the F region only below the E-region critical frequency (2 to 4 MHz). It was stated that due to the normal variability of the E region, and particularly of sporadic-E occurrence, the high-frequency returns could not definitely be associated with the ionosphere modification experiment.

Similar sporadic-E echoes have been observed at Arecibo[4] in association with the ionosphere modification program there, but the effects, as at Boulder, are not reproducible to the extent that they can definitely be related to the heating experiment. On two occasions during ionosphere modification experiments an intense, blanketing, natural sporadic-E layer developed. On one of these occasions, HF-enchanced

plasma-line echoes at 5 MHz were observed in one patch (but not in other patches) of a sporadic-E layer, requiring the plasma to have an electron density corresponding to 5 MHz. The blanketing frequency at the time was nearly 10 MHz. Failure to observe the plasma line continuously suggests that the blanketing may be associated with causes other than reflection of the HF waves.

A brief survey of all data within the time period covered by four series of heating experiments suggests that at Arecibo natural range-type spread frequency in a sporadic-E layer is fairly common (for this sample) and is generally observed when the blanketing frequency is less than about eight-tenths of the maximum frequency in the sporadic-E layers.

3. HF Oblique Soundings

The electron-density gradients produced by (F-region) heating can cause deviations in the normal raypaths for HF waves propagating through the heated region. These raypath deviations are observed as changes in received signal intensity (due to focusing or defocusing) and as changes in the observed angle of arrival. Several experiments have been performed with the Platteville heated region using this technique.

Oblique HF ionograms, transmitted over a 2600-km east-west path centered over Platteville, were examined for evidence of focusing and defocusing effects that were produced by heating.[5] A limited amount of data was available that suggested that this effect was observed. It was not possible to rule out the possibility that the effects were due to natural causes. Also, no quantitative analysis was performed to determine the magnitude of the electron-density change. It appears that this technique can relatively easily provide considerable information on electron-density changes.

4. Incoherent-Scatter Radar

The 430-MHz incoherent-scatter[4] radar at AO has also been used to observe the electron-density changes within the heated region above Arecibo. Density decreases of up to 14% were measured. More detail on the AO measurements, which are primarily directed toward electron-temperature measurements will be found in Section III-B-8.

5. Whistler Receivers

A direction-finding whistler receiver was operated near Platteville in a joint experiment of Stanford University and NOAA. The motivation was to detect new whistler ducts that might be created by the localized electron-density changes produced by the heater. Data were collected during two periods, but as yet no results are available from this experiment.

6. Magnetometers

During early IVORY CORAL experiments, heater-induced perturbations of the geomagnetic field were looked for, using a wide-baseline gradiometer and 3-axis magnetometers,[6] with negative results. During these experiments, the low-frequency limit of the Platteville facility was 5 MHz, and all heating was done at F-region altitudes.

For the October 1973 tests the low-frequency limit of the Platteville facility had been lowered to 2.7 MHz. This permitted heating the E-region during the day, and would be expected to produce greater geomagnetic-field effects.

7. Electron-Energy Changes

The changes in ionospheric electron density described in the preceding section are thought to be a secondary effect, produced by a

localized change in the ionospheric electron-energy balance. Changes in the electron thermal energy of the heated region can be measured in a very satisfying manner with the AO incoherent-scatter radar. The results of these measurements are generally in good agreement with theory.

In addition to measuring the electron thermal energy, optical measurements, both at Platteville and AO, have produced some information on the excitation of superthermal electrons.

8. Arecibo Incoherent-Scatter Radar

The heating experiments at Arecibo have yielded a number of interesting results derived from the normal absorption of radio waves in the ionosphere[2,7,8] and from the anomalous absorption of the high-frequency (5- to 10-MHz) waves and the excitation of plasma instabilities.

O-mode heating of the ambient electrons has been detected. Deviative absorption, raytracing, and heat-balance calculations are consistent with the magnitude of the increase, typically peaking at 150° to 400°K, with the higher values at night; the location, typically 4° to 9° north of the Observatory; the volume, matched to the beam when mapped in two or three dimensions; and thermal relaxation times of a few tens of seconds. The ion temperature is unchanged within error bars of tens of degrees kelvin.

The effects of the deposition of radio-wave energy on electron temperature, ion temperature, and electron number density, are discussed here. Parameters important in determining heating effects are the transmitted power, polarization, HF frequency, ionospheric critical frequency, temperature, altitude, and time of day (HF absorption in D and E region). The multiparameter dependencies are illustrated in the form of "T_e cubes" (Figure 2). The cubes show several items simultaneously. The front face graphs heater power for each time block, as well as the

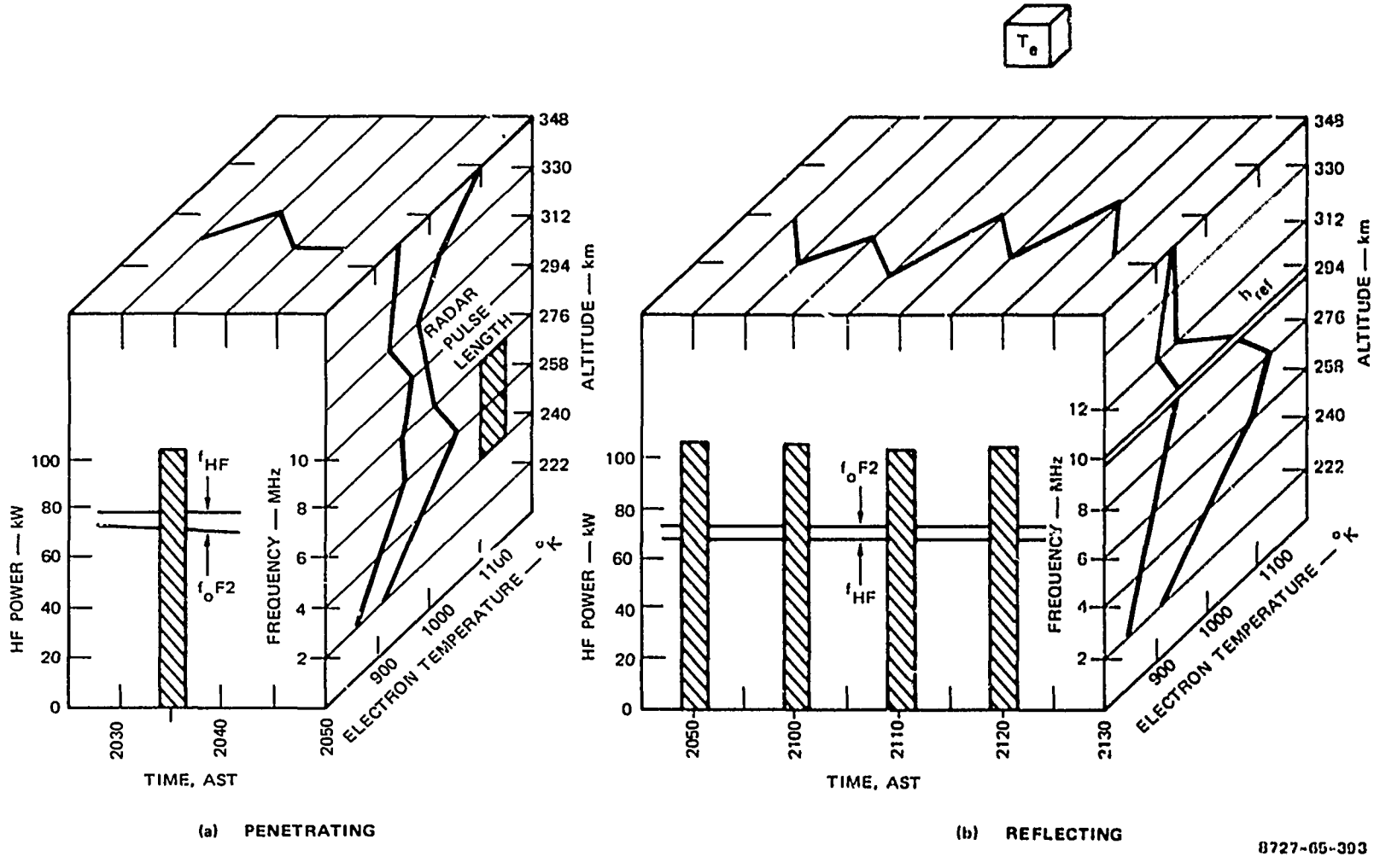

FIGURE 2 CHANGES IN ELECTRON TEMPERATURE FOR PENETRATING AND REFLECTION O-MODE PROPAGATION

heater frequency and f_oF2 versus time. The top face gives the electron temperature for each time block integrated in altitude over the entire F layer. The right face of each cube shows two plots: the lowest-temperature plot is the time average of all the unheated data blocks, and the other plot is the average of the heated blocks.

An example of the difference in heating effect between penetrating and reflecting cases is given in Figure 2. For the penetrating case [Figure 2(a)], the F layer is heated near the peak, while in the reflecting case [Figure 2(b)], only electrons at and below the reflection altitude of 294 km are significantly heated. The most striking result here is the abrupt cutoff of the heating above the reflection altitude, and also the fact that the heating is greater for the reflecting case.

An experiment was made with the heater power changed from zero to half to full power. The results are given in Figure 3, which shows electron temperature versus altitude for the three power levels. The effect of 100 kW on the electrons is not quite double the effect of 50 kW. The ions do appear to be heated, but no firm conclusions can be

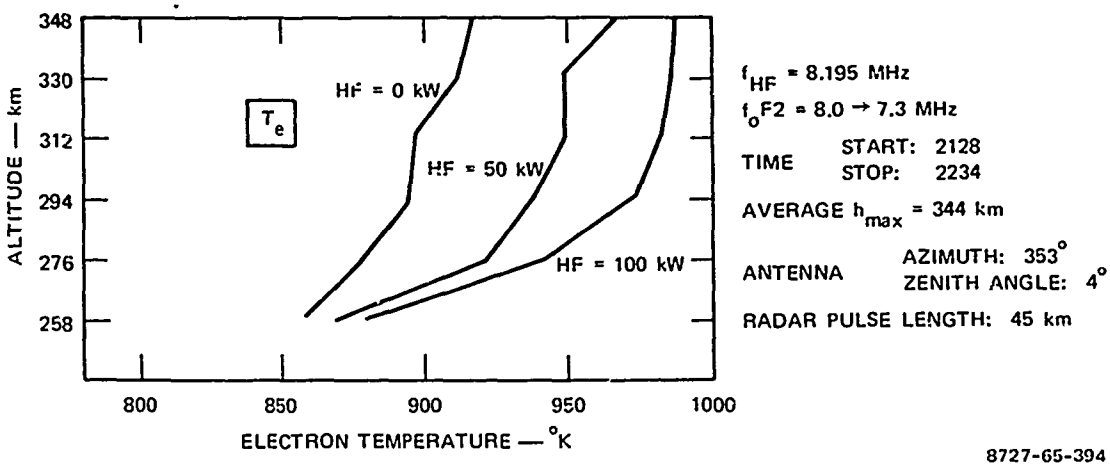

FIGURE 3 ELECTRON TEMPERATURE vs ALTITUDE FOR ZERO-, HALF-, AND FULL-POWER HEATER OPERATION

drawn since the apparent magnitude of heating is less than the expected measurement errors.

The extent of the O-mode heating has been determined by making maps in the magnetic meridian where the O-mode radio wave deviates toward the north. The ambient temperature is first measured, and then the heater is turned on while the interrogating beam is swung from about 4° north to 10° north (angles directly overhead are blocked out by the heater antenna). Figure 4 shows such a map, with a heated region centered 35 km to the north of the observatory at an altitude of 320 km. To determine possible heating out of the meridian plane, a measurement to the west was made, and little heating is indicated there. The run illustrated

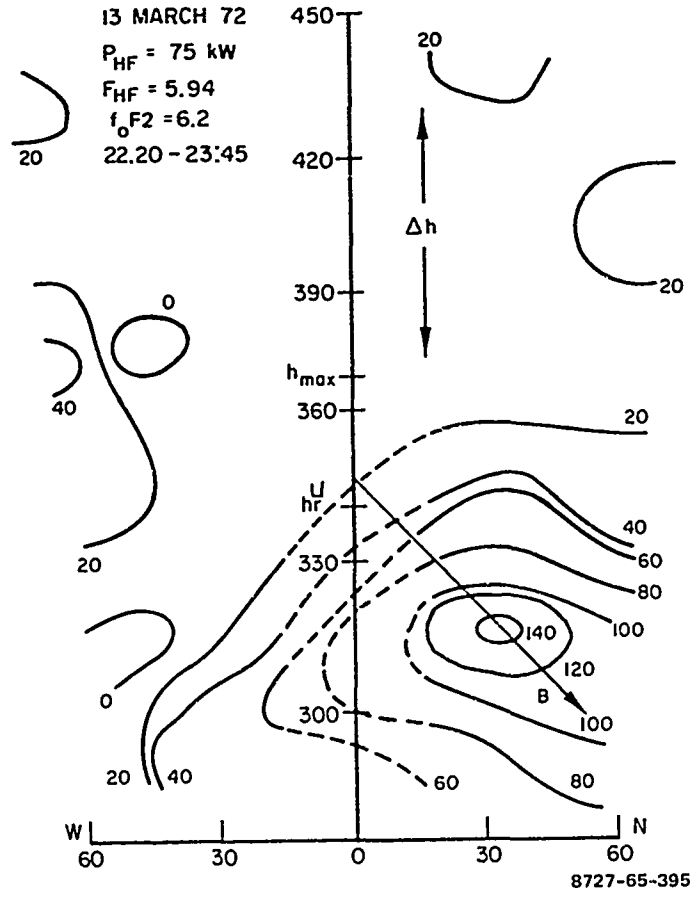

FIGURE 4 CONTOUR MAP OF CHANGE IN ELECTRON TEMPERATURE

here is for the reflected case, but penetrating cases show similar results if the heater frequency is well matched to f_oF2. The line labeled "B" is the magnetic field line that passes through the center of the heated volume.

The inherent variability of the ionosphere has precluded measuring induced changes in electron number density during most of the experiments. During one run the heater was cycled on and off at 10-minute intervals: the electron temperature increased by 23%, and at the same time, the electron density decreased by 14%.

During the day the HF heating observations to date have not exceeded a 50°K change.

9. Airglow Observations

The measurements presented here were based primarily on the early observations of 6300-Å enhancement.[4] These enchancements were presumed to be caused by collisions between oxygen atoms and energetic electrons generated when the heater was operated in the O-mode of polarization. The general techniques used were photometric, with several types being employed.

a. Location, Structure, and Dynamics of the Airglow Region

This portion of the airglow observations was very successful. Two supplementary photometric techniques were used. In one case triangulation measurements were made using NOAA photometers quite some distance apart. This technique was quite useful in determining the altitudes of the enhanced region and in following movement of the region on the order of some tens of kilometers. The photometers of the University of Pittsburgh were rapid-scanning and were used to measure changes in the structure occurring on the order of 10 to 15 s. Figure 5 shows the

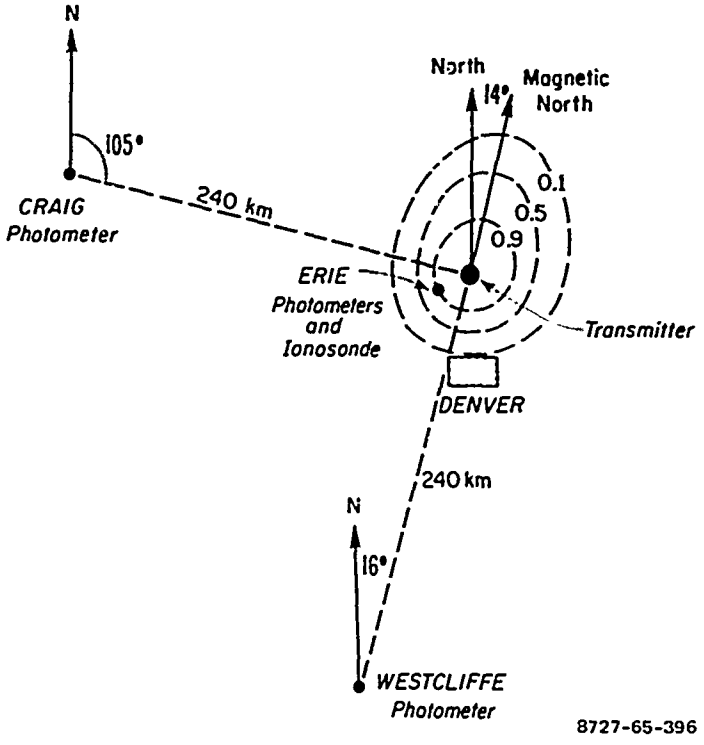

FIGURE 5 LOCATION OF PHOTOMETERS TO MEASURE 6300-Å ENHANCEMENT

location of several of the sites used for observations together with an idealized representation of the airglow region.

b. Electron Energy Distribution

Since the electron energy distribution was non-maxwellian and calculations showed that only electrons in the tail were probably affected, attempts were made to determine the distribution. This was carried out by identifying spectral lines excited in auroras possibly by relatively low-energy electrons.

Attempts were made tc observe lines requiring the following approximate energies for excitation: 1, 2, 4, 9, 12, 18, and 22 eV. Only two of these were observed: the first was the O('D) state of atomic oxygen at 1.96 eV, which emits the red 6300 Å-line; the second was the

O('S) state, which requires 4.17 eV to excite. The emission from that state is the oxygen green line (5577-Å). This emission was observed to be affected by the transmitter only infrequently, with the reason not understood. It should also be mentioned that on occasion when conditions seemed favorable, not even the red line was excited. This objective can therefore be partially successful although the observation did give sufficient data to place restrictions on assumed distribution.

c. Electron Energy Mechanism

Calculations at Utah University indicate that considerable energy is going into other species besides atomic oxygen, probably molecular nitrogen. These calculations are still being carried out with the view of estimating how efficiently the RF power can be coupled into the F-region. These calculations are being continued on the basis of observations made in October 1973, in which an extremely large red-line enhancement was observed at Platteville. Crude estimates based on those observations suggest that possibly as much as 30% of the transmitter power can be coupled into the ionosphere. This should be considered an upper limit at present.

The observational portion of this objective was carried out by the Air Force using a radiometer-equipped U-2. The goal was to detect changes in the infrared emission in the 10- to 12-micron region. No success was achieved with these attempts.

d. Power Dependence

Only limited data were obtained concerning the dependence of the airglow enhancement on the transmitter power. The best results were obtained on October 25, 1970, by the University of Pittsburgh and suggest the red line intensity varies on the third or fourth power of the

transmitter power. Most attempts since then have been hampered by experimental priorities or a rapidly changing background. This portion of the program still remains to be carried out.

e. Dependence on Ionospheric Conditions

Sufficient data have been acquired, both airglow and ionospheric, that now a statistical study of the effect of the ionosphere on the enhancement is being carried out. Such items as magnetic disturbances, the gradient of the electron density profiles, the electron content, base electron temperatures T_e etc., are being considered. This is an analysis program and is not complete. The data obtained in the fall, 1973, are proving to be especially useful since they were obtained under relatively stable nighttime conditions.

f. Seasonal Dependence

No seasonal dependence of the enhancement has been identified.

g. Experimental Results

While the data for the figures presented here were obtained with NOAA photometers, they are considered representative and are used for convenience. In the interest of brevity only those results are given that presumably bear most directly on the modification process.

Initially consider Figure 5. The contours shown were obtained with the high-frequency antenna. Later data obtained with the lower-frequency antenna indicate that the contours in general have not changed. However, the size of the region is often twice as large. Observations also show that the intensity contours are generally not smooth and can change fairly rapidly.

Both triangulation data and time-constant measurements from the decay of the red-line enhancement can be used to infer that the airglow region is relatively thin, probably less than 1/3 of the N_2 scale height, or about 10 km.

In Figures 6, 7, and 8 the motion and behavior of the airglow region are shown. It should be mentioned that this behavior is

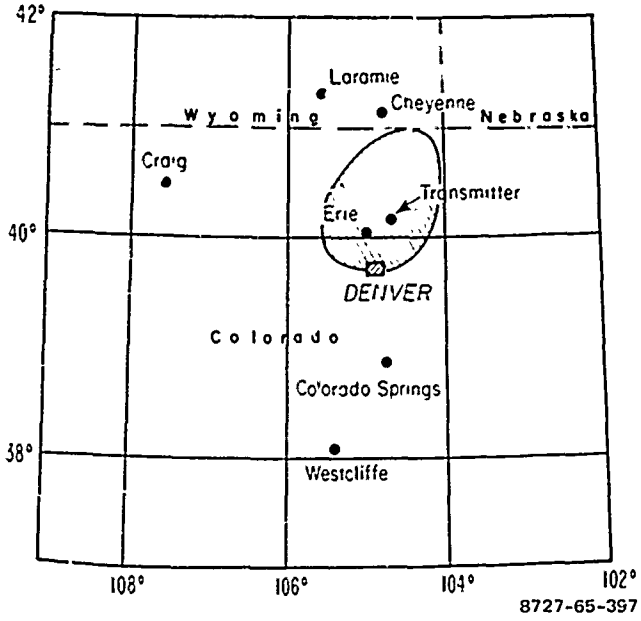

FIGURE 6 TYPICAL AIRGLOW REGION AT ABOUT 2115 MST ON 18 SEPTEMBER 1972

usually seen only when $f_oF2 \sim f_t$ (transmitter frequency). It is also important to note that this behavior presently is unpredictable. Many various forms of decay and motion have been observed.

Both red-line enhancements and red-line suppressions have been observed. X-mode suppressions of roughly 1% (out of 120 rayleighs) have been obtained, consistent with the temperature dependence of the recombination rate. O-mode enhancements have been observed of about 1 to 10 rayleighs offering both HF-power and enhancement-altitude-dependence information.

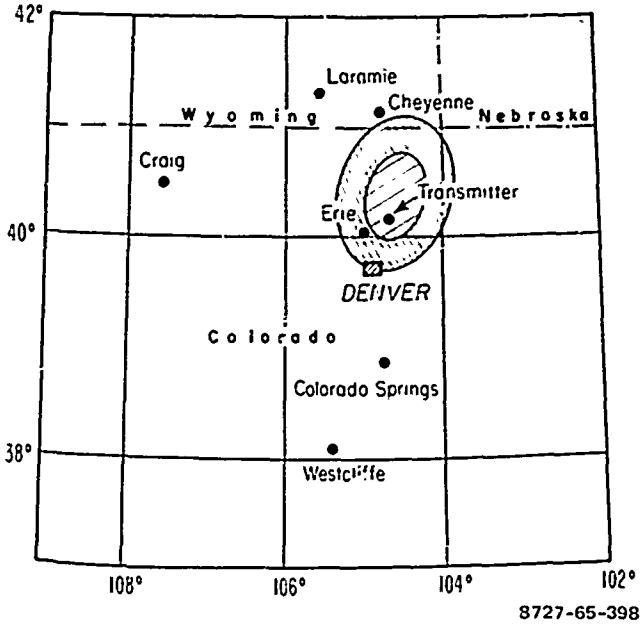

FIGURE 7 AIRGLOW OF 18 SEPTEMBER 1972 AT 2130 MST

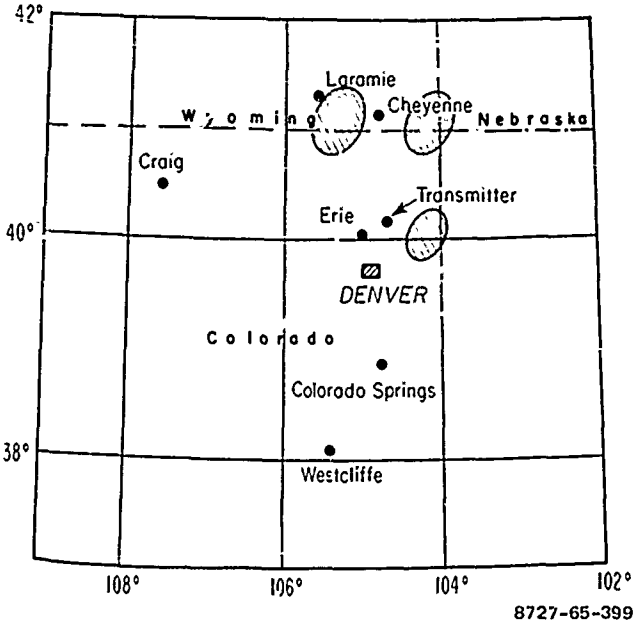

FIGURE 8 AIRGLOW OF 18 SEPTEMBER 1972 AT 2145 MST

6300-Å airglow enhancements were observed at Arecibo in October, coincident with the HF excitation of the ionospheric plasma waves. These manifestations of the plasma waves produced by the anomalous HF heating help to better confirm and define the damping mechanisms, particularly with coincident plasma-line-decay-rate data. The airglow enhancement is also another indication that the Arecibo facility can deliver above-threshold power densities (airglow enhancements were seen at a factor of 4 below available Arecibo transmitted power levels), given that the stronger airglow enhancements were comparable with those seen at Platteville.

C. Neutral-Density Changes

No direct measurements of changes in the neutral density of the heated region have been made. Attempts have been made to detect the effects of neutral changes by observing heater-generated acoustic waves propagating out of the heated region.[9] An array of infrasonic detectors located around Boulder, Colorado was used in an attempt to detect an infrasonic wave, generated in the upper E region, which would propagate to the ground. Approximately 10 one-hour tests were performed during October 1973. No infrasonic waves correlated with the heater operation were observed, although additional data analysis is planned.

Additionally, HF oblique soundings have been made over a 2600-km path centered about 200 km south of Platteville.[9] The objective was to examine the sweep-frequency ionograms for evidence of traveling ionospheric disturbances (TIDs) that could be related to heater operations. Natural TIDs produce a characteristic moving "kink" on such ionograms, even when the TIDs are relatively weak. Data from early tests indicated that TIDs may have been produced by heater operation. The quantity of data available from the early experiments was insufficient to eliminate the possibility that the observed TIDs were natural. A more systematic

experiment was carried out during October 1973. The results of this experiment are not yet available.

D. Field-Aligned Small Electron-Density Fluctuations

The distinction between small and large field-aligned electron-density fluctuations is made primarily on the basis of the types of diagnostics applied in their observation. "Small" implies that the fluctuations have scale sizes, at least in one dimension, of about 30 m or less, and that they are primarily observed using Bragg scattering of radio waves.

Since natural spread-F is known to exhibit geomagnetic-field-aligned structure, the discovery of heater-produced spread-F led experimenters to search for field-aligned structure within the heated F region. Radar diagnostics oriented with geometries suitable for scattering from field-aligned structure in the F region over Platteville revealed very strong heater-related scattering effects. It has subsequently been demonstrated that when the F-region reflection height of the heating signal is matched to the radar's field-aligned specular height (height for which the angles of incident and reflected radar energy are equal with respect to the geomagnetic field line over Platteville), then the heated region's scattering cross section is nominally 75 dBsm below 80 MHz, falling to 45 dBsm at 157 MHz and to 35 dBsm at 435 MHz. The magnitude of scattering decreases as a consequence of mismatch between the heater height and specular height at a rate of about 0.5 dB per km of mismatch.

Because of its high scattering cross sections and consequent potential utility, field-aligned scattering has received the most experimental attention and is empirically the best understood of all the heater-induced effects. A morphological model of the disturbed region has been developed that satisfactorily accounts for the observed scattering characteristics. This scattering model is described in Section IV of this report.

Other bistatic experiments have demonstrated the utility of heater-induced field-aligned scatter for communicating over long transmission paths at frequencies not normally usable.

In addition to scattering by zero-frequency fluctuations, which produces scattered signals of approximately the same frequency as the incident signals, fluctuations are observed whose frequency is equal to the heater frequency and whose scatter signals are offset in frequency above and below the incident frequency by exactly the heater frequency.

For center-line observations the presence of field-aligned structures within the heated volume was first established in a bistatic experiment that employed a mobile aircraft-based receiver to trace out the scattering zones over the ground. For radar illumination from White Sands Missile Range scattered from the heated volume over Platteville, it was found that these zones consisted of wide east-west bands narrowly confined in the north-south direction, indicative of scatterers aligned with the geomagnetic field.

Principal experiments and experimenters involved in measuring the parameters of field-aligned scatter are:

- HF backscatter from WSMR (Raytheon).
- HF backscatter and sidescatter, Stanford Research Institute (SRI).
- VHF TV intercept (SRI).
- VHF, UHF backscatter from WSMR with RAM, Riverside Research Institute (RRI).
- Airborne HF and VHF receivers (RRI, Raytheon).
- HF-VHF sweep-frequency sounding, numerous paths, multiple receivers (SRI).
- VHF and UHF bistatic, WSMR to Palo Alto and El Centro, California (RRI, SRI).

- VHF-model-verification experiment (SRI).
- VHF bistatic-communications demonstration (Barry Research Corporation).

HF heating of the E and F region of the ionosphere produces electron-density irregularities elongated along the geomagnetic field both above and below the heater reflection height (the altitude at which the vertically incident HF heater signal is reflected by the ionosphere). This height can be adjusted by varying the frequency of the heater transmissions. The individual irregularities within this region can be thought of (for the purpose of explanation) as long, thin cylinders aligned with the geomagnetic field. If RF energy illuminates such a cylinder it will be scattered much as a beam of light would be scattered by a long, thin shiny metal rod. When the illumination is perpendicular to the axis of the cylinder, the cylinder will scatter energy throughout the plane normal to the cylinder and containing the illuminating ray. For this case, some energy will be scattered back in the direction of the illuminator and can be received at the same location from which it was transmitted, as in the case of monostatic radar. Obviously the cylinder must be perpendicular to the radar look direction in order to be visible to the radar, and the locus of points providing field-normal geometry for a given radar location is called the monostatic reflection surface. There is a different such surface (which can be determined by geometry) for each different radar location. One possible example is shown in Figure 9. Notice that in this case the monostatic specular surface is substantially above the heater reflection height for the radar location shown.

For the case of illumination that is not normal to the cylinder axis the energy will be scattered throughout a cone of angles where the angle of the scattered energy equals the angle of illumination with respect to the cylinder axis. In that case, the scattered energy can intersect the earth at a location different than that of the transmitter, as is shown

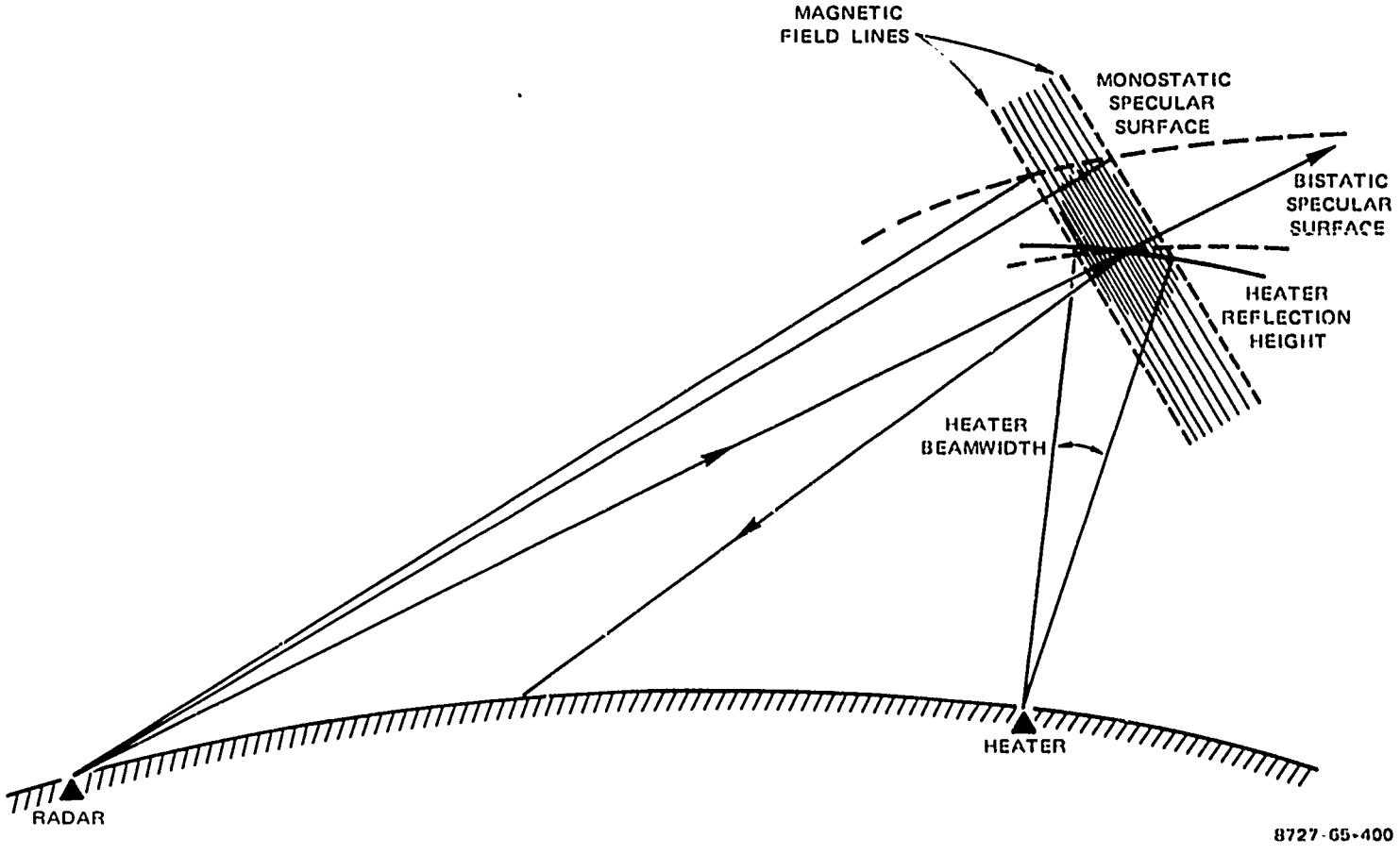

FIGURE 9 ELEVATION VIEW OF FIELD-ALIGNED SCATTERING

in the figure for energy scattering from a field-aligned irregularity centered in the heater beam at the heater reflection height. The scattering cone always contains the extension past the scatterer of the illuminating ray, and the cone and cylinder have a common axis of symmetry. When the locations of the separate transmitting and receiving sites are held fixed, there is again a locus of points where the angle of incidence from the transmitter and angle of scattering to the receiver are equal with respect to the geomagnetic field. In that case, the locus of points is called the bistatic specular surface; in general there is a different such surface for each possible pair of transmitter and receiver locations. The bistatic example shown in the figure has the heater reflection height well matched to the bistatic specular surface. Such matching has been empirically shown to produce the maximum magnitude of RF scattering and for this reason the heater operating frequency is generally adjusted to provide the best possible match between the heater height and the specular surface for the transmitter and receiver locations of interest. The intersection of cones of scattered energy can be plotted on a map for a fixed irregularity location and altitude but with a variety of scattering angles, as illustrated by Figure 10.

The contours of Figure 10 would be different for different heater reflection heights and for different heater locations. However, they may be calculated in a straightforward manner for any location from geometry and a knowledge of the geomagnetic field. Such maps indicate that optimum heater-supported communications would be possible for the conditions shown from any place on the 90° contour to any place else on the 90° contour, or from any place on the 88° contour to any place on the 92° contour, or (in general) from any place on one contour to any place on its supplementary contour.

If a fixed transmitter location is assumed, a different set of intersection contours can be constructed with heater reflection height

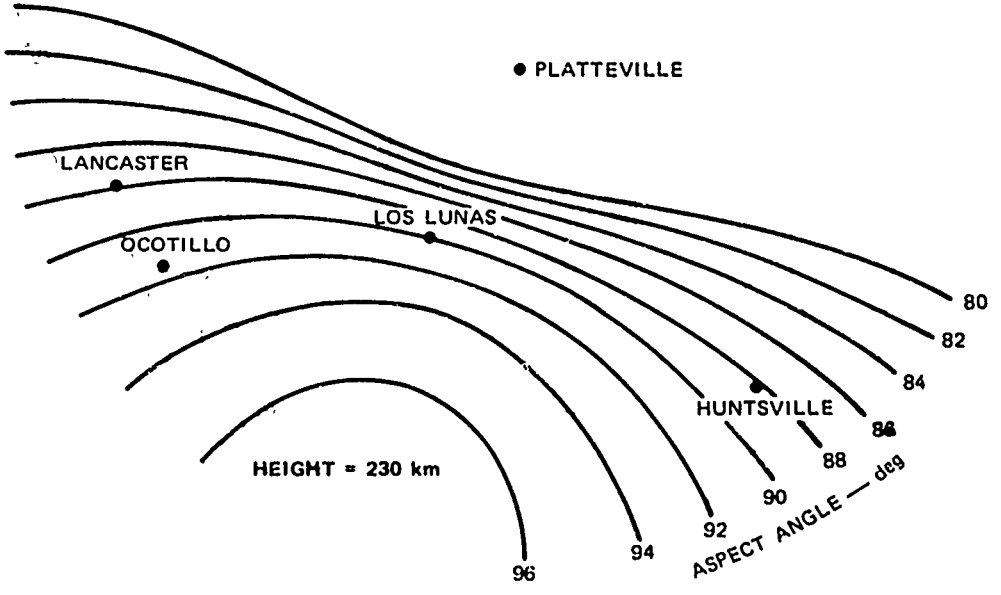

8727-65-401

FIGURE 10 GROUND INTERSECTIONS OF SCATTERING CONE WITH VARIOUS ASPECT (scattering) ANGLES FOR A SINGLE IRREGULARITY CENTERED OVER PLATEVILLE, COLORADO, AT AN ALTITUDE OF 230 km

as a parameter, as shown in Figure 11. For the transmitter location shown and a given reflection height, the scattered energy will be received

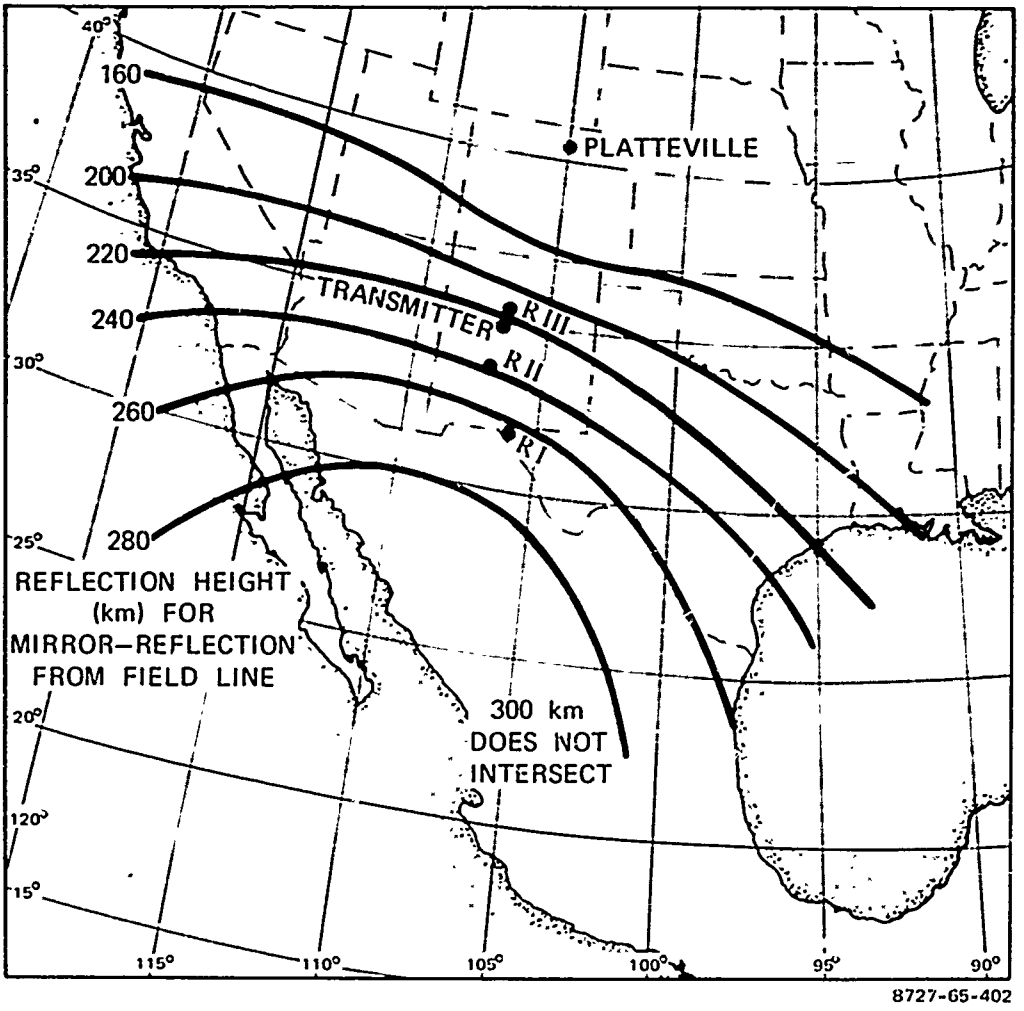

FIGURE 11 GROUND INTERSECTION CONTOURS FOR A FIXED TRANSMITTER LOCATION AND VARIOUS SCATTERING ALTITUDES FOR A GEOMAGNETIC-FIELD-ALIGNED IRREGULARITY CENTERED OVER PLATTEVILLE

most strongly along the contour for that heater height. Notice that for the receiving sites indicated in the figure the optimum heating height for RI is a little above 260 km, for RII it is slightly below 240 km, and for RIII, it is slightly below 220 km. As a consequence of the fact that there are many scattering irregularities distributed throughout the heater

beam (which is nominally 100 km in diameter at 250 km altitude) the regions where scattered energy intersects the ground are actually bands 100 km to 300 km wide (at their half-power points) instead of lines as shown in the figure. The contours shown represent the locations of maximum scattering, although energy can still be received some distance from these lines. A typical example of the dependence of on-frequency scattering cross section on heater reflection height for a given observation geometry is shown in Figure 12, where a smooth curve is drawn through the data points to represent the nominal height dependence. This dependence seems to be roughly independent of the observation frequency. Notice that matching the heater reflection height to the optimum specular reflection height for the path of interest is not terribly critical--matching to within ±10 km is sufficient to achieve scattering magnitudes

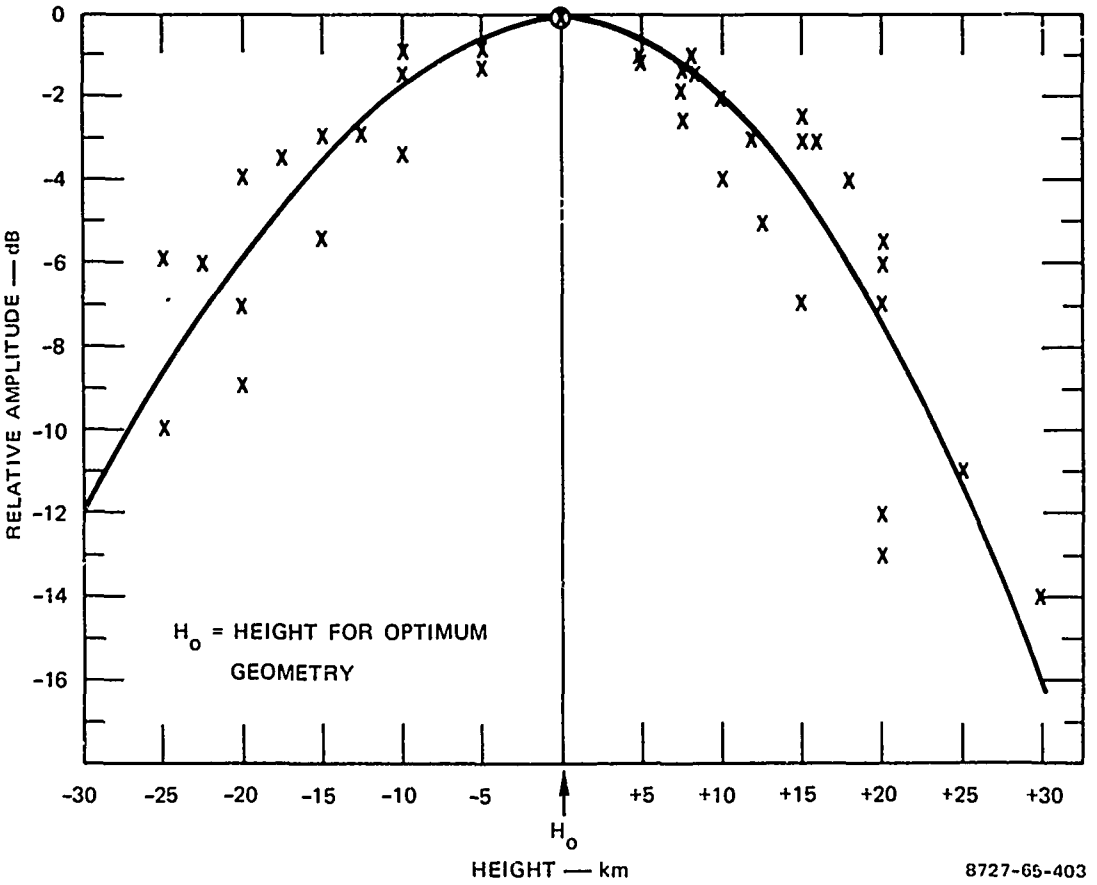

FIGURE 12 CROSS-SECTION VARIATION WITH HEATING HEIGHT

within 3 dB of maximum. However, mismatching by 30 km can reduce the received signal strength by as much as 15 dB, so some care in selecting the heater operating frequency is clearly necessary.

For plasma-line scattering at both VHF and UHF the aspect sensitivity, if it exists, is much weaker. Contrary to center-line scattering, the plasma-line scattering regions are, in fact, found to coincide quite closely with the heater reflection heights. Plasma-line backscatter has been observed for mismatched heights as great as 90 km--a condition where center-line scattering has never been observed. However, since maximum plasma-line returns are observed with nearly matched heights, it seems that the plasma-line scattering may be aspect-sensitive, at least to some extent.

Many observations of the F region have been made at frequencies between 10 and 435 MHz. The nominal cross-sectional frequency dependence derived from many observations is shown in Figure 13. The band thickness of this curve is intended to represent the range of observed maximum cross sections for evening hours where the heater height was optimum for the observation geometry. Obviously, mismatching the heater height could cause the observed cross section to fall substantially below this curve. The variation in observed cross sections under matched conditions due to diurnal variability can reduce these values by about 10 dB. Observations have also been made at L and S band but no scattering was observed.

Recent measurements of FAS from irregularities generated in the E region during the day indicate that for frequencies below 80 MHz, observed cross sections are comparable to daytime F-region values (~60 to 65 dBsm). For E-region FAS however, the cross section does not begin the rapid decrease with increasing frequency until at least 150 MHz.

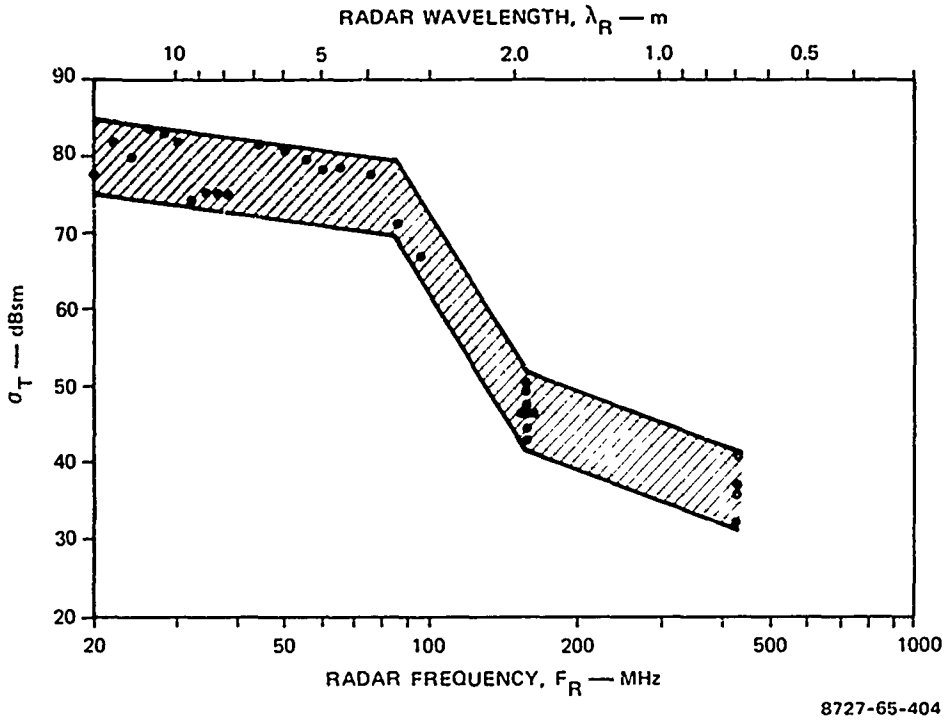

FIGURE 13 MEASURED TOTAL RADAR CROSS SECTION

It is seen that, for center-line scattering, the VHF cross sections exceed the UHF cross sections. For plasma-line scattering, however, this is not the case. For the plasma line, peak UHF cross sections of ~ 7 dBsm, equal to the center-line cross sections, were observed, whereas at VHF, peak plasma-line returns of ~ 1 dBsm were observed. This difference in cross section between the VHF and UHF plasma-line echoes is further accentuated by the fact that the VHF per-pulse scattering column is of the order of ten times larger than the per-pulse UHF volume. Hence, as discussed in somewhat more detail in Ref. 6, these results indicate a significant reversal in frequency dependence between the center-line and plasma-line scattering properties of the heated volume.

As discussed later the observed characteristics of heater-produced field-aligned scattering can be satisfactorily accounted for by a Booker scattering model where the morphology of the heater-disturbed F region

can be represented as shown in Figure 14. The heater-produced disturbance in the ionosphere for F-region heating can be thought of as having a

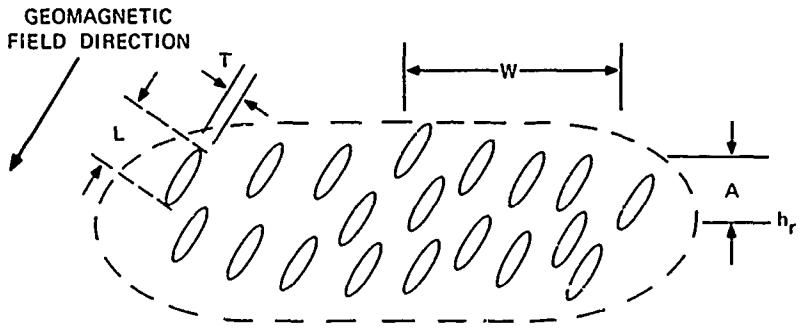

A = SEMI THICKNESS OF HEATED REGION ~7.5 km

W = RADIUS OF HEATED REGION ~50 km

L = LONGITUDINAL (along field) IRREGULARITY SCALE SIZE >10 km

T = TRANSVERSE IRREGULARITY SCALE SIZE 0.5 m, 0.1 m

$\left(\frac{\Delta N}{N}\right)_{RMS}$ = RMS ELECTRON DENSITY FLUCTUATION ~1%

h_r = HEATER REFLECTION ALTITUDE

8727-65-405

FIGURE 14 MODEL PARAMETERS OF SCATTERING REGION FOR F-REGION HEATING

gaussian envelope with a locus of 1/e (-4 dB) points that forms a horizontal disc having a radius of 50 km (the radius of the heater beamwidth at the F region) and a thickness of 15 km centered at the heater reflection altitude. The 1/e locus of this disc as seen from the side is represented by the dashed line in Figure 14 where the plane of the paper represents a vertical plane parallel to the geomagnetic field. Throughout this disturbed region are distributed long, thin field-aligned irregularities that again may be thought of as having gaussian envelopes with average 1/e thickness of 0.1 m to 0.5 m and average 1/e lengths as large as 10 km. Side views of the 1/e loci for typical field-aligned irregularities are shown by solid lines in Figure 14. The rms electron-density-fluctuation producing these irregularities is about 1%.

The horizontal shape of the disturbed region was assumed gaussian for convenience, although it has been found that the effect on the scattering characteristics of assuming some other heater beam shape is not very great. It should be emphasized that the only scattering that a particular radar receives from the disturbed region comes from the intersection with the disturbed region of the field-aligned specular surface for that radar's geometry.

For backscatter, the signal amplitude versus range and Doppler frequency have been measured. Figure 15 shows a typical range Doppler analysis of a swept-frequency CW signal scattered from field-aligned irregularities within the F region. The overall Doppler shift (in this case about +7.5 Hz) varies diurnally over a range of positive and negative values consistent with physical motion of irregularities drifting with the ambient F-region ionosphere (i.e., the Doppler shift increases linearly with radar frequency). The Doppler frequency spread (in this case about 2 or 3 Hz) is also consistent with physical motion of irregularities. Similar Doppler characteristics are observed on the frequency-shifted signals (plasma-line scatter). Practically, these effects are quite small and do not seriously degrade the quality of signals transmitted via the heated region. However, the combination of the Doppler spread and the range depth of the heated region produces signal fading due to fine-scale multipath. For the case shown, an unmodulated CW signal at this frequency would be expected to suffer an average fading rate of two or three fades per second. The detrimental effects of such fading on communications can be reduced by use of diversity reception. Furthermore, the spread in time delay of 1/3 to 1/2 ms would be expected to limit the coherent bandwidth to 2 to 3 kHz. These multipath effects could probably be reduced by using a smaller heater beamwidth or smaller radar antenna beamwidths. For E-region heating, the observed time-delay spreading is

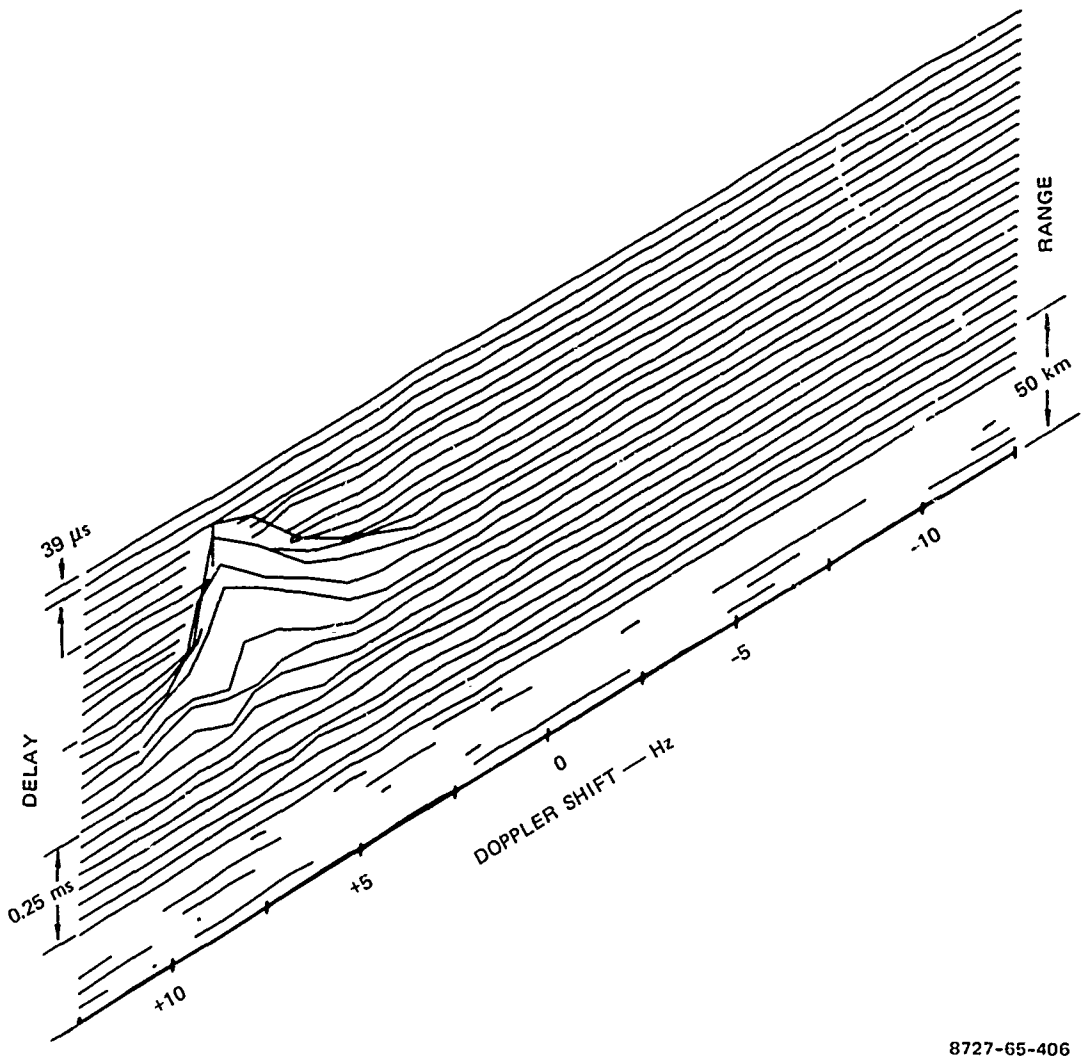

FIGURE 15 BACKSCATTER SIGNAL AMPLITUDE vs RANGE AND DOPPLER SHIFT FOR FIELD-ALIGNED SCATTER AT 44.3 MHz

only about 100 μs (due primarily to geometry difference) and coherent bandwidths of about 10 kHz would be expected.

Measurements of decay and rise time of VHF center-line backscatter in response to sudden heater turn-off and turn-on give some indication that behavior in decay can be interpreted as an outward cross-field diffusion of the field-aligned structures with a diffusion constant at VHF equal to 3 cm^2/s. In this interpretation the decay time goes as λ^2,

which is in qualitative agreement with other observations. The VHF rise time is found to be extremely short, with a cross-section increase of 20 dB in a time period of less than 0.1 s being observed.

A systematic study of the variation in observed cross section with changes in heater power has only recently been undertaken. At the present time, the processes involved in determining the scattering-cross-section "yield" of heater power are not understood. The available data can be modeled using a relation of the form

$$\sigma \propto P^n$$

where

σ = Observed scattering cross section

P = Heater power output

n = Parameter having values between about 0.5 and 1.0.

There are some indications that a better understanding of yield will come from further examination of available data. There appear to be specific times when n above is very nearly 1.0. Also, there is some evidence that, under certain conditions, the cross section may saturate (i.e., increase less rapidly) as the Platteville heater nears full-power output.

E. Field-Aligned Large Electron-Density Fluctuations

The large-scale field-aligned irregularities in ionization produced in the F layer by intense RF heating have been described as artificial spread-F (ASF). To clarify the reason for this description, the properties of ASF and of naturally occurring spread-F (NSF) are briefly described. The name spread-F derives from the appearance produced on a sweep-frequency ionogram by irregularities in F-region ionization.

The leading features of ASF may be compared with NSF as follows:

- ASF occurs on every occasion when ordinary-mode heating is used at a frequency slightly less than f_oF2. However, it appears to be more severe at night for the same heating power.
- ASF occurs in an approximately circular region with radius about 50 km centered slightly north of the heater transmitter, with an onset and decay time of about a minute relative to the time of heating. The intensity of the irregularities is somewhat nonuniform in the horizontal direction, perhaps due to variations in the intensity of heating produced by gross horizontal inhomogeneities in the F layer.
- As with NSF, the irregularities are field-aligned, with maximum intensity in the F-region peak. However, the e-folding distance of the horizontal correlation function of the structures is about one-tenth of the natural scale--namely, about 100 m. The ASF irregularities move horizontally at a speed of a few tens of m/s, apparently corresponding to horizontal motions of the entire F layer.
- For both NSF and ASF the irregularities continue all through the F layer from 200 to about 450 km altitude, their intensity being approximately proportional to the ambient electron density.

1. Ionosonde and HF Phased-Array Observations of ASF

The earliest observations of ASF were made using a vertical-incidence ionosonde located at Erie, Colorado. A typical record from this ionosonde is shown in Figure 16(a). During local nighttime hours, the observed spreading can be even more severe, totally masking the direct F-region traces at the high end of the frequency scale.

The angular spectrum of spread-F returns from an artificially modified ionosphere has been examined by the phased array as a function of range delay (group path), Doppler shift, sounding frequency, and polarization.[10] Figure 16 illustrates the way in which the angle-of-arrival of spread-F returns varies with range delay at a fixed sounding

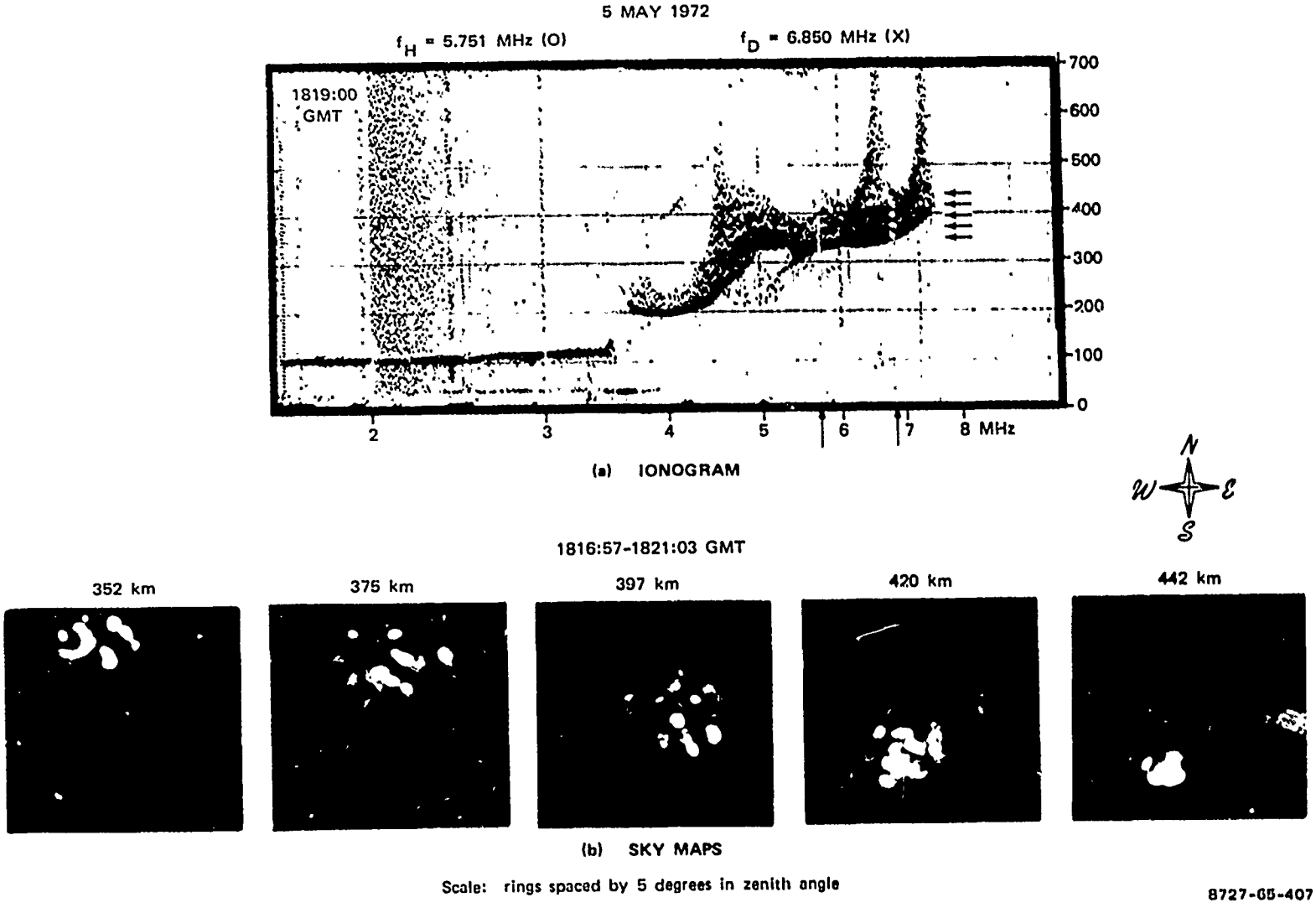

FIGURE 16 DEPENDENCE OF X-MODE ANGULAR SPECTRUM ON VIRTUAL HEIGHT

frequency. The arrows in Figure 16(a) indicate the range delays used in producing the angular spectra of Figure 16(b). The phased array was operating with X-mode polarization at a frequency of (f_D), which was between the O-mode and X-mode critical frequencies. The heater was operating with O-mode polarization at a frequency (f_H) below the O-mode critical frequency. Many such observations have been made, from which the following principal conclusions are listed:

- There is a well defined relationship between the time of arrival of spread-F returns on a given sounding frequency and the angle of arrival of that return: The angle of arrival changes systematically from north to south as the range delay examined is changed from the leading edge of the return to the trailing edge. This behavior is observed for both ordinary and extraordinary returns and over a wide range of frequencies but is most pronounced for extraordinary returns at or near f_xF2.
- The envelope of the volume containing spread-F irregularities extends in height at least over a range from the layer maximum down to 150 km and has lateral dimensions comparable to the heater beamwidth. The volume is tilted so as to be aligned with the earth's magnetic field.
- A systematic Doppler dependence on the angle of arrival of the returns is also observed. The returns arriving at shorter delays that map to the north are found to exhibit predominantly positive Doppler shifts. In contrast, the longer delayed returns arriving from south are Doppler-shifted predominantly to negative.
- It was shown by means of raytracing simulation that the phased-array observations are consistent with the model of field-aligned ducts for the heater-induced spread-F irregularities proposed by Georges.[11]

2. Scintillation Studies of ASF

The transmission experiment is designed to study ASF by examining amplitude fluctuations from orbiting and geostationary satellite signals received at VHF and UHF by receivers spaced at fixed locations on the ground.

In planning the implementation of the transmission experiment, the following objectives were considered as needing to be determined by measurements of ASF irregularities:

- Irregularity orientation.
- Irregularity size and shape.
- Altitude distribution--relative intensity of the electron-density fluctuations as a function of altitude in the disturbed region of the ionosphere.
- Horizontal extent--large-scale horizontal variation of fluctuation intensity in the north-south and east-west directions.
- Onset and decay times.
- Drift velocity.
- Frequency variation (intensity and time scale of amplitude fluctuations of signal transmitted through the heated region as a function of wave frequency).
- Multipath effects.
- Yield studies (effects of transmitter parameters such as heater reflection height, power, and modulation.
- Radar simulation (simulation of scintillation effects anticipated during radar track of objects located behind the disturbed region).

Figure 17 shows the configuration available for a geostationary satellite. ASF irregularities form "shadows" on the ground plane that can be studied by suitably placed receiving antennas A, B, and C. Since all such satellites are located in the equatorial plane, their lines of sight are all somewhat to the south, so the three-station network must be

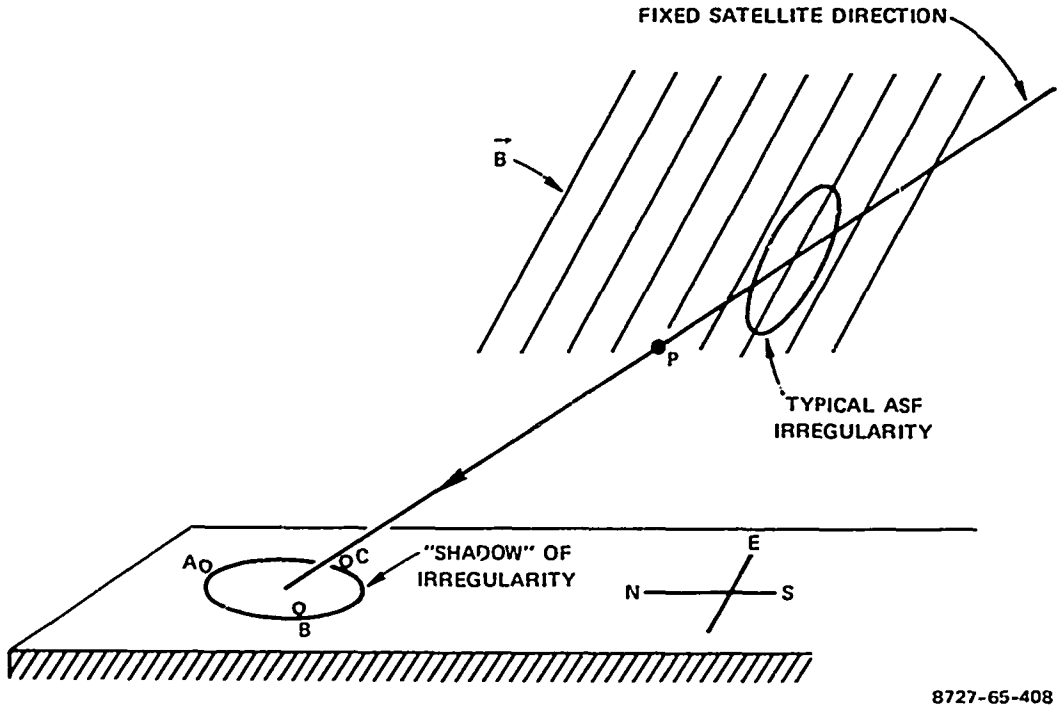

FIGURE 17 CONFIGURATION OF GEOSTATIONARY-SATELLITE EXPERIMENT

offset from the center of the disturbed region in order to allow observation of scintillations. Here, the line of sight is virtually stationary, so the observations obtained are complementary to the orbiting-satellite observations in that time variabilities in the medium are dominant.

The general character of the scintillation observations when the heater transmitter is on is illustrated in Figure 18. The autocorrelation function is nearly gaussian in shape, the fading having an average period of about 10 to 15 s. The unheated quiet ionosphere has a scintillation index (S) less than 0.01, while values of S up to 0.25 have been observed for the heated ionosphere, depending on the heater power and frequency. It is evident that the fading pattern is nearly identical at the three receivers, but simply displaced in time by the amount shown. From this it is concluded that internal velocities in the ionospheric irregularities are negligible, and that the fading is due

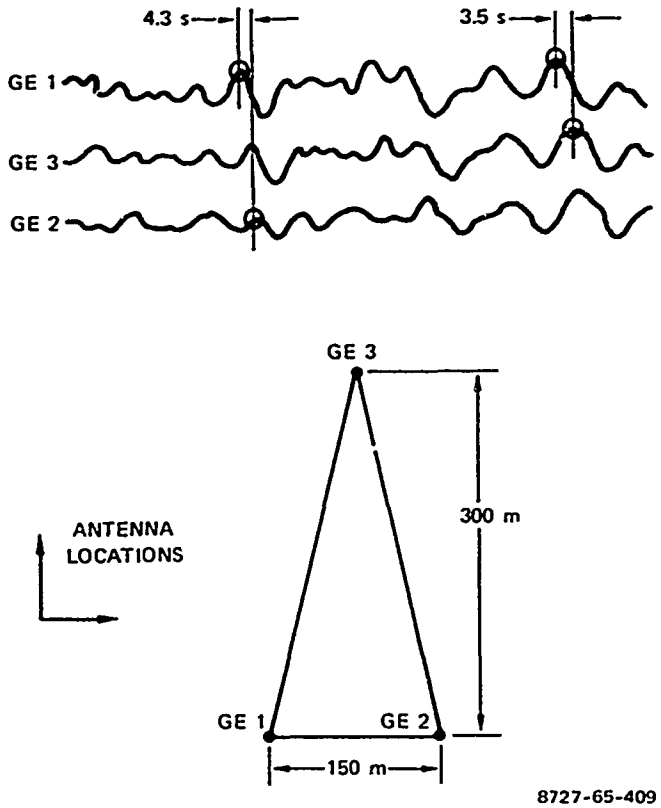

FIGURE 18 ILLUSTRATION OF TIME SHIFTS BETWEEN ANTENNAS, 1323-1325 MDT, 20 OCTOBER 1971

primarily to the drifting of elongated irregularities over the antenna triangle. These data were analyzed by the method of similar fades to give the size of the structure observed at the ground, and the direction and magnitude of the velocity of the irregularities.

Velocities were found in the range from 25 to 125 m/s, from west to east, in reasonable agreement with velocities found by MADRE radar backscatter and the Raytheon vertical-incidence phased array.

The same data can be used to verify the field alignment of the ionospheric irregularities; if this is the case, the direction of the line of maxima should be 7.2° north of east. In fact, values were observed ranging from 4° south of east to 12° north of east. The closeness

of these values to those predicted supports the concept that the irregularities are approximately field-aligned.

Summarizing, the geostationary data show that the disturbed region contains approximately field-aligned irregularities with a correlation distance of about 100 m transverse to the magnetic field, moving in an east-west direction with a velocity of a few tens of meters a second, and with essentially no internal random motion.

The two-frequency transmission experiment using orbiting satellites has been carried out on a substantial number of satellite passes during the past year. Most of these experiments have used ground stations along an east-west line about 100 km north of the heating transmitter at Platteville. Generally, ground observing points have been selected so as to ensure that the LOS to the satellite traverses the center of the disturbed region over the heater. If the satellite passes directly over Platteville, it is possible to choose a site that looks directly upfield through the disturbed region, when the scintillation depth is greatest. However, in general, the angle between the LOS and the magnetic field in the ionosphere goes through a minimum value greater than zero, and the depth of fading is shallower, the greater this minimum value. It is clear that the closer the LOS passes to the magnetic field, the greater the depth of scintillation.

The type of orbital satellite data obtained is well illustrated by Figure 19, which refers to a pass of a U.S. Navy navigational satellite on May 10, 1972, during the PRAIRIE SMOKE II exercise. It shows the variation of the scintillation index at frequencies of 150 and 400 MHz. In each case, the ratio between the indices at the two frequencies is approximately inversely proportional to the wave frequency.

In making a close study of the cross-correlation function of two spaced antennas during an orbital pass, much finer structure was observed,

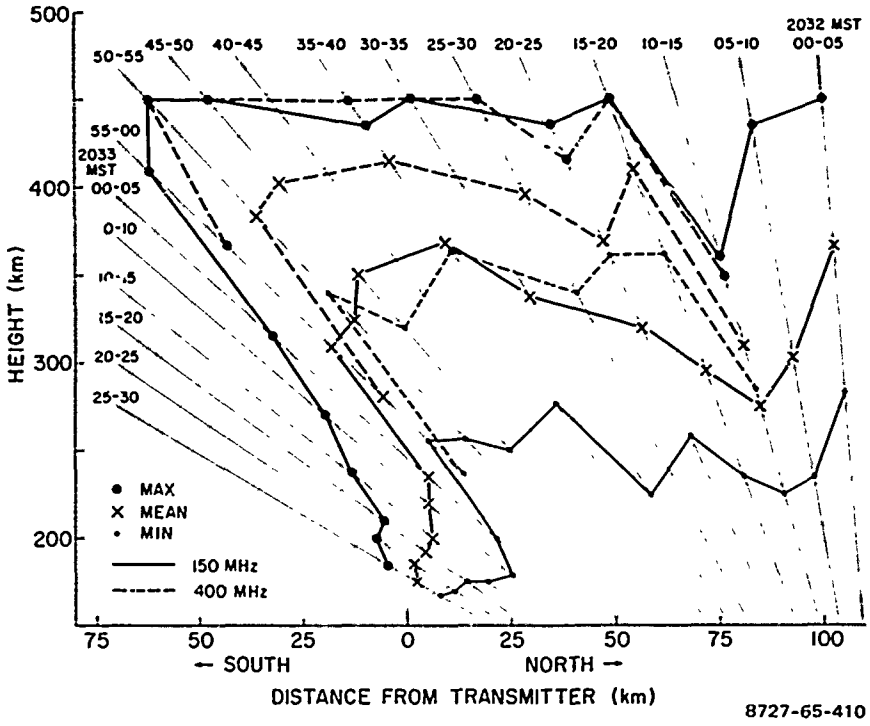

FIGURE 19 RANGE OF HEIGHTS OBSERVED FOR AN ORBITAL PASS

as shown in Figure 20. Analysis of this structure and the larger structure in conjunction shows that their correlation distances appear to fluctuate together but with a ratio of approximately 20 to 1. The conclusions are as follows:

- The field-aligned structure gives strong VHF and UHF scintillations up to 400 MHz.
- The scintillation index maximizes when the direction of propagation is close to the downfield direction. For example, heating the ionosphere upfield from a 150-MHz radar will produce a "blind spot" of about 10° radius centered on the magnetic zenith.
- The fading depth of the scintillation varies inversely with frequency, as would be expected from the integrated phase-path theory of satellite scintillations.
- The transverse scale of the large-scale structure has a half-correlation distance of about 100 m, and

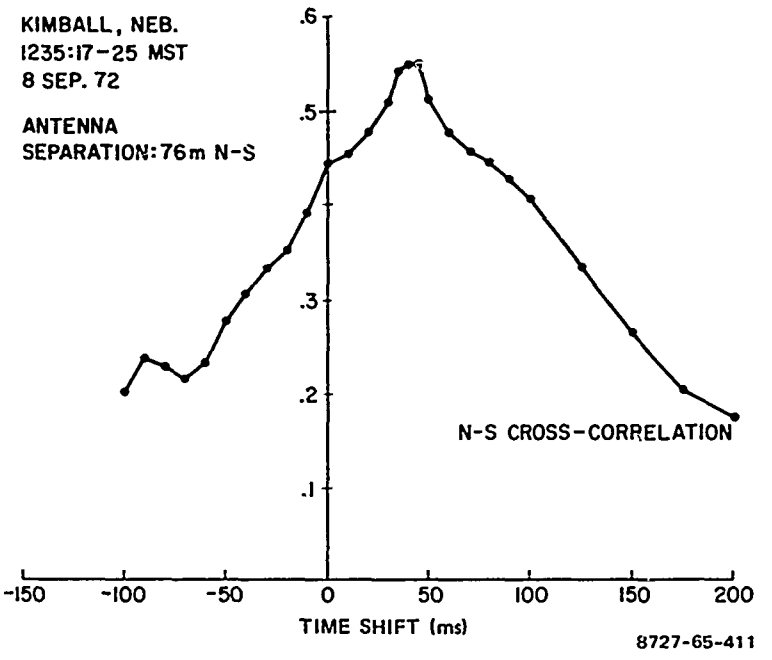

FIGURE 20 SMALLER-SCALE STRUCTURE

convects in an east-west direction with the velocity of the ambient plasma (about 20 to 50 m/s).

- The large-scale structure extends from 200 to 450 km altitude, and is usually confined within a cylinder of about 50 km radius, with its axis the magnetic field line passing through the reflection point directly over the heater.
- Occasionally, unusual shapes for the irregular region are seen, probably arising from a doughnut-shaped disturbed region due to burnthrough of the central core of the ionosphere above the heater.
- A finer-scale structure has been identified, with a scale size of 5 to 10 m, apparently centered close to the reflection height for the heater frequency. This structure is present for extraordinary-mode heating as well as for ordinary-mode, but apparently with smaller intensity.

F. Non-Field-Aligned Fluctuations

At least five scattering experiments have been conducted for two non-field-aligned scattering geometries. The experiments performed were sensitive only to scatterers of a single spatial Fourier component, so no conclusions can be drawn at this time as to the favored orientation of these types of scattering irregularities. Of these five experiments, one (AO incoherent scatter) has provided large amounts of high-quality data on plasma-wave and ion-wave scattering, one has provided a limited quantity of data on ion-wave scattering, one may have very recently detected plasma-wave scatter at Platteville, and two have failed to detect either ion- or plasma-wave scatter at either Platteville or AO. The failure of these last two experiments is the major stumbling block to a general reconcilation of the major experimental observations with presently developed theory.

1. Arecibo Radar Plasma-Line Enhancements

When the ionospheric F region is illuminated with a strong O-mode HF radio wave, excitations of longitudinal plasma and ion acoustic waves are observed by radar scattering. HF-enhanced plasma lines were first observed at the Arecibo Observatory in 1971. A summary of the observations is given by Kantor.[12] The decay line, the growing mode, and image of the decay line are identified and associated with the components of parametric instabilities. The borad line has been recently interpreted by Perkins, Oberman, and Valeo,[13] and Kuo and Fejer.[14] The thickness of the layer producing the observed plasma line is less than 300 m.

Enhancement rise times after HF turn-on have been found to be on the order of tens of milliseconds and show a ringing of the plasma. The period of the ringing was about 8 ms on two measurements made under

the same conditions. This ringing may be the same found by Perkins, Oberman, and Valeo, and Kuo and Fejer.

Decay times of the plasma-line intensity after HF turnoff are about 0.3 to 1 ms, consistent with the linear theory for the frequency range studied. They are primarily due to wave damping by photoelectrons, and are shortest for those waves going in the direction of the largest flux. This has obvious application to photoelectron-flux studies. At night the decay rates are slower by a factor of roughly 2 to 10, again consistent with the linear theory, primarily due to electron-ion collisions. No significant nonlinear damping has been detected yet.

The HF-excited plasma line exhibits spectral features (decay-mode line, growing-mode line, image of decay-mode line), most of which can be explained by parametric instability theory. Some features are not as yet explained. The decay times are consistent with the wave-damping theory and offer a new tool for collision-frequency and photoelectron studies.

2. Ion-Line Enhancement

Figure 21 shows an ion enhancement obtained using coded pulses.

The ion component shows a highly variable amount of enhancement. On two occasions measurement of the autocorrelation function indicated enhanced correlation beyond the first autocorrelation zero crossing, which indicates the presence of spikes in the frequency spectrum at the ion acoustic frequency, as is predicted by the parametric theory. The fact that the cross section increases shows that the effect is due to HF enhancement of the ion line and not only to temperature increase.

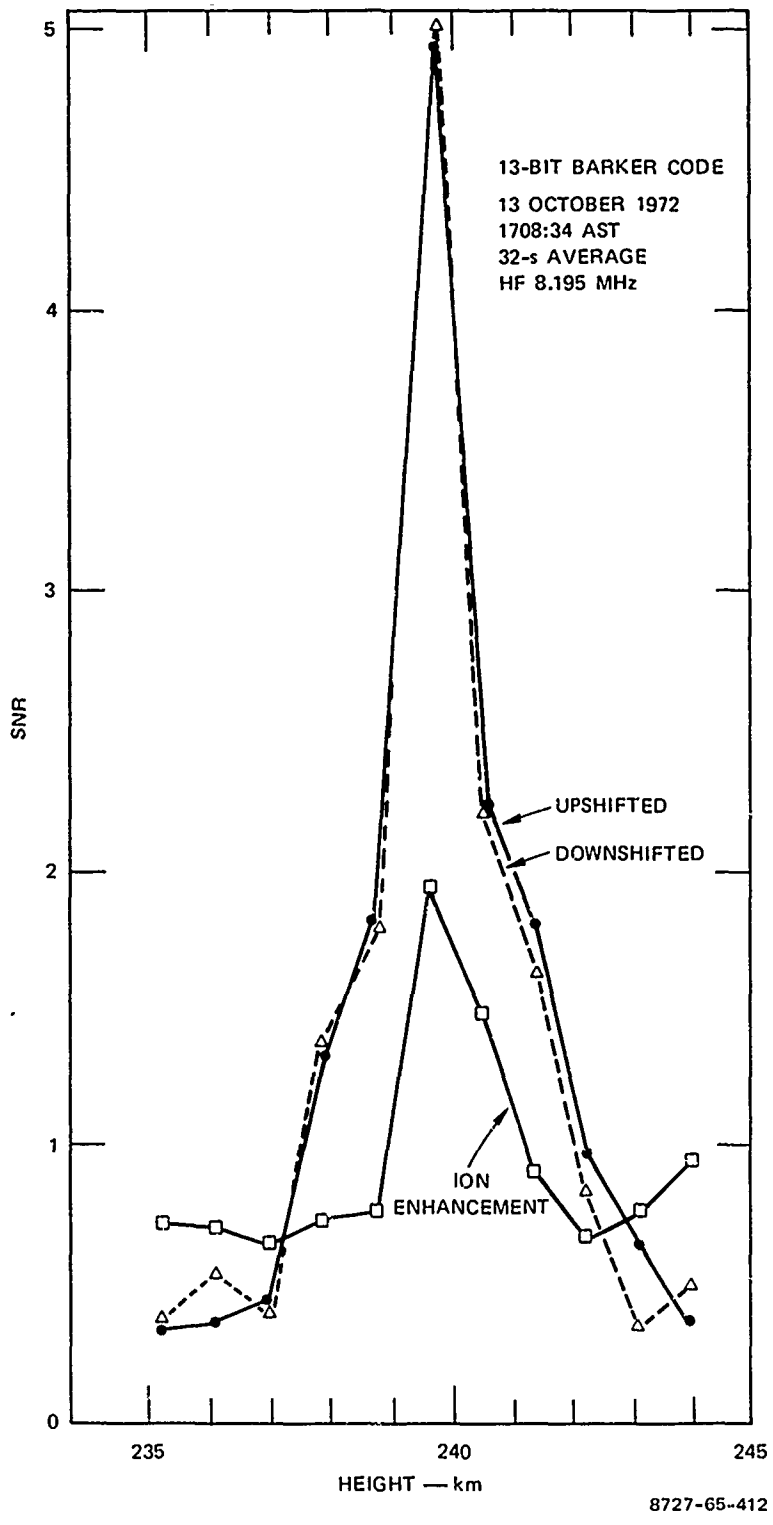

FIGURE 21 BARKER-CODE PROFILE FOR UPSHIFTED AND DOWNSHIFTED PLASMA-LINE AND ION ENHANCEMENT

3. Vertical-Looking Radar at Platteville

During the last quarter of 1973, a vertically directed 350-MHz radar at Erie, Colorado, was employed by ITS in attempts to detect enhanced plasma-line scattering over Platteville.[9] At the present time it appears that detections may have been made. Because this radar is grossly less sensitive than the AO radar, a detection of enhanced plasma-lines at Platteville would imply a significantly greater level for these fluctuations at Platteville than that observed at AO. Such a difference could result from the somewhat higher power density of the Platteville heater and/or from the different geomagnetic field orientation at the two locations.

4. Ion-Wave Scatter from North of the Heated Region

Ion-wave scatter, like plasma-wave scatter, is a relatively weak scattering mechanism requiring sensitive diagnostics for meaningful study. So far it is the only scattering mechanism that has been observed north of the heated region.[15] The magnitude of the scattering cross section was about 10^3 m^2 when observed over a long oblique path oriented to provide scattering from planes normal to the geomagnetic field in the heated region. It was observed on three TV video carrier signals on a single day at frequencies of 55 and 61 MHz. No subsequent observation was attempted. The observed scattered signal appeared as two components shifted in frequency above and below the incident frequency by about 200 Hz--a value comparable with Doppler shifts expected for F-region ion-acoustic waves. Very little is empirically known about the maximum magnitude or geometrical and frequency dependencies of ion-wave scatter, but their observation in this geometry indicates that plasma-waves having the same orientation should be present.

5. Plasma-Wave Scatter from North of the Heated Region

Two experiments, possibly of marginal sensitivity, have been conducted in an effort to verify theoretical predictions of strong plasma waves propagating in a small cone of angles about the geomagnetic field direction. One attempt has been made at each of the heating facilities. No scattering, at least of the magnitude expected from theoretical studies, was found. It appears that these negative results are in such disagreement with otherwise acceptable theories that a repetition with greater sensitivity and using a range of probing frequencies is warranted.[9]

IV MODELS

A. General

A model for the "on-frequency" field-aligned scattering has been developed on the basis of the work performed to date by all the members involved in the modeling task. The model is intended primarily for use in systems applications and its presentation format has been adopted adopted accordingly. An attempt is made here to present the model in a form that would best meet its intended objective, and it is hoped that it reflects the consensus of the modeling group.

The formulation of the model begins with a physical description of the scattering medium that specifies the dimensions of the disturbance, the wavenumber spectrum of the density fluctuations, and a yield model relating the fluctuation intensity to the heater power density. The characterization of the medium is an important aspect of the modeling task and we strive in this presentation to see that it is consistent with all the available observations to the best possible extent. It is followed by a description of the radar properties of the disturbed volume where the concepts of aspect sensitivity and surface of specularity are introduced, as well as the underlying principle relating the bistatic and monostatic scattering geometries. The mathematical component of the model is only summarized here; detailed derivations have been given elsewhere.[16] It is presented in two parts, each representing a different degree of sophistication in computing the total radar cross section. The first part is concerned with a general case where a bistatic geometry and a realistic yield model are considered and it involves a numerical approach. The second part, considering a monostatic geometry and an idealized

yield model, offers an analytic solution. This case is of interest since a general bistatic radar problem can be reduced to an equivalent monostatic case and can be evaluated to first order without resorting to a complex computer program. Finally a schematic flow diagram is given for computer adaptation of the model.

B. Physical Description of the Scattering Medium

1. Dimensions of the Disturbance

The physical model of the disturbance generated by the Platteville heater is shown pictorially in Figure 22. The disturbed volume containing the small electron-density fluctuations responsible for the field-aligned scattering of the radio waves is a diffuse region centered above the heater at the height where the heater frequency equals the local ionospheric plasma frequency. The strength of the irregularities falls off above and below this altitude with a gaussian scale length of 7.5 km (15 km between 1/e points). The lateral dimensions of the volume are set by the width of the heater antenna beam: for the Platteville heater this sets the gaussian radius of the disturbed volume at 50 km (100 km between 1/e points) for a heater reflection height of 240 km. The disturbed volume can thus be visualized as a flat pancake-shaped region with diffuse boundaries. At the center of the disturbed volume the rms intensity of the electron density fluctuations is typically 1 to 1.5% when the heater is operating at its full power of 1.9 MW. The physical description of the disturbance presented here has been arrived at primarily by requiring the resulting scattering model to be consistent with the radar observations.

2. Wavenumber Spectrum

The wave spectrum of the density fluctuations of the scattering medium is related to the backscatter coefficient σ_v as:[17]

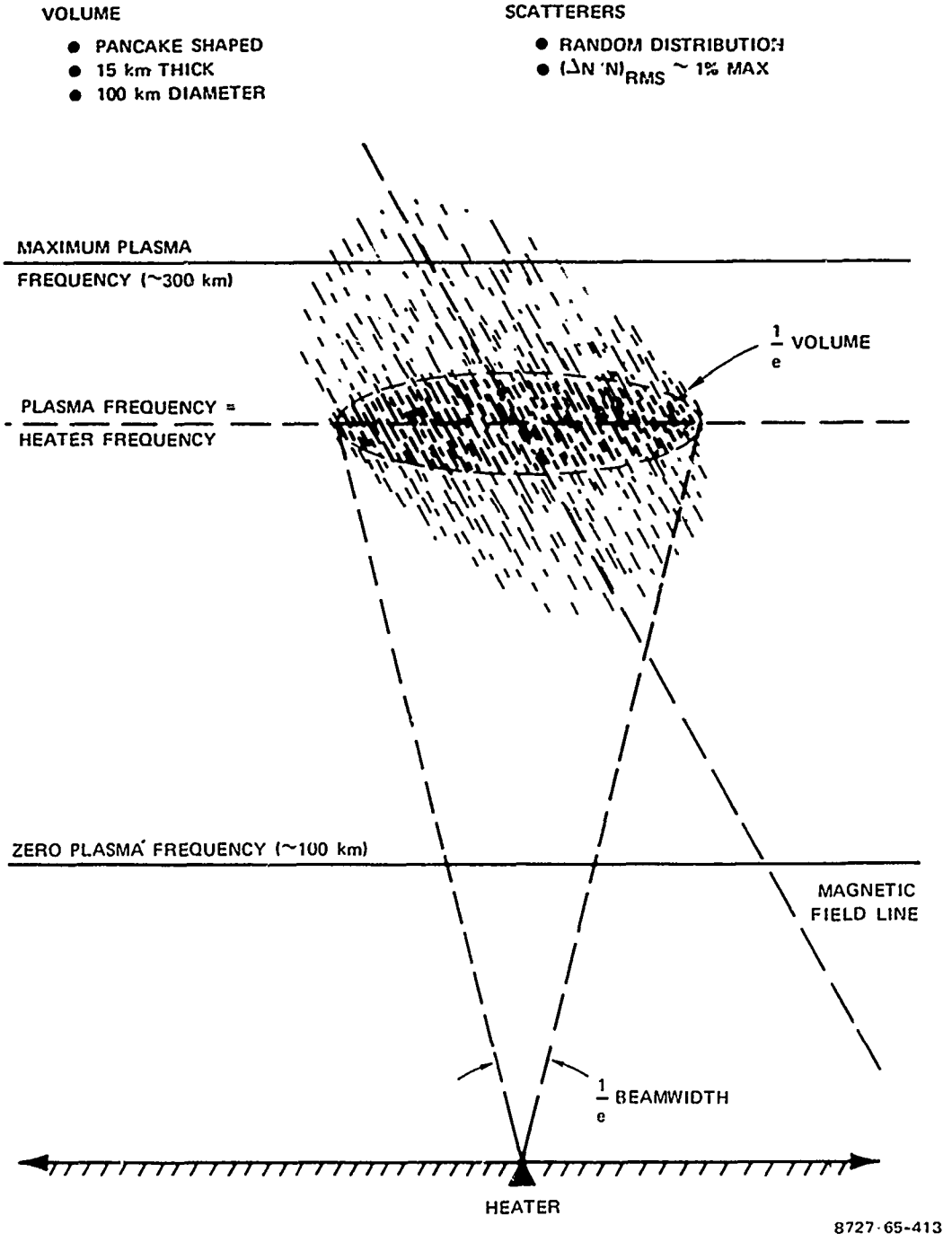

FIGURE 22 PHYSICAL MODEL OF THE VOLUME CONTAINING ELECTRON-DENSITY IRREGULARITIES RESPONSIBLE FOR "ON-FREQUENCY" FIELD-ALIGNED SCATTERING

$$\sigma_v = \frac{\pi^2}{\lambda_N^4} \overline{\left(\frac{\Delta N}{N}\right)^2} \; P\,(2\,K\ell,\ 2\,Km,\ 2\,Kn) \quad . \qquad (1)$$

In the case of strongly aspect-sensitive scatter, the three-dimensional wavenumber spectrum can be written in separable form or as:[18]

$$P\,(2\,K\ell,\ 2\,Km,\ 2\,Kn) = P_{\perp}\,(2\,K\ell,\ 2\,Km)\,P_{\parallel}\,(2\,Kn) \qquad (2)$$

where the two components are defined in terms of the corresponding spatial correlation functions. Using Eq. (2), and the approximations associated with the high aspect sensitivity of the scatterers, a relation between σ_T, the total radar cross section, and the axially symmetric transverse spectrum $P_{\perp}$ (2K) was derived by Pendyala and Thome as:[16]

$$\sigma_T\,(K) = \left\{ \frac{4\,\pi^5\,W^2\,R\,\overline{(\Delta N/N)_o^2}}{\lambda_N^4\,(\cos^2\theta + \frac{W^2}{A^2}\sin^2\theta)} \right\} \frac{P_{\perp}\,(2K)}{K} \qquad (3)$$

where θ is the tilt angle of the specular surface from horizontal, W and A are the horizontal and vertical gaussian scale sizes of the disturbance, λ_N is the background plasma wavelength, R is the range, and K is the radar wavenumber. An integral form of Eq. (3) allows one to determine the rms density fluctuations from the radar measurements as shown in Ref. 16. Using the radar observations of σ_T shown in Figure 23, the transverse spectrum and the density fluctuation intensity are evaluated for the following parameters:

λ_N = 54 m

$\theta = 10°$

W = 75 km

A = 7.5 km

R = 900 km.

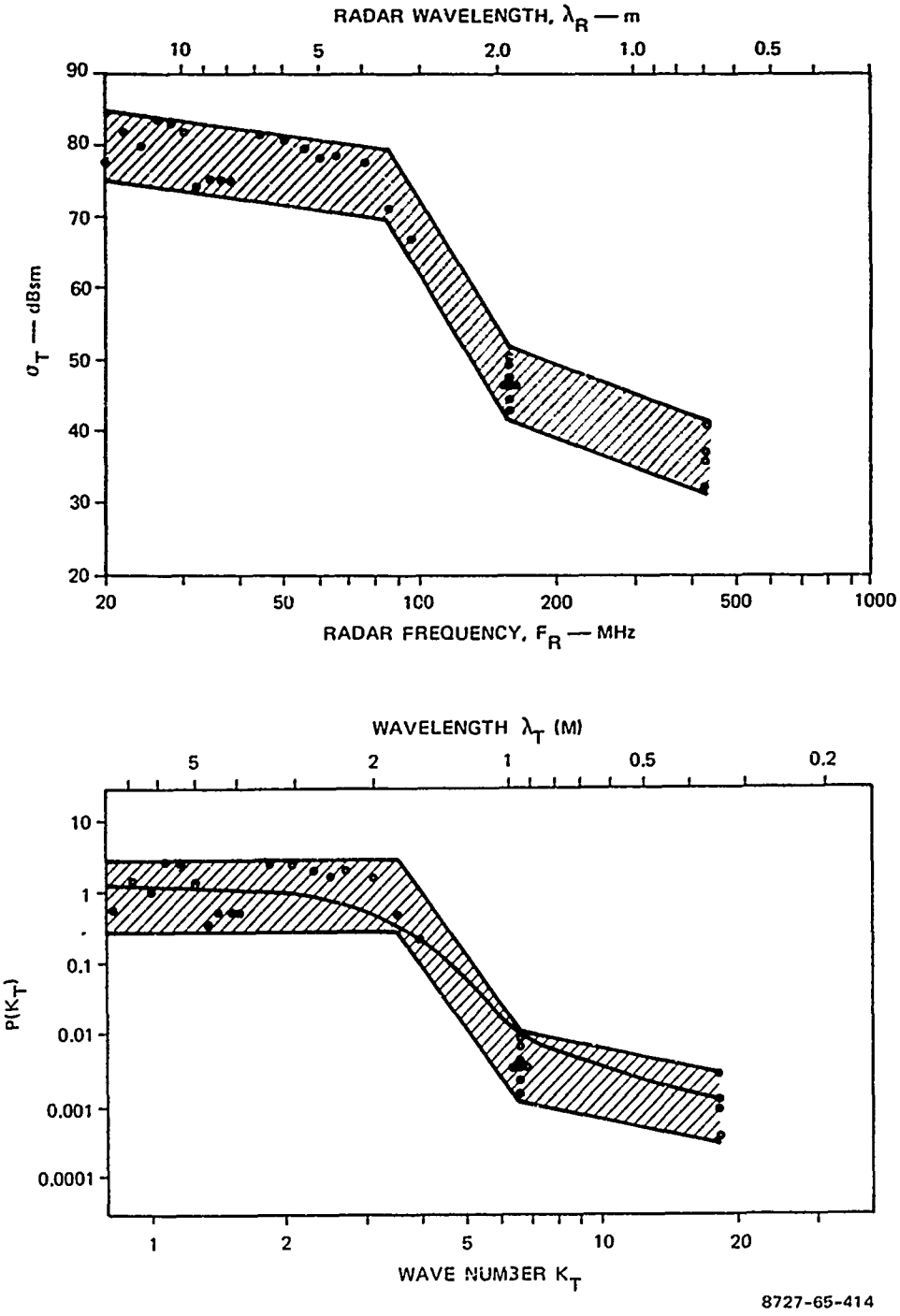

FIGURE 23 MEASUREMENT OF TOTAL RADAR CROSS SECTION AND THE DERIVED TRANSVERSE-WAVENUMBER SPECTRUM OF DENSITY FLUCTUATIONS

The rms density fluctuation was obtained as:

$$(\Delta N/N)_{rms} \approx 1.5\% \quad .$$

The transverse spectrum derived from the radar observations is also shown in Figure 22. It is a three-segment spectrum such that

$$\begin{aligned} P(K_T) &= 0.4 && (0.8 \leq K_T \leq 3.3) \\ &= 0.8 \times 10^{4} K_T^{-8.3} && (3.3 \leq K_T \leq 6.6) \\ &= 0.8 \times 10^{-2} K_T^{-1.1} && (6.6 \leq K_T \leq 18.23) \quad , \end{aligned}$$

The curve through the hatched region of the wavenumber spectrum represents a double-gaussian fit of two correlation scale sizes.

3. Yield Model [$\overline{(\Delta N/N)}^2$ Dependence on Heater Power Density]

One of the important elements of the scattering model is the density-fluctuation intensity $\overline{(\Delta N/N)}^2$. A model as to how this quantity depends on the heater power density, referred to as yield model, is presented in this section. There are two ways to arrive at the desired model on the basis of the radar observations relating the total cross section σ_T to the heater power P_H. One involves performing a numerical inversion of the observed radar data to obtain the required solution. The other method is indirect, in that a model will be assumed to start with, and will be tested for its validity by synthesizing the radar cross sections and comparing them with the measurements. The second method has been adopted here since it is relatively simpler. It is assumed in the analysis given here that the heater power affects only the intensity and not the spectrum of the density fluctuations.

Radar observations from PRAIRIE SMOKE V show a wide variability in the radar cross-section yield as a function of the heater power. The

results may be classified into two types: one revealing a constant slope and the other revealing a variable slope with the heater power. Most measurements fall into the first category, and they are shown in the form of scatter plot in Figure 24. The cross section has a power-law dependence on the heater power, with the exponent ranging over 0.3 to 1 with a median value of about 0.65. In the case of SRI data, it was found that lower slopes are in general associated with the conditions when the heater is operating close to the critical frequency. For these measurements of constant slope, the yield model relating $\overline{(\Delta N/N)}^2$ to the heater power density is the same as that relating the cross section to the heater power. In some instances, the second type of behavior with variable slope is noted, although the conditions under which this happens are not yet identified. Influenced by the observed behavior, we have started with a simple two-step model with density fluctuations increasing linearly with power density up to a certain level and 0.33 times as rapidly above that level (Figure 25). Based on the model, the computation of the normalized total cross section as a function of the heater power proceeds as described earlier by Pendyala and Thome.[16] Briefly it is as follows:

First, the power density distribution on the heater reflectrix is obtained using a gaussian pattern for the heater antenna. The next step involves converting the power density to density fluctuation using the functional dependence shown in Figure 25. In order to compute the radar cross section, however, the density fluctuations had to be calculated on the specular surface. Using the geometry shown in Figure 26, the following expression involving an arbitrary constant C is derived for the total cross section σ_T (Pendyala and Thome):[16]

$$\sigma_T = C \int_0^{\infty} \int_0^{2\pi} \overline{(\Delta N/N)}_R^2 \exp - (d/A)^2 \frac{R}{\cos^2 \theta} \, dR \, d\Phi \quad . \qquad (4)$$

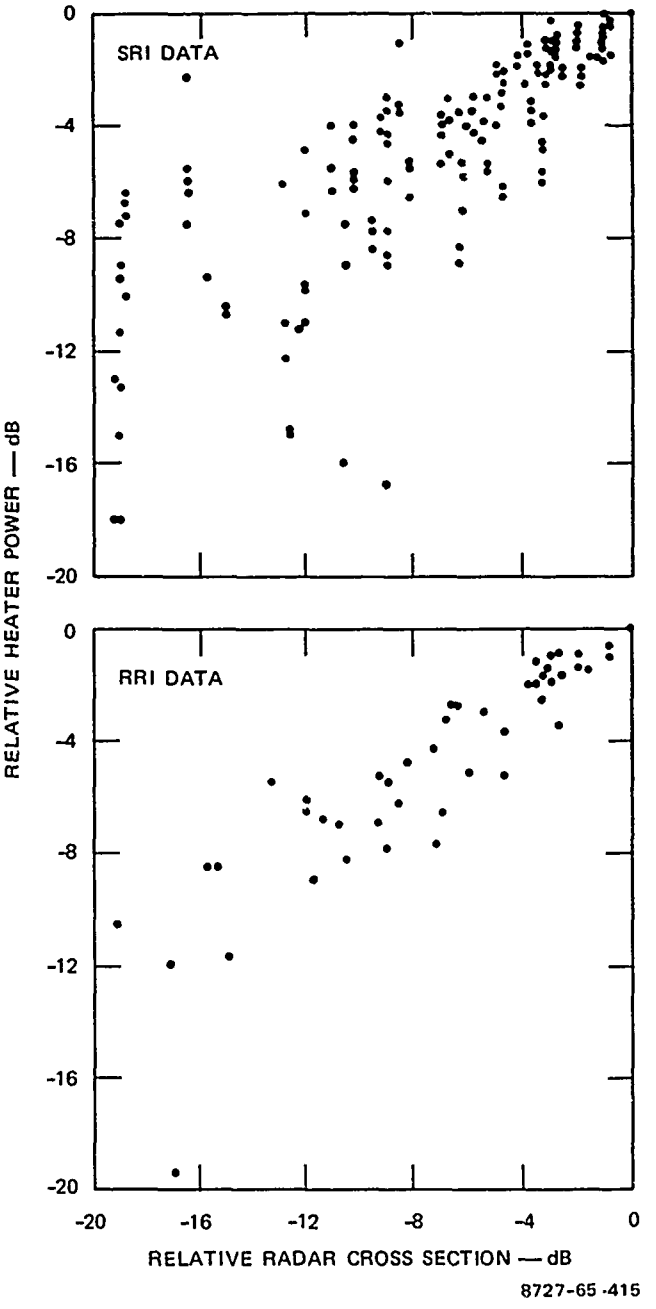

FIGURE 24 SCATTER PLOTS OF THE YIELD MEASUREMENTS CONDUCTED BY SRI AND RRI DURING PRAIRIE SMOKE V REVEAL CONSTANT-POWER-LAW DEPENDENCE OF RADAR CROSS SECTION ON HEATER POWER, FOR ANY INDIVIDUAL RUN

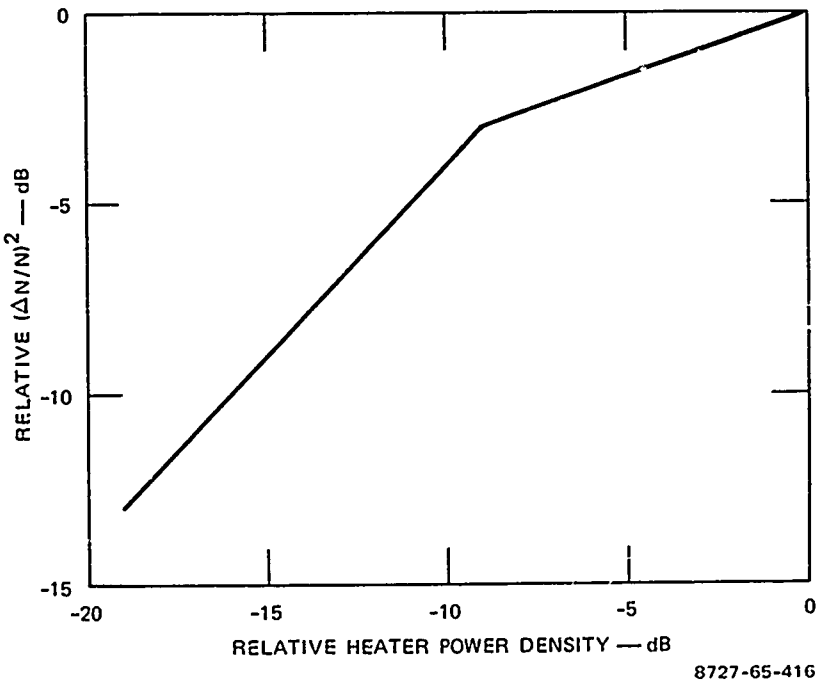

FIGURE 25 THE TWO-STEP YIELD MODEL FOR $\overline{(\Delta N/N)^2}$ ON WHICH THE COMPUTATIONS ARE BASED

The above surface integral is numerically evaluated by dividing the surface into concentric rings as shown in Figure 26. The outermost ring encloses all the area of interest with dimensions twice the gaussian diameter of the disturbance. The cross section is calculated for different power values relative to its value when the heater is operating at the maximum power. Figure 27 shows a comparison between the synthesized (dashed curve) and the observed cross-section dependence on the heater power. Given the uncertainties in the yield measurements, the simple model presented here can be considered adequate to account for the power dependence of the radar cross section. Some caution should, however, be exercised in adopting a simple yield model because of the wide variability seen in the measurements.

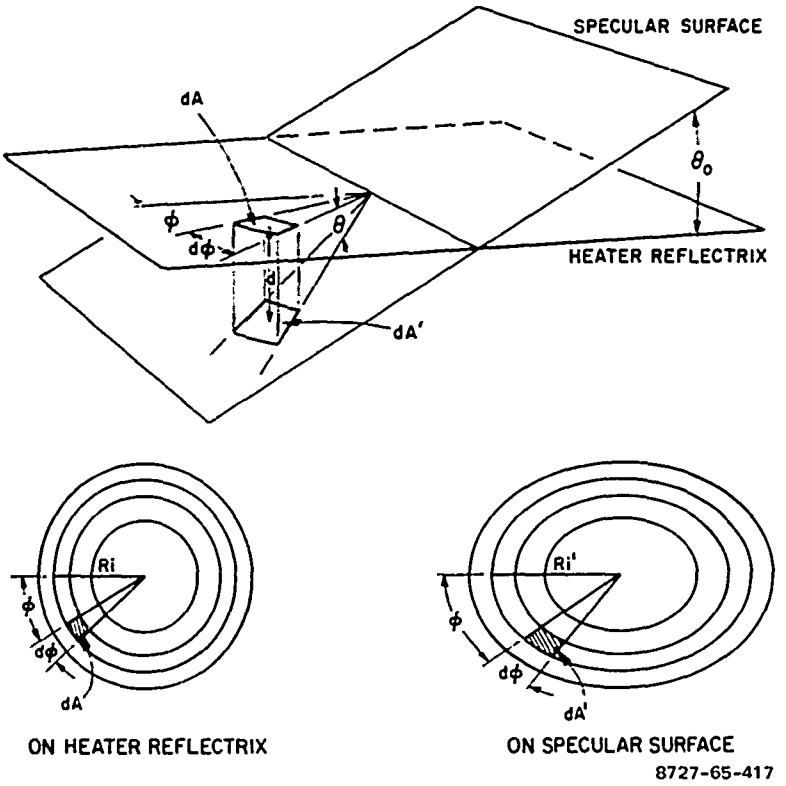

FIGURE 26 THE SPECULAR-SURFACE/HEATER REFLECTRIX GEOMETRY ADOPTED IN DERIVING THE YIELD MODEL

C. Radar Properties of the Disturbed Volume

1. Aspect Sensitivity and the Concept of a Surface of Specularity

The high aspect sensitivity of the scatterers leads to an important modeling concept--the surface of specularity. The importance of the concept is, first of all, that it helps to physically understand the radar results, and secondly, that it reduces the numerical task of computing radar scattering cross sections from a 3-dimensional problem to a 2-dimensional problem. Consider first the optical analog shown in Figure 28. The glass rods are aligned with the earth's field and represent the small field-aligned fluctuations in refractive index caused by heating the ionosphere. The light from the candle flame is partially reflected by the glass rods, and an observer behind the candle sees an image of the flame at the specular point on each rod. If there are

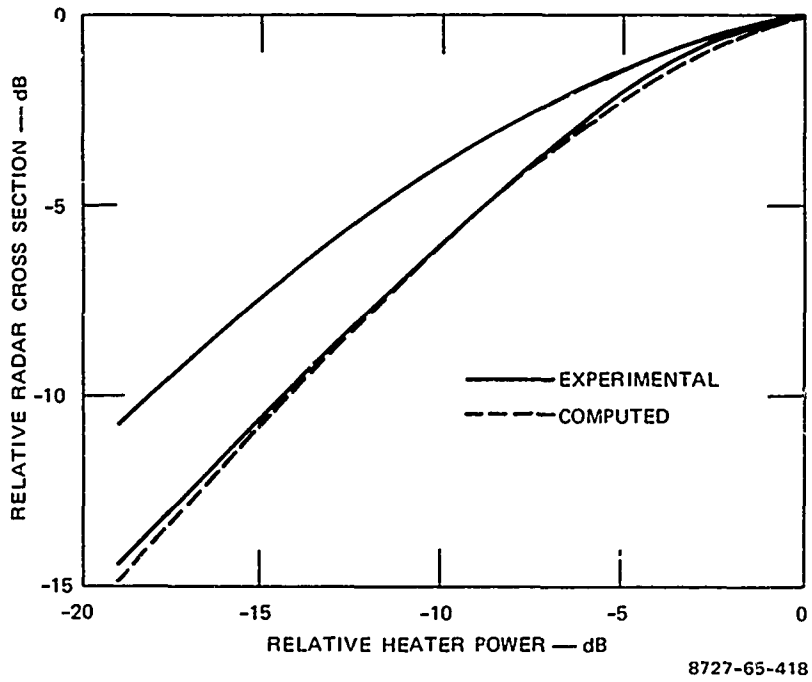

FIGURE 27 COMPARISON BETWEEN EXPERIMENTAL AND COMPUTED RADAR CROSS-SECTION DEPENDENCE ON HEATER POWER

many closely spaced rods, the images from each will blend together to form a bright "specularity surface" on which the specular points for all rods lie. The only part of the rod that matters for the observer is the segment that coincides with the specularity surface. The corresponding picture for the radar case is shown in Figure 29. The glass rods have been replaced by the field-aligned electron-density irregularities caused by the heater. In this case, the height where the heater frequency matches the local plasma frequency is well above the specularity surface for the radar and consequently only the weak lower tips of the irregularities are "seen" by the radar. The received signal strength will consequently be weak. The situation can be improved by lowering the heater frequency (and consequently the height where the heater frequency matches the plasma frequency) till the disturbed volume coincides with the surface of specularity. The concept is qualitatively the same for bistatic as well as for monostatic paths. The procedure is to compute the surface of specularity,

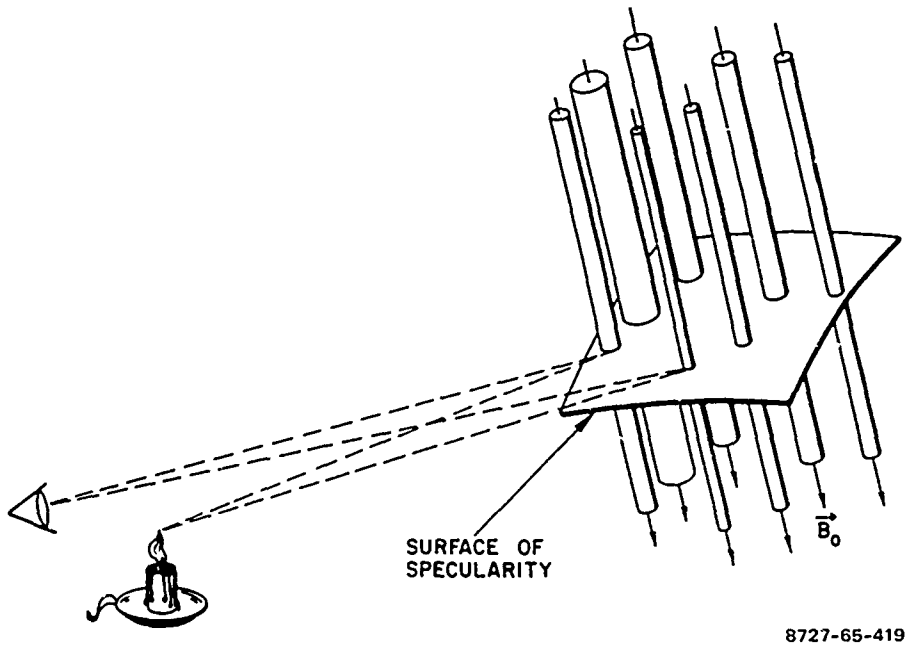

FIGURE 28 ILLUSTRATION OF THE OPTICAL-ANALOG CONCEPT OF A SURFACE OF SPECULARITY FOR REFLECTIONS FROM A BUNDLE OF CLOSELY SPACED FIELD-ALIGNED SCATTERERS (glass rods)

given the end points of the path and a model of the earth's field, and then use the strength of the scatterers lying on the surface to compute the effective scattering cross section of the disturbed volume. This converts the computational problem from a volume integration to a surface integration with a corresponding reduction in complexity.

2. Bistatic vs Monostatic Scattering Geometries

When the receiver and transmitter of a communications path are separated from each other (bistatic rather than monostatic operation) the scattering properties of the disturbed volume are modified. The principal modification is that the size of the irregularities that support scatter over bistatic paths is larger than the size that supports back-scatter at the same frequency. The situation is shown in Figure 30. The Bragg condition for constructive interference says that the spatial Fourier component, which counts in determining the strength of the wave

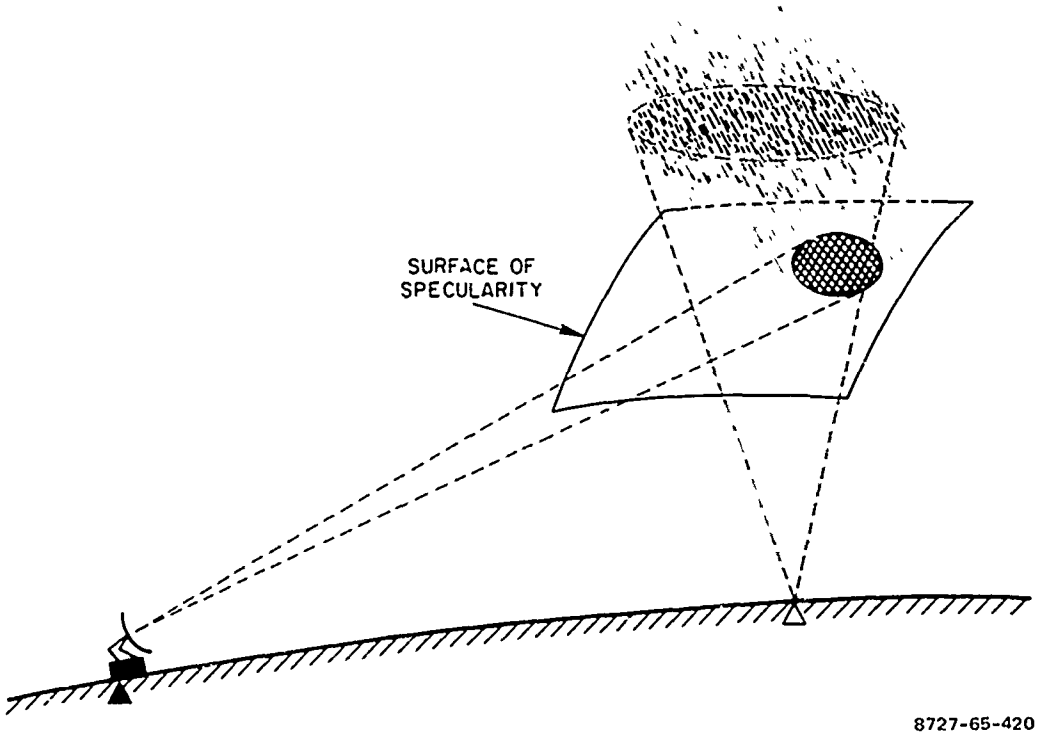

FIGURE 29 THE SURFACE OF SPECULARITY FOR THE BACKSCATTER-RADAR CASE

scattered through an angle θ, is the component of spatial wavelength $s = \lambda/2 \sin(\theta/2)$, where λ is the wavelength of the incident radio wave. When this condition is met, the waves scattered from adjacent crests of the spatial Fourier components will differ in phase by exactly one wavelength and thus will add coherently in the direction of interest. Figure 30 illustrates the fact that the spatial wavelength of interest becomes longer as the path changes from monostatic to bistatic. Since the strength of the spatial frequency spectrum increases monotonically as the wavelength becomes longer (see Figure 23), the disturbed volume will scatter more strongly over a bistatic path than over a backscatter path, all else being equal.

The "bistatic gain" predicted by the model for a 90° scattering angle is shown in Figure 31. The shaded area shows the range in which

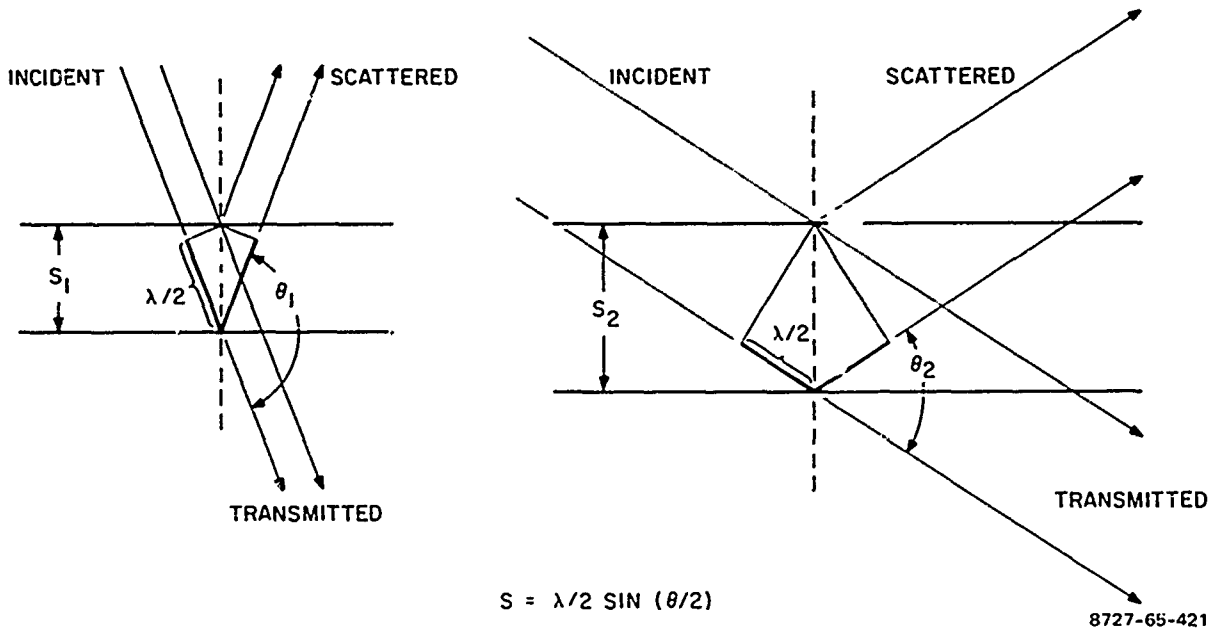

FIGURE 30 ILLUSTRATION OF BRAGG SCATTERING SHOWING THAT THE WAVELENGTH OF THE SPATIAL-FREQUENCY COMPONENT THAT CONTROLS THE STRENGTH OF THE SIGNAL SCATTERED THROUGH AN ANGLE θ INCREASES AS THE SCATTER GEOMETRY CHANGES FROM MONOSTATIC TO BISTATIC

backscatter measurements of total radar cross section fall as a function of frequency. The solid "backscatter" curve shows that the model predictions are in agreement with the observations, and the solid "bistatic" curve shows the increase in cross section expected for a 90° scattering angle. Gains of 10 dB or more can be expected, depending on frequency.

D. Mathematical Model for σ_T

1. General Case (Bistatic Geometry and Realistic Yield Model)

The formulation of the mathematical model presented in detail elsewhere[16] involves, basically, the derivation of an expression for the radar cross section per unit area σ_A on the specular surface. The total radar cross section per unit volume σ_T is computed by numerical evaluation

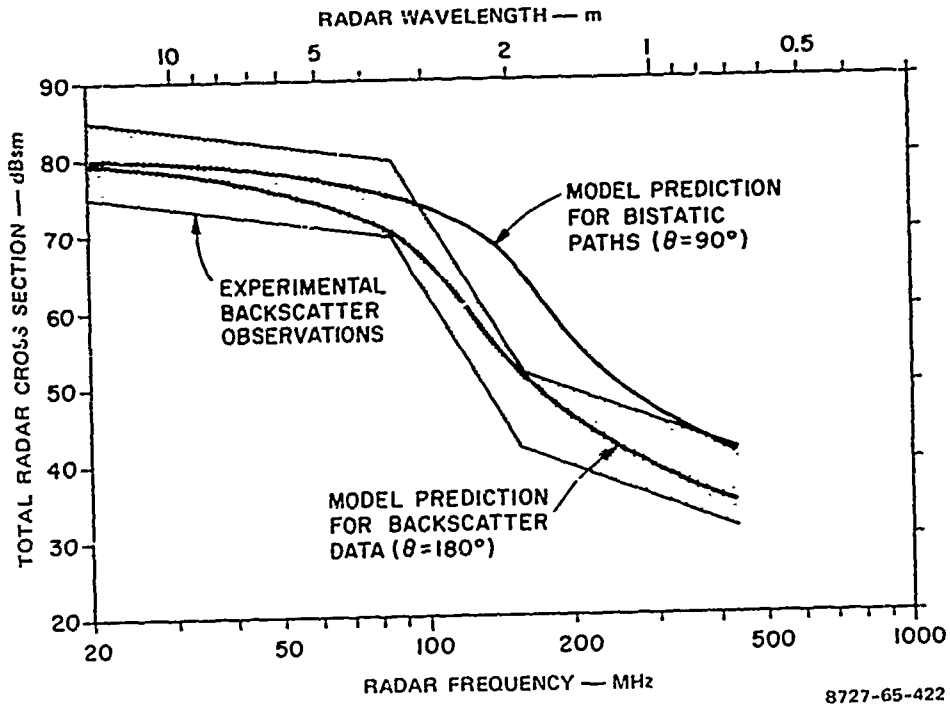

FIGURE 31 A COMPARISON BETWEEN EXPERIMENTAL BACKSCATTER MEASUREMENTS OF THE TOTAL RADAR CROSS SECTION OF THE DISTURBED VOLUME AS A FUNCTION OF FREQUENCY, MODEL PREDICTION FOR BACKSCATTER, AND MODEL PREDICTION FOR A 90° BISTATIC PATH

of the surface integral of σ_A. The radar cross section per unit volume σ_V of the scattering medium, which must be integrated along the direction normal to the specular surface to obtain σ_A, is expressed by Booker as:[17]

$$\sigma_V = \frac{\pi^2 \sin^2 \chi}{\lambda_N^4} \overline{(\Delta N\, N)}^2 P\{K(\ell_2 - \ell_1), K(m_2 - m_1), K(n_2 - n_1)\} \qquad (5)$$

where

χ = Angle between incident E vector and the direction of scattering

λ_N = Background plasma wavelength

(ℓ_1, m_1, n_1) = Direction cosines of incident wave vector

(ℓ_2, m_2, n_2) = Direction cosines of scattered wave vector.

Resolving the three-dimensional wavenumber spectrum into parallel and transverse components and using the yield and wavenumber spectrum models described earlier, Eq. (5) is integrated with respect to z to obtain the cross section σ_{Ai} for the elemental area dAi of the specular surface shown in Figure 32. σ_{Ai} is obtained as:[16]

$$\sigma_{Ai} = \frac{\pi^2 \sin^2 \gamma_i}{\left[1 + \frac{\lambda^2 R^{1^2} \cos^2 \gamma_i}{8\pi^2 L^2 A^2}\right]^{1/2}} \frac{\lambda R^1}{2} \frac{\overline{(\Delta N/N)}_i^2}{\lambda N_i^4} P_\perp (2K \sin \phi_{si}/2) \qquad (6)$$

where L is the longitudinal gaussian correlation scale size of the irregularities, γ_i is the complement of the dip angle, ϕ_{si} is the scattering angle, λ is the operating wavelength, and $R^1 = 2R_1R_2/(R_1 + R_2)$, R_1 and R_2 being the ranges from transmitter and receiver to the scattering volume. The total cross section is obtained by numerical evaluation of the surface integral of σ_A. Thus

$$\sigma_T = \int_S \sigma_A \, dA = \sum_{i=1}^{i=N} \sigma_{Ai} \, dA_i \qquad (7)$$

where N is the number of elements into which the active region of the specular surface is divided.

2. Special Case (Monostatic Geometry and Idealized Yield Model)

The scattering model for the total cross section can be presented in an analytic form for the special case of a monostatic geometry and an idealized yield model. The solution is of some interest since a general bistatic radar problem can be reduced to an equivalent monostatic case and can be evaluated to a first order without resorting to a complex

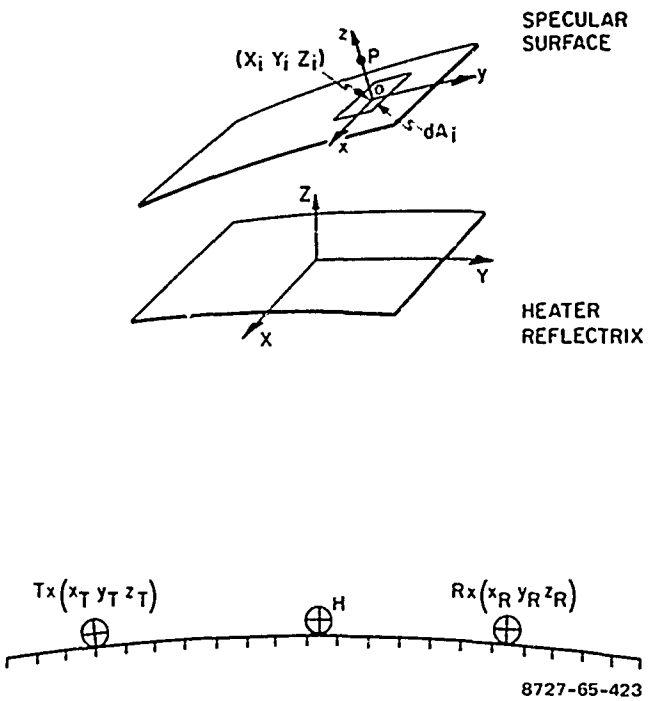

FIGURE 32 SKETCH OF BISTATIC-RADAR GEOMETRY SHOWING THE COORDINATE SYSTEMS ON THE SPECULAR SURFACE AND THE HEATER REFLECTRIX USED IN THE MODEL

computer program. The approximate nature of the solution is a consequence of two simplifying assumptions that readily permit an analytic description to the model. The assumptions are that the magnetic field is constant over the dimensions of the scattering volume and that the intensity of the density fluctuations is directly proportional to the power density on the heater reflextrix. Starting with Eq. (1) and following the steps given by Pendyala and Thome,[18,19] we obtain the following equivalent monostatic form for a bistatic radar illuminating the entire disturbed volume:

$$\sigma_T(K) = \frac{2\pi^4 \sin^2 \chi\ W \lambda R^1}{\lambda_N^4} \left(\frac{\overline{\Delta N}}{N}\right)_o^2 \exp - \{D^2/A^2\}\ P_\perp (2K \sin \phi_s/2) \left[\cos^2\theta + \frac{W^2}{A^2}\sin^2\theta\right]^{-1/2} \qquad (8)$$

where D is the on-axis mismatch distance between heater reflectrix and specular surface, ϕ_s is the scattering angle and the equivalent range $R^1 = 2 R_1 R_2/(R_1 + R_2)$. The above equation will be useful for the purpose of quick evaluation of a given radar link. The reader is referred to Pendyala and Thome[16] for an expression when a pulse radar is employed and only a portion of the disturbance is illuminated.

E. Model Verification

According to the model presented above, there will be an enhancement in the radar cross section to be gained by going from monostatic to bistatic configuration when operating in the region where the spectral function $P_\perp(K_T)$ decreases with the increasing wavenumber. A multistation CW scattering experiment designed to verify the model prediction was conducted by SRI using an operating frequency of 144 MHz that falls in the region of steep slope of the cross section-versus-frequency curve (Frank et al., 1973).[20] The experiment involves a comparison of the cross sections observed over a near-backscatter path with $\phi = 168°$ (Ocotillo-Lancaster) and a forward-scatter path with $\phi_s = 89°$ (Ocotillo-Huntsville). The observations show a 10-dB gain in the cross section for the forward-scatter path relative to the backscatter case. The scattering model predicts an enhancement of about 14 dB on the assumption that the polarization and mismatch effects are small. The difference noted between the model prediction and the observation is considered to be within the error bounds of the experiment.

F. Analytical Model for ASF

The easiest aspect of ASF to quantify is its effect on a UHF radio signal transmitted through the ionosphere. Such a signal undergoes a random phase perturbation with rms value γ, in radians, given by

$$\gamma^2 = \frac{\pi^{5/2}}{\lambda^2} \left(\frac{f_o F2}{f}\right)^4 \int_0^{h_s} D \sec i \operatorname{cosec} \psi \, g^2 (x,y,h) \left(\frac{N}{N_m}\right)^2 dh \qquad (9)$$

where λ is the wavelength of the probing signal, and f is its frequency; $f_o F2$ is the ordinary-wave critical frequency of the F2 layer; D is the e-folding correlation distance of the ASF irregularities transverse to the magnetic field; i and ψ are the angles the line of sight makes with the vertical and the magnetic field, respectively; g is the rms fractional deviation in electron density; and N/N_m is the ratio of the electron density at height h to that at the F-layer maximum. Now consider a satellite height h_s that is far above the F-layer peak, zenith angles less than about 60° (so that earth curvature can be neglected), and irregularity size D that is independent of altitude. Choose a coordinate system with x to the magnetic north, y to the magnetic east, h vertical, and the origin at the heater transmitter. Then the center of the disturbed region at 300-km height and distance x_0 to the north, has coordinates

$$[(x_0 - (h - 300) \cot \delta), 0, h]$$

where δ is the local magnetic dip. Other than x_0, the three parameters that seem to be required to specify the general form of the spatial variation of g are the value g_0 at the center of the disturbed region, and its e-folding distances X,Y in the north-south and east-west directions. Within the region where earth curvature and magnetic-field curvature may be neglected, the spatial variation of g seems to be well represented by

$$g^2 = g_0^2 \exp \{-[x - X_0 + (h - 300) \cot \delta]^2/X^2 - y^2/Y^2\} \quad . \qquad (10)$$

For typical conditions corresponding to ordinary-wave heating with maximum power, the following approximate values of the parameters apply:

$$g_0 = 0.007$$

$$x_0 = 30 \text{ km}$$

$$X = Y = 50 \text{ km}.$$

Inserting g from Eq. (10) into Eq. (9), with the approximations listed above, we obtain

$$\gamma^2 = \frac{\pi^{5/2}}{\lambda^2}\left(\frac{f_o F2}{f}\right)^4 D \sec i \operatorname{cosec} \psi \, g_0^2 \int_0^\infty \left(\frac{N}{N_m}\right)^2 \exp$$

$$\{-[x - x_0 + (h - 300)\cot \delta]^2/X^2 - y^2/Y^2\} \, dh \quad . \qquad (11)$$

In this equation, of course, the values of X and Y are parametrically determined as functions of h by the equation for the line of sight [which will be a straight line for the conditions of UHF propagation for which Eq. (9) applies].

The integral in Eq. (11) can be conveniently evaluated once we note that most of the height valuation of the integrand is contained in the term $(N/N_m)^2$, and that the exponential of the integrand is nearly constant over most of the range of interest. To a good approximation, therefore, we may write

$$\gamma^2 = \frac{\pi^{5/2}}{\lambda^2}\left(\frac{f_o F2}{f}\right)^4 D \sec i \operatorname{cosec} \psi \, g_0^2 \exp$$

$$\{-[x_m - x_0 + (h_m - 300)\cot \delta]^2/X^2 - y_m^2/Y^2\} \int_0^\infty \left(\frac{N}{N_m}\right)^2 dh \qquad (12)$$

where the integral in this equation is typically about 120 km, and x_m and y_m are the coordinates at which the line of sight intercepts the height of maximum of the layer.

If we further make the approximation that the region of disturbance is circular, we can put X = Y = R, and Eq. (12) becomes

$$\gamma^2 = \frac{\pi^5 \lambda^2}{2} \left(\frac{f_o F2}{f}\right)^4 D \sec i \operatorname{cosec} \psi \, g_0^2 \exp(-r^2/R^2) \int_0^\infty \left(\frac{N}{N_m}\right)^2 dh \qquad (13)$$

where r is the horizontal distance between a point at which the line of sight intercepts the height of maximum of the layer, and a point at the same height on the field line that passes a distance x_0 north of the heater transmitter at an altitude of 300 km.

The variation of g_0^2 with yield is well represented by a proportionality to heater power; there is some evidence that the value of g_0 at night is approximately twice that during the day, though focusing effects produce variations in x_0 that tend to make this effect less definite.

G. Relationship of FAS to ASF

The wavenumber spectrum of FAS shown in Figure 23 is produced by an rms electron density fluctuation g_o of about 0.01. Therefore, the spectrum may be replotted as a spectral density Q (k_T), proportional to P (k_T), and satisfying

$$\int_0^\infty Q(k_T)\, d\, k_T = g_o^2 \quad . \qquad (14)$$

This plot is shown in Figure 33. The fluctuations at the much larger scales in ASF have a g_o that is also about 0.01, and can be represented

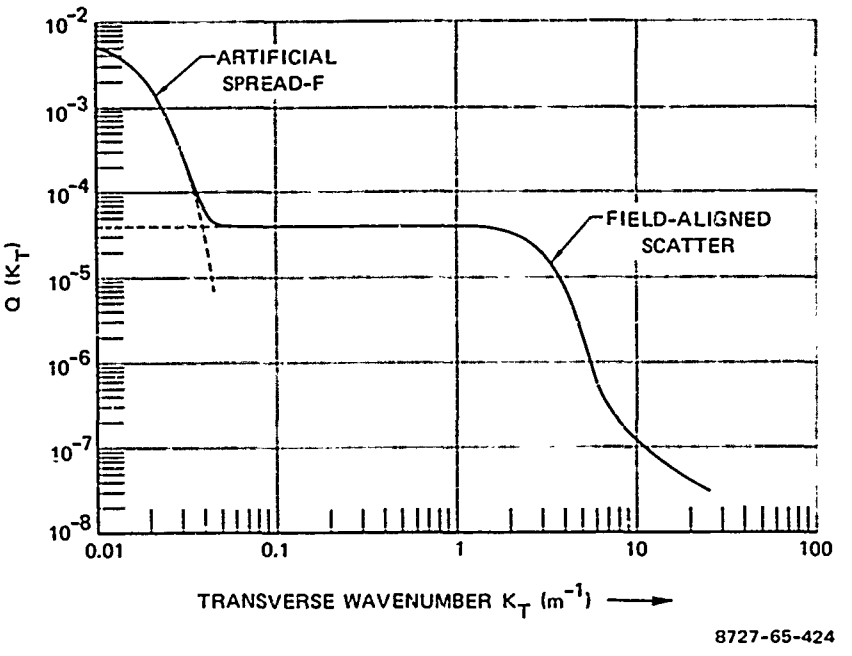

FIGURE 33 DERIVED TRANSVERSE-WAVENUMBER SPECTRUM OF DENSITY FLUCTUATIONS

also as a spectral density satisfying Eq. (14). Since the wavenumbers differ by a factor of over 100, the ASF does not contribute to FAS effects, nor does FAS contribute to scintillation effects. Nevertheless, they are both part of the same wavenumber spectrum.

H. Concluding Remarks

The scattering model presented here deals only with the so-called "on-frequency" component of scatter from the heated volume. There are other components (e.g., ion lines and plasma lines), but these are relatively weak and appear to be of secondary importance for applications. The model has been developed on the basis of information available primarily from the field experiments reported to date. In order to place the model on a firmer ground, relevant laboratory and theoretical contributions also need to be incorporated into the model. Although the model is based on the observations limited to the conditions of ordinary-mode

heating of the daytime F region, the underlying concepts apply as well to any other situation where the scattering mechanism is identified to be the same. Specifically, the model needs to be extended for the E region and the nighttime heating conditions.

V THEORY

A. General

The ionosphere is one of the few regions where man can apply enough power to substantially modify the energy content of the environment on a large scale. The plasma of the ionosphere is sufficiently dilute to have small heat capacity, yet is sufficiently close so that man-made energy fluxes are not overly weakened by the inverse-square falloff with distance. An estimate of the power required to raise the ionospheric electron temperature by a factor of 2 is straightforward: the electron heat content, U, of $(100\ \text{km})^3$ of ionospheric plasma with $n = 4 \times 10^5\ \text{cm}^{-3}$ and $T_e = 1000°\text{K}$ is $U \approx 10$ MW s, while the electron-ion energy equipartition time is $t_{eq} \approx 50$ s. Hence, transmitters of megawatt power levels focused onto areas of $(100\ \text{km})^2$ at ionospheric heights can substantially alter the electron temperature if all the incident power is absorbed. Furthermore, incident power fluxes that are intense enough to modify the energy balance through ohmic heating can also cause parametric instabilities that produce additional nonlinear absorption.[13] For orientation, one should note that an incident energy flux of $1\ \text{MW}/10^4\ \text{km}^2 = 10^{-1}\ \text{ergs/cm}^2\text{-s}$ substantially exceeds the energy fluxes of $(3\text{-}10) \times 10^3\ \text{ergs/cm}^2\text{-s}$ due to photoelectrons and heat conduction in typical daytime ionospheres.

A useful overview of ionospheric heating can be gained by examining the distribution of energy losses due to various dissipative processes and the concomitant ionospheric changes that are produced by these mechanisms (Figure 34). In the F layer, ohmic heating, due to deviative absorption, and nonlinear heating by various mechanisms, principally the parametric decay instability, account for the absorption of as much as

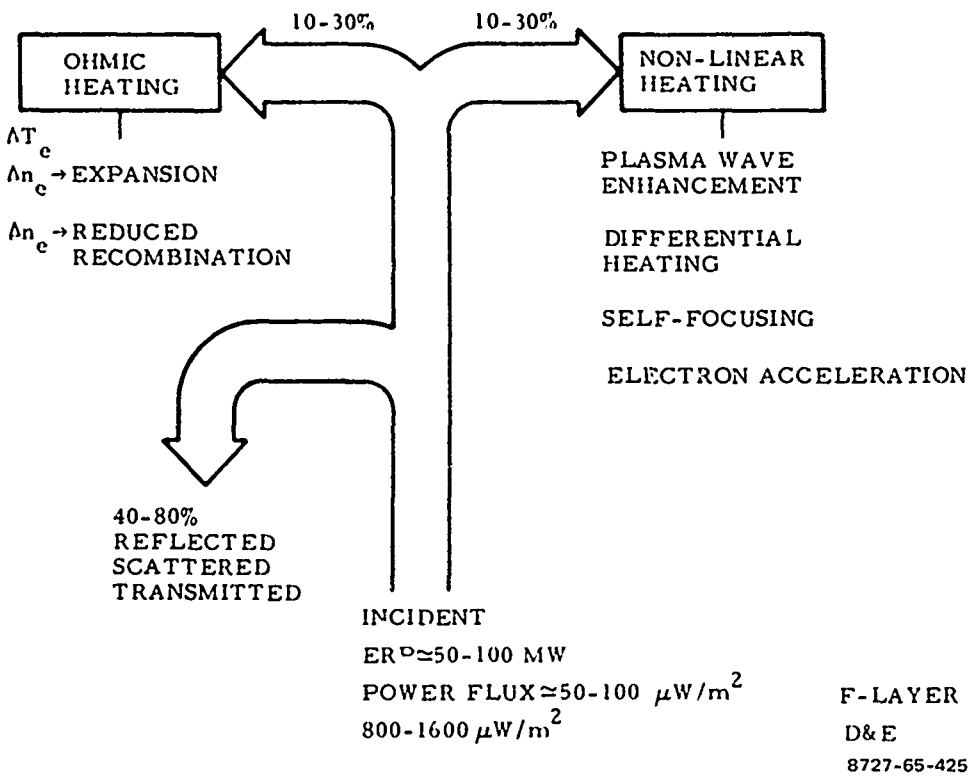

FIGURE 34 DISTRIBUTION OF LOSSES AND THE ASSOCIATED IONOSPHERIC CHANGES PRODUCED BY RADIOWAVE HEATING

60% of the incident power. The generation of large plasma-wave intensities contributes about 10 to 30% of the absorption,[13, 21, 22] while another 10 to 30% of the incident HF energy is absorbed through ohmic or joule heating. Only a small fraction of the energy, perhaps of the order of 10%, goes into fast electrons. If the ionosphere is illuminated with sufficiently low frequencies, then D-region heating and deviative E-region absorption dissipate almost all of the incident energy.

The heating and expansion of the F-layer plasma occurs in several phases. During the first minute, energy is imparted to the electrons through ohmic dissipation and by plasma-wave collisional and Landau damping, causing an increase in the electron temperature; pressure gradients develop as a result, and the plasma expands along the magnetic field. As the heating continues, the F-region density is reduced and the electron

and ion temperatures increase and approach steady state in about two minutes. The density changes probably cause self-focusing, which produces large-scale structuring of the ionosphere and the overall density depletion that is evident in the multiple-echo ionograms, airglow maps, and radar-backscattering maps at UHF.[23] A more subtle effect is the differential heating produced by stimulated Brillouin,[24] stimulated diffusion scattering, or self-focusing instabilities.[25] These effects are probably the cause of the large-scale field-aligned irregularities that are manifest in the development of spread-F and the ducted modes[3] that are inferred from HF phased-array maps.[26]

Ohmic heating in the D layer, in contrast to F-layer heating, produces an increase in the electron density due to a decrease in the rate of dissociative recombination. There are no direct measurements of this effect as yet but absorption measurements following sustained heating suggest that a density increase has occurred.

B. Theoretical Models and Observations

Ionospheric modification experiments show that the plasma structure generated by heating spans a wide range of perpendicular lengths and a number of geometries. A correspondingly wide variety of theoretical models are anticipated in order to provide qualitative, and hopefully quantitative, understanding of all the underlying physical processes.

In the discussion that follows, we include not only a direct comparison of predictions with observations of plasma turbulence, but also theoretical arguments that small-scale structure should, via instabilities, spontaneously arise from the measured large-scale properties of the ionospheric modification experiments (e.g., incident-power flux and plasma-density scale lengths).

1. Small Scales (1 to 50 Meters)

The most striking observation of the entire program--strong scattering by short-wavelength, field-aligned density fluctuations--requires a model that explains why the density fluctuations are so intense and why they are field-aligned. The origin of these nonpropagating field-aligned structures as well as the mechanism that generates plasma waves propagating orthogonal to the magnetic field is discussed in Section V-D.

Short-wavelength structure, in the form of plasma waves and ion-acoustic waves propagating along (or close to) the magnetic field,[27] which are predicated by theory, is needed to explain the Arecibo plasma-line incoherent-scatter spectra and the SRI ion-acoustic scatter observations. These waves are also the most plausible source of the accelerated electrons that cause the observed airglow enhancements. Section V-D begins a discussion of theoretical models dealing with these questions.

2. Intermediate and Large-Scale Structures

Fluctuations in the lower range of this regime have scale sizes comparable to the modifier wavelength and are probably responsible for the wideband-attenuation effect observed on ionograms. A qualitative model for these structures is discussed in Section V-D.

Longer-wavelength structures produce artificial spread-F as observed on ionograms, and scintillations of UHF and VHF signals from satellites and radio stars.

3. Global Effects (10 to 100 km)

The general overall heating and distortion of the ionosphere is taken up in Section V-G.

C. Parametric Instabilities and Plasma Waves Propagating Along the Magnetic Field

Soon after the results of the initial ionospheric modification experiments became available, it was predicted[27] that the modifier electric field was sufficiently intense to set off parametric instabilities whereby the energy of the incident electromagnetic wave would spontaneously convert into a short-wavelength electron-plasma, ion-acoustic wave pair. These waves would give a part of their energy up to the high-energy portion of the ambient electrons, creating the accelerated electrons required to produce the airglow. The observations of enhanced scattering with a frequency shift equal to the predicted plasma-wave frequency (slightly less than the modifier frequency) of the Arecibo Ionospheric Observatory provided an important stimulus for a major effort to compute the saturation level of the parametric instability, the concomitant nonlinear absorption, and the scattering cross sections. Several publications[13,21,23] document this effort. The principal conclusions are:

(1) Both the spectrum and intensity of the scattering observed at Arecibo can be quantitatively explained (see Figure 35).

(2) Nonlinear absorption of roughly 10 to 30% is expected for the Boulder experiment.

(3) The most intense density fluctuations are associated with plasma waves propagating in the direction of the modifier electric field (Figure 36), which for an ordinary-mode modifier, lies close to geomagnetic-field direction. The intensity was predicted to be roughly four orders of magnitude higher than the scattering observed at Arecibo and four orders of magnitude weaker than field-aligned scatter.

(4) Ion-acoustic waves should be excited.

(5) Sufficient heating of the high-energy electrons was available to account for airglow observations.

Items (1), (2), and (5) all agree with various experimental measurements. But a crucial test of the theory is the direct observations of

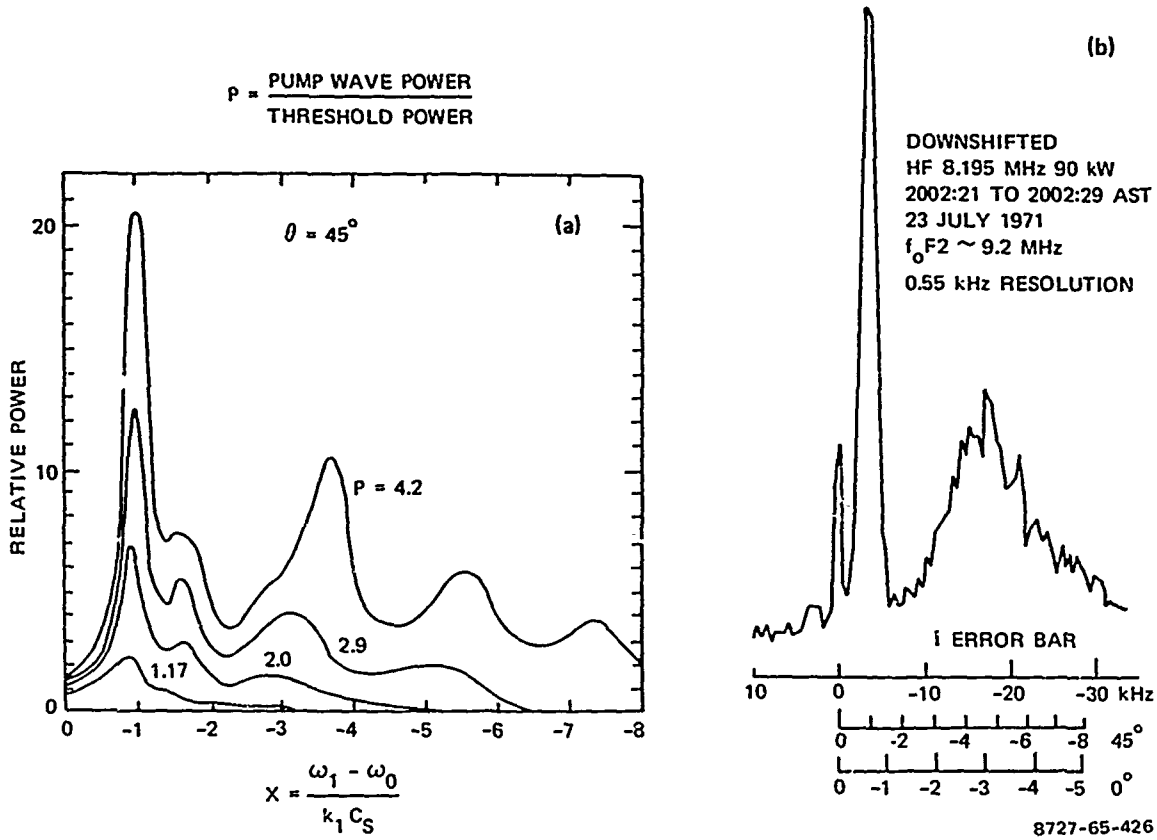

FIGURE 35 ILLUSTRATION OF AGREEMENT BETWEEN PREDICTED AND MEASURED SHAPE OF THE SPECTRUM OBSERVED AT ARECIBO

intense plasma waves propagating along the magnetic field, an experiment that has failed to detect positive results in two cases. Although these experiments were five orders of magnitude less sensitive than Arecibo, and although the predicted signal-to-noise ratio was roughly 3, it should have been sufficient to allow detection with pulse-to-pulse integration.

Therefore, until sufficiently sensitive scattering experiments are fielded to obtain positive results and/or the theory is revised (if so required) to provide alternative explanations of (1), (2), (4), and (5), the agreement between theory and experiment will remain inconsistent.

The inconsistent picture outlined above gives rise to uncertainties in our models of field-aligned scatter and the overall nonlinear energy

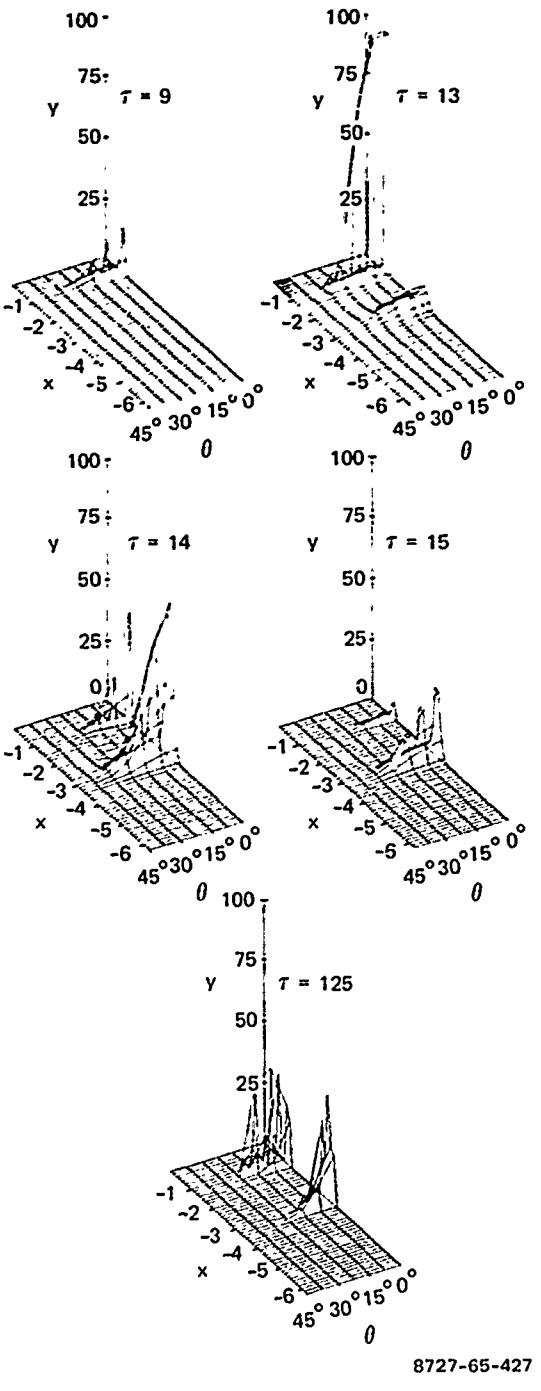

FIGURE 36 NONLINEAR SPECTRUM OF PLASMA WAVES RESULTING FROM PARAMETRIC INSTABILITIES. Here τ is proportional to time from the application of the pump field. Note that the waves observed at Arecibo ($\theta = 45°$) are invisible compared to the nonlinear intensities.

absorption. Furthermore, it is difficult to understand why parametric instabilities are not unstable, given the incident power fluxes.

D. Field-Aligned Density Fluctuations

The appearance of very intense small-scale field-aligned density fluctuations was surprising. The existing theory of parametric instabilities outlined in the previous sections implied that: (1) the low-frequency density fluctuations would be small compared to density fluctuations in the plasma waves (resulting in plasma-line scattering exceeding central-line scattering), and (2) the most intense fluctuations should be along (not across!) the magnetic field. Recently a new concept in parametric instability theory[29,30] was discovered that appears to explain many of the features of the field-aligned fluctuation. Because it is quite recent, the concept has not yet been fully developed to the necessary extent, whereby the precise manner in which the field-aligned irregularities arise can be determined.

The new concept[29,30] is that the nonlinear interaction between two high-frequency waves to produce a low-frequency heat wave can occur through differential heating as well as by a ponderomotive force. Simple requirements show that heating dominates when the low-frequency wavelength across the magnetic field is longer than an electron gyroradius (2 cm), and the wavelength along the field is longer than the mean free path (0.2 km), a geometry satisfied by the observations. Under these conditions, the low-frequency density fluctuations can become larger than those associated with the plasma waves.

These arguments indicate that the new interaction, which is due to differential heating, accounts for the magnitude and geometry of field-aligned density fluctuations, but exactly how it operates is not clear. Two possibilities arise: first, if the plasma-wave turbulence predicted

in the preceding section exists, it can provide the high-frequency pump waves; preliminary analyses of this mechanism show agreement with the observed results, but the required plasma-wave turbulence has not been found by direct experiments (only inferred by indirect ones). The second mechanism is a direct decay from the electromagnetic wave into short-scale-length field-aligned waves. This is a very-low-threshold process in a uniform plasma, but difficulties occur in the ionospheric case because the frequency sum rule, which requires that the pump frequency be equal to the plasma-wave frequency, cannot be satisfied except at one point along the magnetic field line. A calculation (not yet performed) to determine whether the nonlinear interaction is sufficiently robust to overcome the frequency mismatches remains to be done. And even if the answer were positive, only a saturation calculation could provide an estimate of the scattering cross sections.

On the other hand, both processes will produce short-wavelength plasma waves propagating across the magnetic field because of the beat between the short-wavelength density fluctuations and the small (but definitely nonzero) perpendicular components of the pump electric field. The frequency spectrum of these plasma waves should reflect the frequency of the field-aligned fluctuations, which indeed they do.

E. Wideband Attenuation and Artificial Spread F

The interaction of high-frequency waves via differential heating has also emerged as the most likely explanation of wideband attenuation and artificial spread-F. Indeed, the heating interaction was discovered in independent attempts to explain field-aligned scatter[29] and artificial spread-F.[30] The difference between the field-aligned scatter process and artificial spread-F lies in the high-frequency waves involved, field-aligned scatter being a short-wavelength phenomenon involving electrostatic plasma waves, whereas in artificial spread-F the high-frequency

waves are electromagnetic. The only difference between artificial spread-F and wideband attenuation lies in the scattering angle that the electromagnetic waves undergo; large scattering angles produce the observed wideband attenuation (which we take to be not a true absorption, but a scattering process), while small scattering angles yield artificial spread-F. Because small scattering angles go over into refraction in the geometrical optics limit, artificial spread-F is often attributed to self-focusing. Several publications[30],[31] document this research, and there is general, but not complete, agreement with the experiment.

F. Conclusions About the Generation of Scattering Structure

As to firm conclusions of practical interest, we can say the following:

- Strong scattering will remain field-aligned down to an altitude where the electron-neutral, mean free path becomes comparable to the wavelength of the scattering wave.
- Plasma-line scatter will not exceed the currently predicted (but not observed) levels because the present incident energy fluxes cannot provide enough energy to maintain a higher level.
- Artificial spread-F has a low threshold ($\sim$10 μ-watts/m^2).

G. Plasma Heating

A theoretical model of the initial stages of heating, when the density changes are small and the temperatures are approaching or have reached steady-state, comes from a solution of the one-dimensional conservation equations.[32] Changes in the electron and ion temperature are governed by the energy balance in the electron and ion gases; density changes are determined by a simultaneous solution of the continuity and momentum equations. It is sufficient to treat the electron heating alone, since

the ion heating is generally small and can be neglected (the ion temperature remains essentially unchanged due to the high ion-neutral collision frequency of $\sim 1\ s^{-1}$ and the much greater concentration of neutrals that act as a heat sink). The relationship between the rate of change of plasma energy and the RF heating is given by:

$$\frac{d\bar{E}}{dt} + P_e \frac{d}{dt}\left(\frac{1}{\rho_e}\right) = \frac{1}{\rho_e}\left\{Q - L_e + \frac{\partial}{\partial x} K_e \frac{\partial}{\partial x} \delta T_e\right\}$$

where

$\bar{E} = 3/2\ k\ T_e/M_e$ = Specific electron energy

$P_e = N_e\ k\ T_e$ = Electron pressure

$\rho_e = M_e N_e$ = Mass density

$\delta T_e = T_e - T_{eo}$ = Change in electron temperature

x = Magnetic field-aligned coordinate.

The dissipation per-unit-volume, Q, includes both linear ohmic losses due to deviative and nondeviative absorption, and anomalous losses due to the damping of plasma waves by electron collisions with ions and neutrals. Collisional losses, donated by L_e, include elastic collisions with ions and neutrals, and inelastic energy transfer through the excitation of fine-structure transitions in O (^3P) and the rotational and vibrational levels of N_2. Energy is also transported away from the heated region by the thermal conduction in the electron gas. The thermal conductivity K_e is small in the D and E layers, and is by comparison substantial in the F region where electron temperature is large and the electron-neutral collisions are infrequent.

We compute the dissipation by first determining the local electric field from a combination of raytracing and full-wave theory and then substituting in the fundamental relations

$$Q = 1/2\ J \cdot E = 1/2\ \sigma E^2 = \sigma S \cdot \eta \quad .$$

Here, we have expressed the loss in terms of the Poynting flux S and a local wave impedance η. The conductivity σ is composed of a linear ohmic part and a nonlinear part[13] that is proportional to E^2.

Predicted changes in electron temperature and the concomitant density reductions are displayed in Figures 37(a) through (d) in the form of contour maps of constant fractional change in the magnetic meridian plane. The parameters correspond to representative nighttime conditions and typical effective radiated powers (ERP) at Arecibo and Platteville. Density decreases of about 3% (after two minutes of heating) are noted along with an expected northward displacement in the location of the maximum temperature increase. Density changes as large as 14% after 10 minutes of heating have been reported,[33] while electron-density reductions of about 7% are inferred from ionograms recorded near Platteville.[3] One other noteworthy point is the difference in the altitude extent of ΔT_e in the two cases [Figures 37(a) and 37(c)]. This is due to the difference in electron thermal conduction since $K_e \propto T_e^{5/2}$.

A comparison of the predicted changes in the electron temperature and the measured increases (obtained by incoherent-backscatter techniques at Arecibo) can be drawn by comparing Figures 37(a) and 38. The time constants for heating and cooling are also in fair agreement (Figure 39) with theoretical predictions. Note the apparent oscillation in T_e after 30 s of heating. This could be due to the effects of self-focusing and electron-density reductions. Figure 40 illustrates the expected nonlinear dependence of the density decrease and temperature increase with transmitter power. The results shown in this figure are for nighttime heating with a frequency 5% below the peak plasma frequency in the F layer.

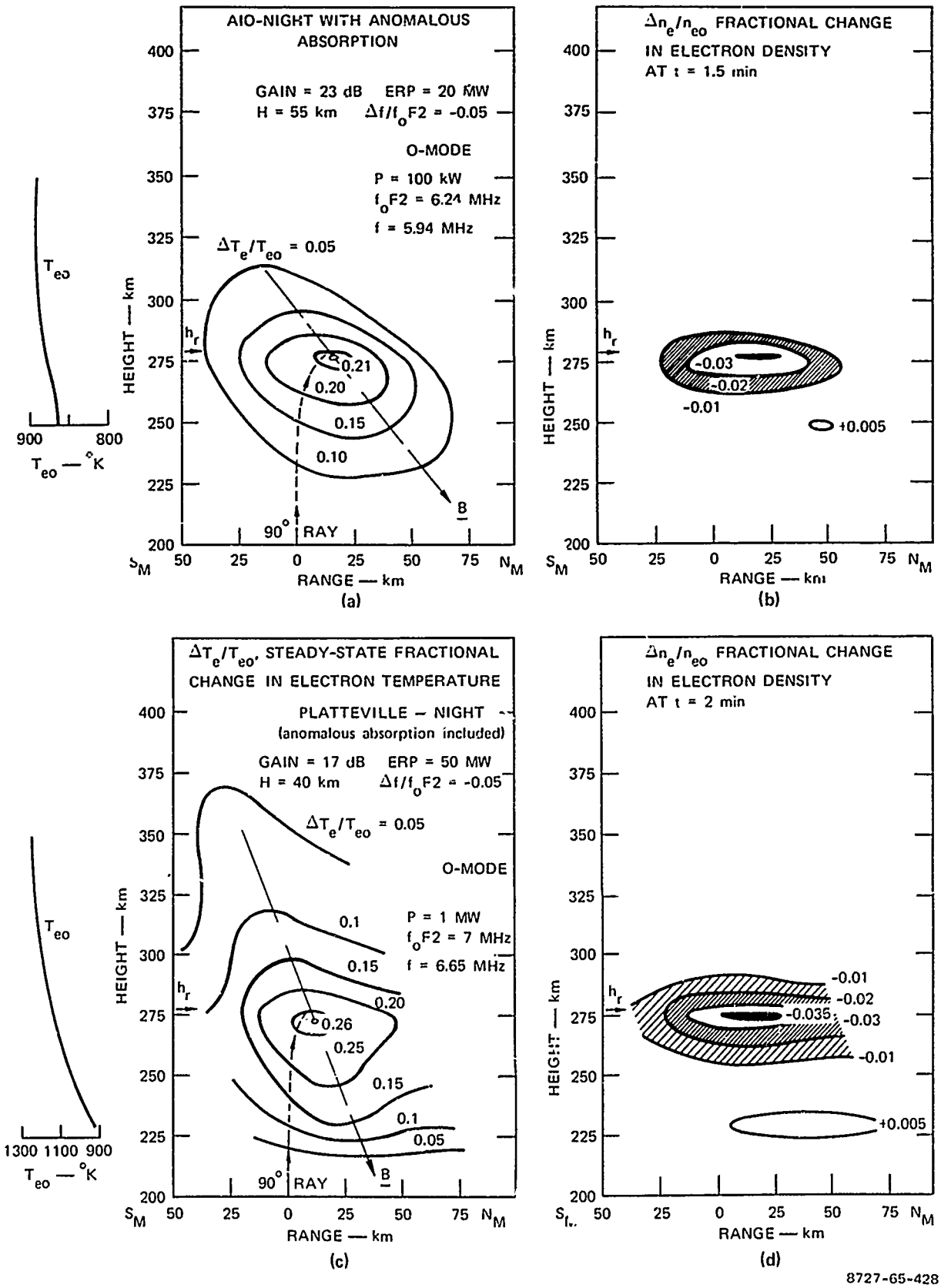

FIGURE 37 COMPUTED FRACTIONAL CHANGE IN THE ELECTRON TEMPERATURE AND DENSITY IN THE PLANE OF THE MAGNETIC MERIDIAN

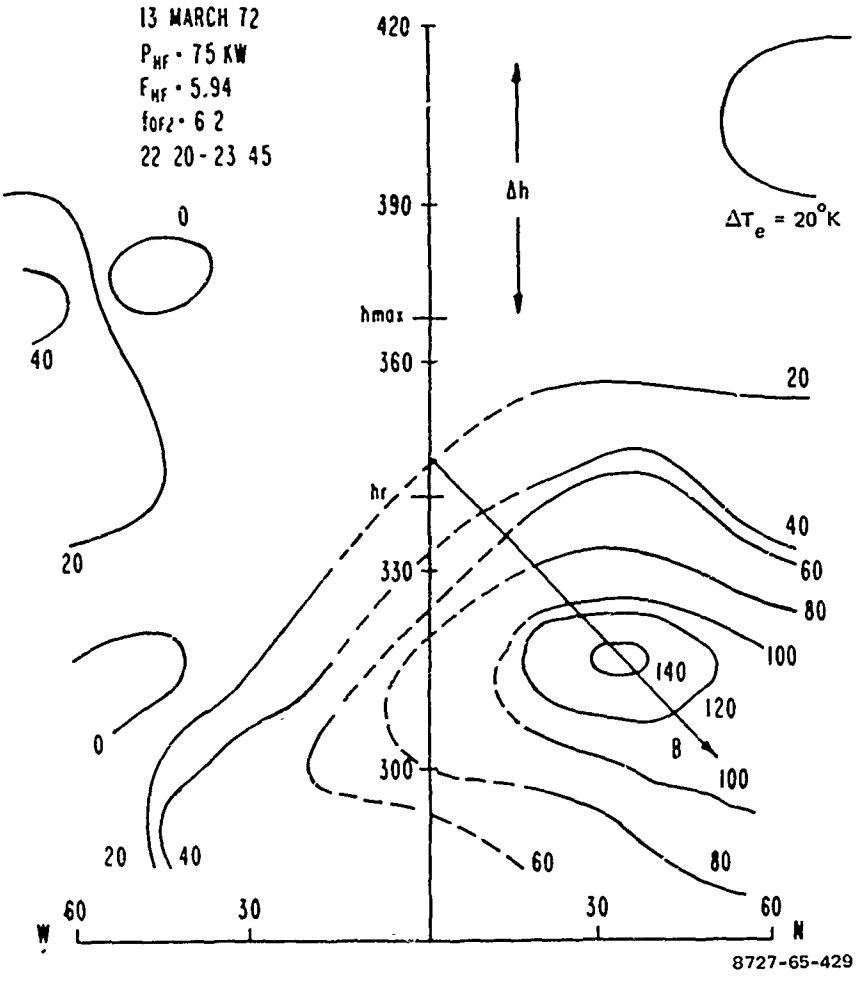

FIGURE 38 OBSERVED ELECTRON TEMPERATURE CHANGES DUE TO CW IONOSPHERIC HEATING AT ARECIBO

Calculations of temperature and density changes due to remote heating with obliquely incident waves have also been carried out.[34] The results shown in Figure 41(a) and (b) show small changes compared to the overhead heating results previously discussed.

A more accurate estimate of temperature and density changes requires a self-focusing computation wherein one self-consistently computes the energy deposition as the density is changed. A limited study of large-scale self-focusing shows that if the heating frequency is about 1% below

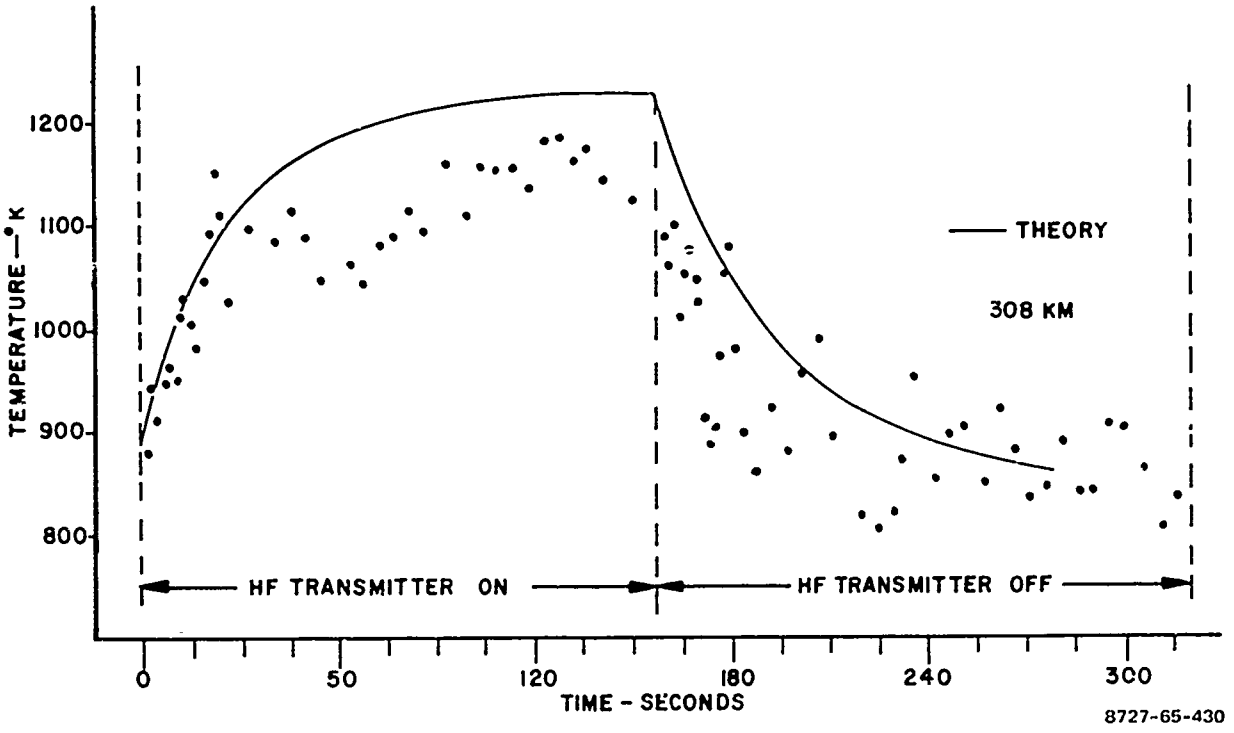

FIGURE 39 COMPARISON OF THE COMPUTED HEATING AND COOLING TIMES AND THOMSON-SCATTER MEASUREMENTS

$f_o F2$, then burnthrough can be achieved in a few minutes as shown in Figure 42. In this example, the energy disposition was recomputed at the end of 60 s of heating and the subsequent evolution of density contours was charted without further iterations. One can see the bulge that develops due to the plasma expansion, ultimately breaking through the peak of the F layer and allowing the previously reflected rays to penetrate. In effect, a "hole" has been punctured in the F layer. The time constant for this phenomenon and the dependence of the displacement in the constant density contour at reflection Δh on transmitted power are shown in Figures 43(a) and (b).

Nonlinear absorption will also occur in the lower ionosphere when the region is illuminated by intense radio waves. In fact, calculations of ohmic heating, based on generally accepted formulas for inelastic electron energy loss rates in the lower ionosphere, predict unexpectedly

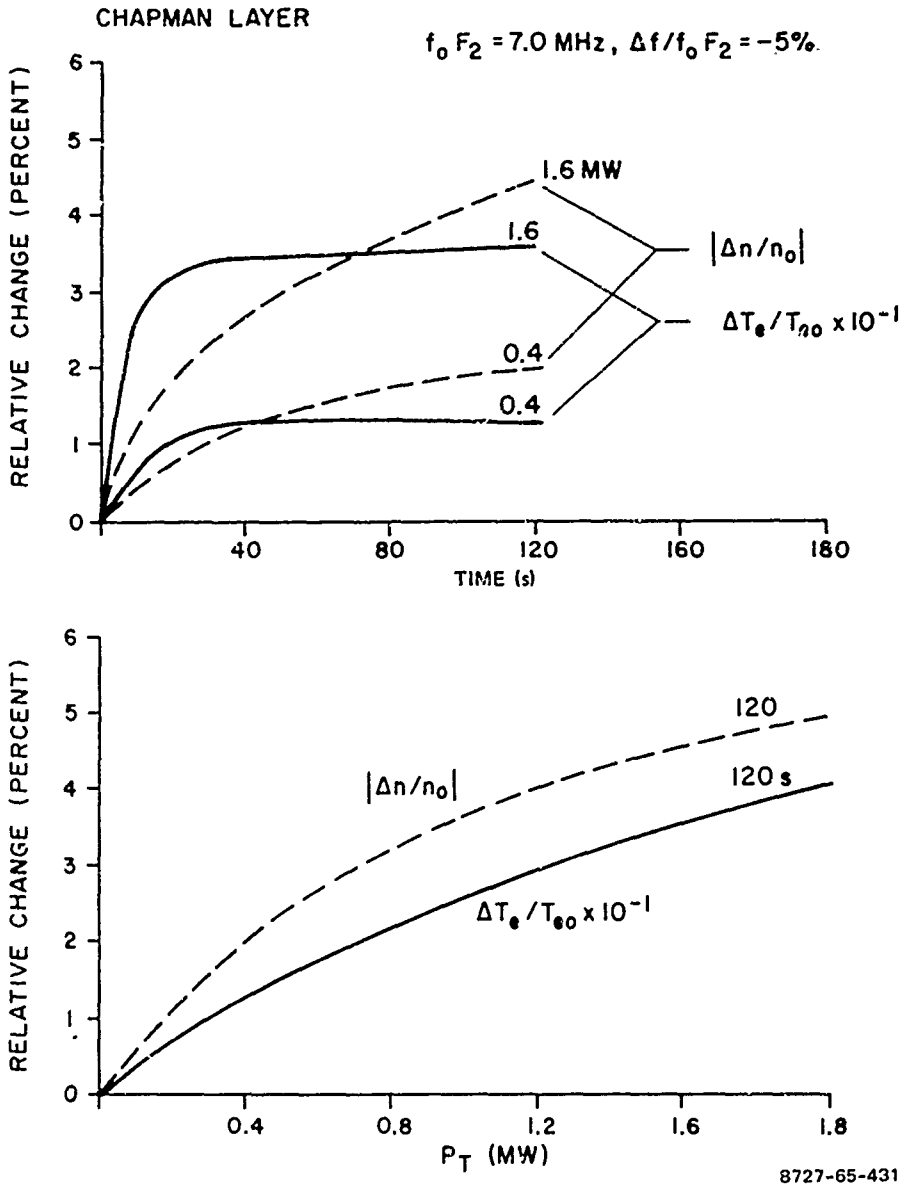

FIGURE 40 COMPUTED ELECTRON-TEMPERATURE INCREASES AND DENSITY REDUCTIONS AS A FUNCTION OF TIME AFTER TURN-ON AND TRANSMITTER POWER

large increases in electron temp rature and corresponding changes in absorption when the D and E regions are irradiated by radio waves having frequencies and power densities comparable to those attainable with the Platteville facility.[35] For power densities greater than a critical value, the electron temperature increases rapidly after the HF power is turned

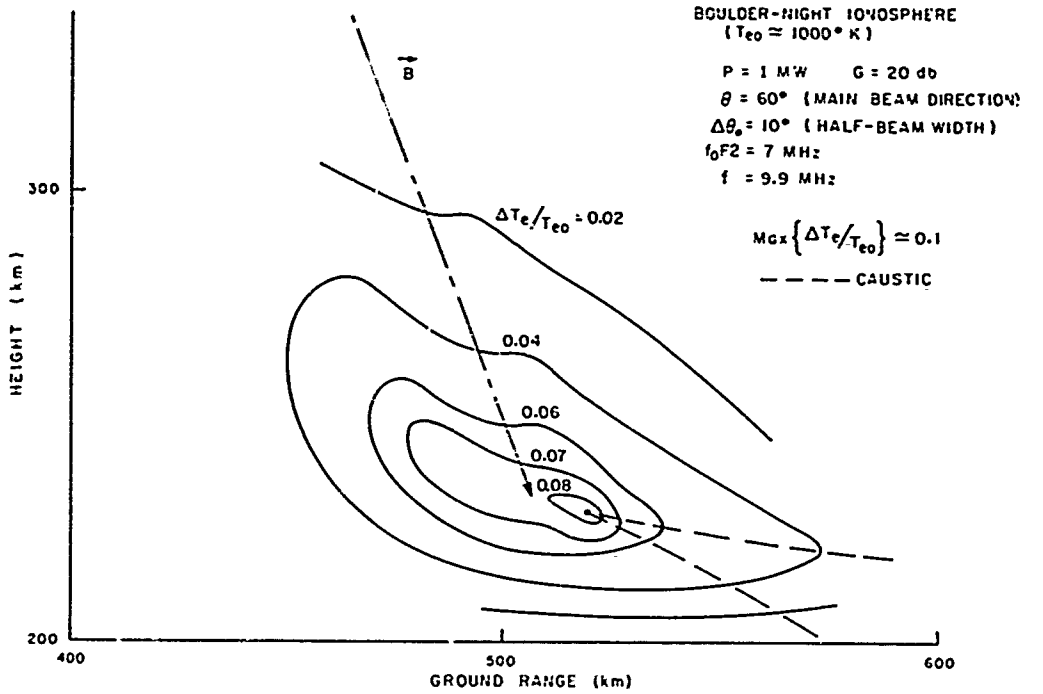

(a)

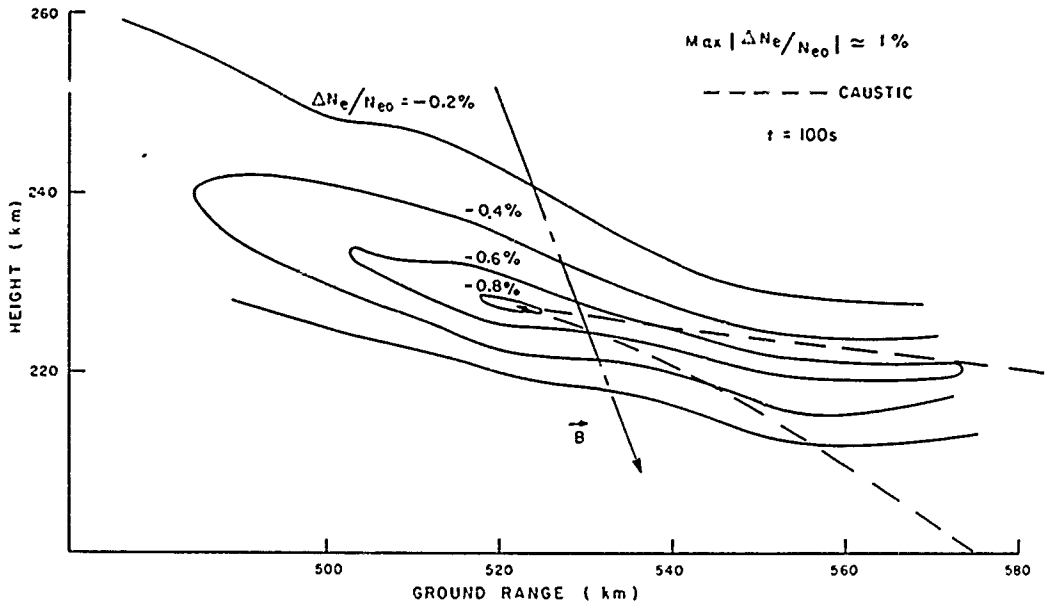

(b)

8727-65-432

FIGURE 41 FRACTIONAL CHANGE IN IONIZATION DENSITY FOR OBLIQUE HEATING AT t = 100 s

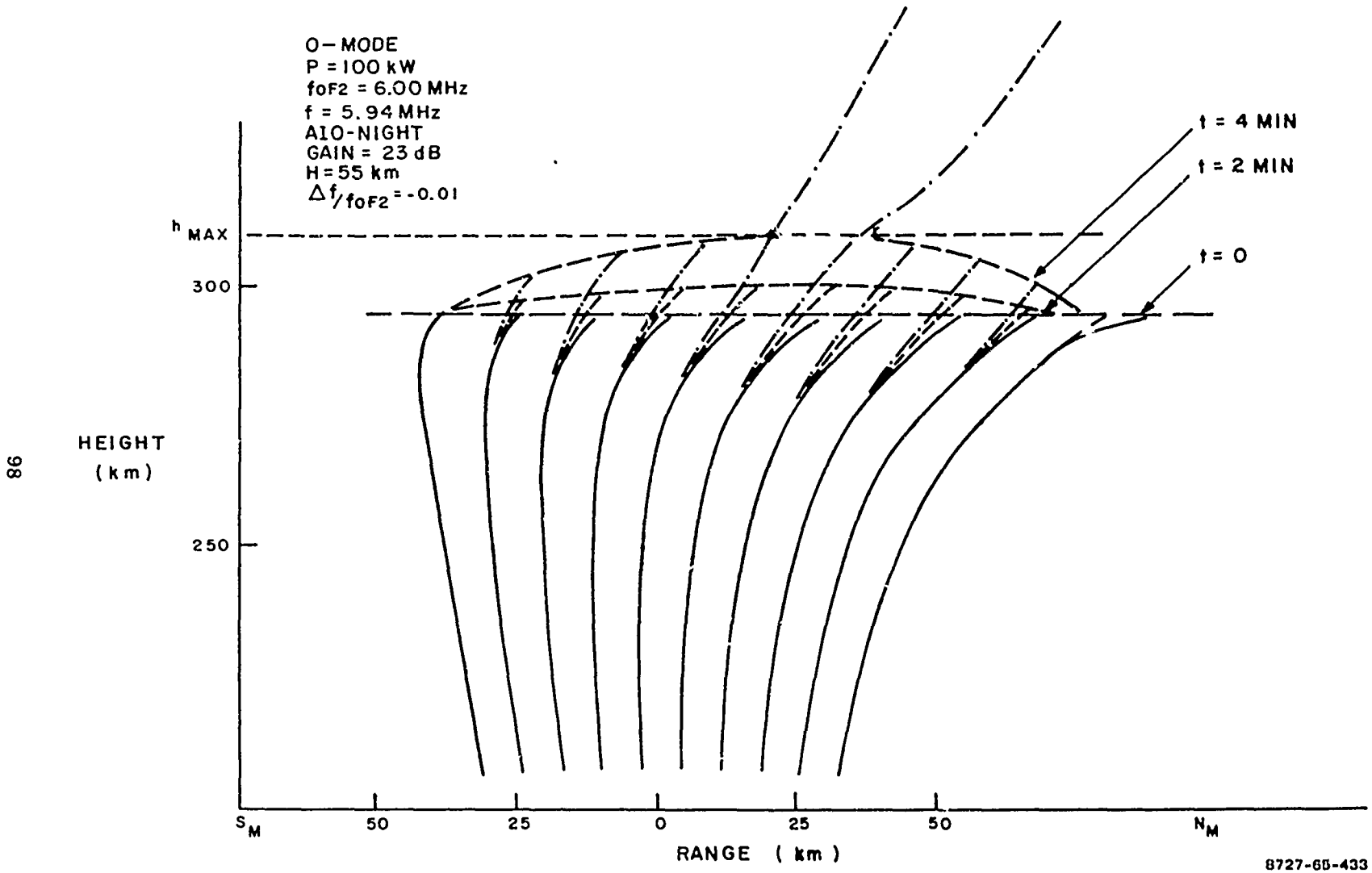

FIGURE 42 FORMATION OF AN IONOSPHERIC BULGE AND SUBSEQUENT "BURNTHROUGH" DUE TO SELF-FOCUSSING

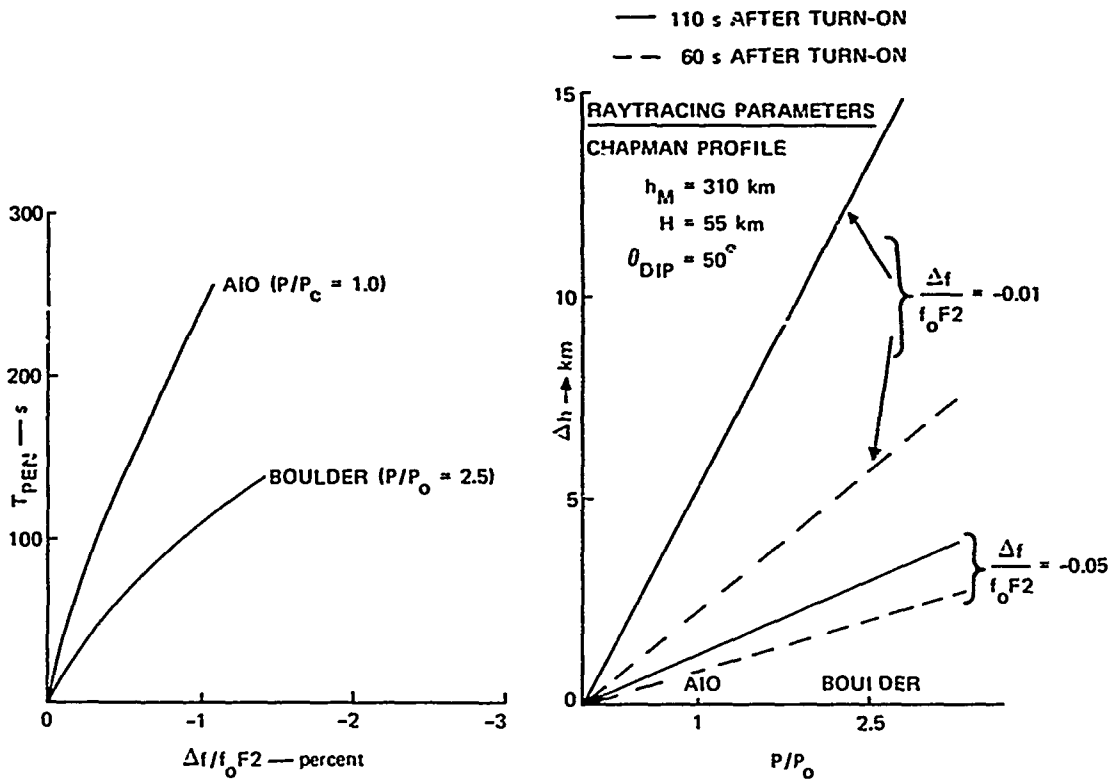

(a) PENETRATION TIME vs. $\Delta f/f_oF2$ FOR TWO POWERS

(b) PENETRATION DEPTH vs. INCIDENT POWER

8727-65-434

FIGURE 43 . CHANGES IN CONSTANT-DENSITY CONTOURS NEAR REFLECTION HEIGHT

on and rises to a steady-state value of the order of 10 times ambient. The electron density is also expected to increase, but on a longer time scale, due to a decrease in the recombination rate. Since both the density and the collision frequency increase once the nonlinear effect is triggered, one expects an increase in the D-region absorption during sustained high-power illumination.

Since electron thermal conductivity and fluid motion can be neglected in the lower ionosphere, the electron temperature satisfies

$$\frac{\partial T}{\partial t} = 1.12 \times 10^{-6} \nu_{en} S f_e^{-2} - (2/3) \sum_i U_i \qquad (15)$$

where S is the power density in $\mu W/m^2$, f_e is the effective frequency in MHz ($f_e^2 = (f \pm f_B)^2 + \nu_{en}^2/4\pi^2$), T is the electron temperature in eV, and U_i is the rate of energy loss per electron due to the ith loss process. (The choice of sign in the definition of the effective frequency depends on the mode, "plus" corresponds to the O-wave and "minus" to the X-wave; f_B is the electron gyrofrequency.) Here ν_{en} is an effective Appleton-Hartree collision frequency which, for $f \gg \nu_{en}$, equals 5/3 times the unaveraged collision frequency evaluated at the mean electron energy (i.e., 5/2 times the collision frequency evaluated at an energy corresponding to the mean thermal speed). With this correction, the collision frequency will be taken as

$$\nu_{en} = 2.88 \times 10^{-7} \, T \, n_2 \quad . \tag{16}$$

Under ambient conditions, electron energy is mainly lost to rotational excitation of nitrogen and fine-structure transitions in O. The measured losses may be approximated by

$$U_1 = 2.93 \times 10^{-12} \, n_2 \, T^{-1/2} \, \delta T \tag{17}$$

for the rotational losses to N_2 and O_2, and

$$U_2 = 4 \times 10^{-12} \, n_1 \, T_N^{-1} \, \delta T \tag{18}$$

for the O (^3P_J) $\rightarrow$ O ($^3P_J1$) transition, where temperature and energy are in eV, T_N is the ambient neutral temperature, n_1 is the number density of O, and $\delta T = T - T_N$.

The steady-state solution for the electron temperature can be obtained if a temperature can be found for which the right-hand side of Eq. (15) is zero. The results at 95 km for a model atmosphere with

$n_1 = 3.41 \times 10^{11}$ cm^{-3}, $n_2 = 2.45 \times 10^{13}$ cm^{-3}, and $T_N = 198^\circ$, are shown in Figure 44. The dashed straight line shows the steady-state electron

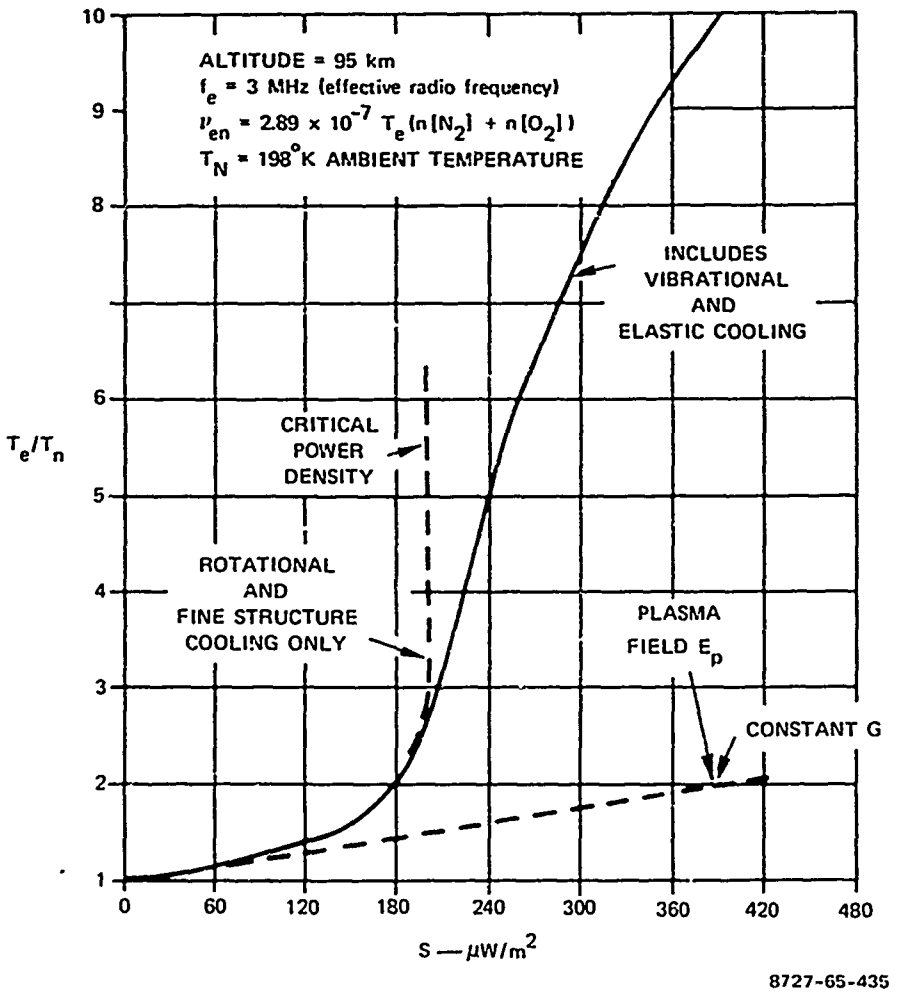

FIGURE 44 STEADY-STATE ELECTRON TEMPERATURES AS A FUNCTION OF POWER DENSITY FOR 3-MHz EFFECTIVE FREQUENCY

temperature that would be obtained if G, the fractional energy loss from collision, had a constant value of 4.03×10^{-3}, the ambient value calculated from Eqs. (17) and (18). This number is in good agreement with the value of 5×10^{-3} used for G by Showen.[26] If we substitute U_1 and U_2 from Eqs. (17) and (18) into Eq. (15), we obtain the dashed curve in Figure 44; if only these two cooling losses are considered, no solution exists for S greater than a critical power that we denote by S_c. For power densities

greater than S_c, the temperature excursion will be limited only after some new limiting loss process intervenes. The solid line in Figure 44 was calculated by assuming that the process is vibrational loss to N_2, which we have modeled on the basis of Dalgarno's[37] tabulated rates by the expression

$$U_3 = 1.95 \times 10^{-9} n_2 \left(T^4 - T_N^4\right) \quad . \tag{19}$$

In addition, the elastic energy loss, which was less important, was taken as

$$U_4 = 5.85 \times 10^{-5} \nu_{en} \delta T \quad . \tag{20}$$

These new loss processes control the electron temperature after it has undergone a large increase. The loss expressions may be modified if enough CO_2 is present or if the internal states of neutral molecules in the ambient atmosphere have a nonequilibrium distribution. Although there is some uncertainty in the collision frequencies and the loss rates, this uncertainty is unlikely to affect the existence of S_c although it may affect its numerical magnitude. At 95 km the loss rate for power densities less than S_c is dominated by rotational losses. At 115 km where fine-structure transition to O dominates, because of the increase in atomic oxygen relative to N_2, the critical power density is larger while the fractional increase in electron temperature is lower.

Figure 45 shows the rate of change of electron temperature calculated from Eq. (15) at 95 km for the specified power levels. In this figure, a power density of 270 $\mu W/m^2$ is greater than the critical power density although it is below S_c at 115 km.

A cross-modulation experiment was carried out under the direction of Dr. W. F. Utlaut during February, 1973.[38] The results are shown in

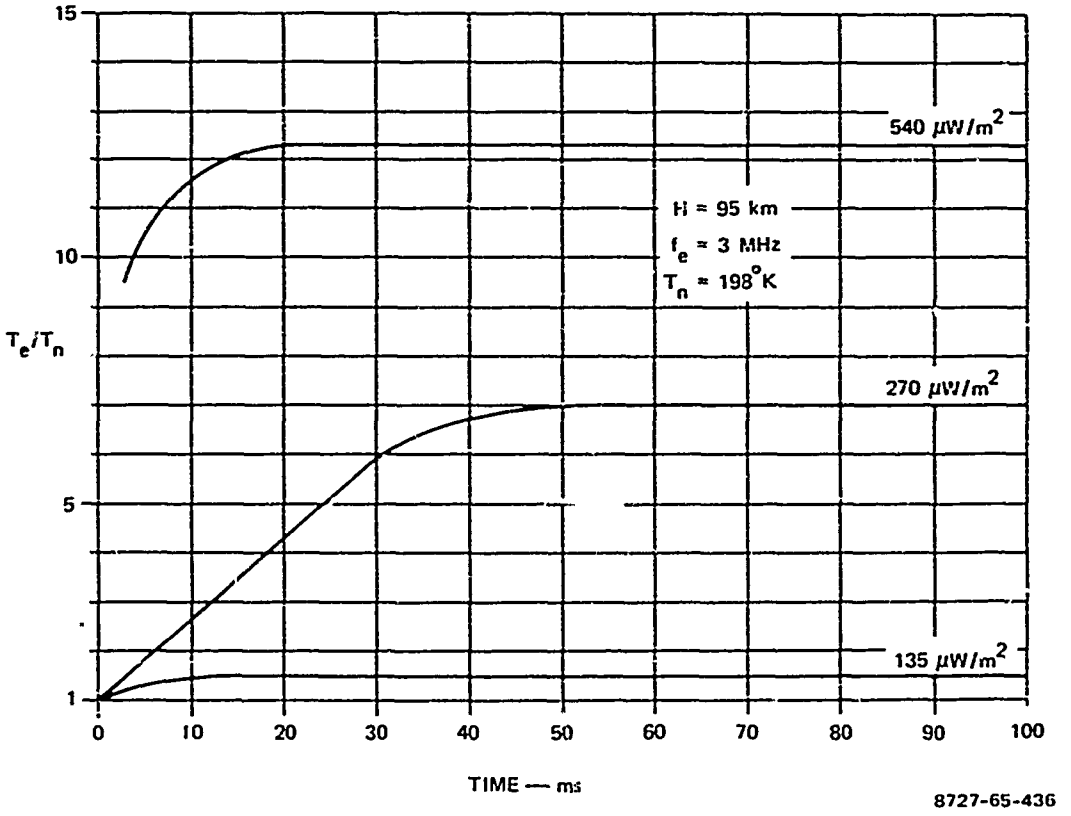

FIGURE 45 ELECTRON TEMPERATURE AS A FUNCTION OF TIME AFTER THE RF POWER IS TURNED ON, FOR THREE DIFFERENT POWER DENSITIES

Figure 46. We can use our preceding results to estimate the expected critical power density for the onset of large increases in absorption and hence cross-modulation in this experiment. Scaling the value of S_c given in Figure 44 to an effective frequency of 6 MHz, which corresponds to 7.4-MHz X-mode operation, we find $S_c \sim 760\ \mu W/m^2$. The incident power flux at 77.5 km is 1895 $\mu W/m^2$ for P = 1.8 MW and G = 92 (computed lossless gain at 7.5 MHz), including 0.6 dB ascribable to nonlinear absorption below 77.5 km. Thus, assuming that 50% of "full power" corresponds to these conditions, we have plotted the computed value of S_c on Figure 44. One or two dB less power density would bring the value of S_c in near coincidence with the observed break in the amplitude of the X-wave experiment. The O-mode critical power density at 7.4 MHz is twice as large

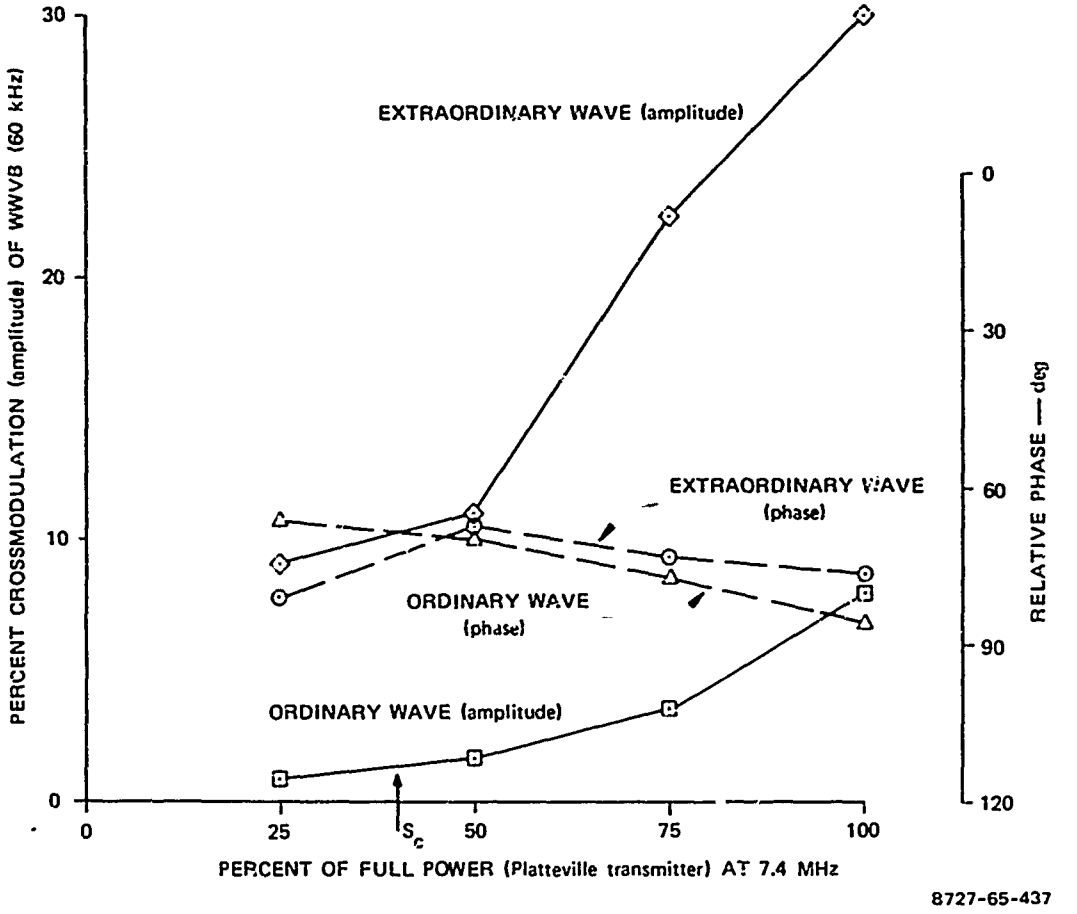

FIGURE 46 MEASUREMENTS OF THE PHASE AND AMPLITUDE OF WWVB (60-kHz) TEST PULSES REFLECTED FROM THE D REGION ABOVE PLATTEVILLE

as the X-mode value and we do note a distinct deviation in the O-mode amplitude from a linear dependence on power at values of S in excess of the S_c for the O-mode.

Self-consistent computations of nonlinear absorption and electron temperature and density changes have been carried out for a model midday ionosphere. The predicted electron temperature is shown in Figure 47 for various effective frequencies. This plot shows that the strong nonlinear effects occur below 90 km and that they are not necessarily monotonically decreasing with effective frequency. These computations are for an ERP of 90 MW; results for a larger ERP can be obtained by noting that $S_c \propto f_e^{-2}$.

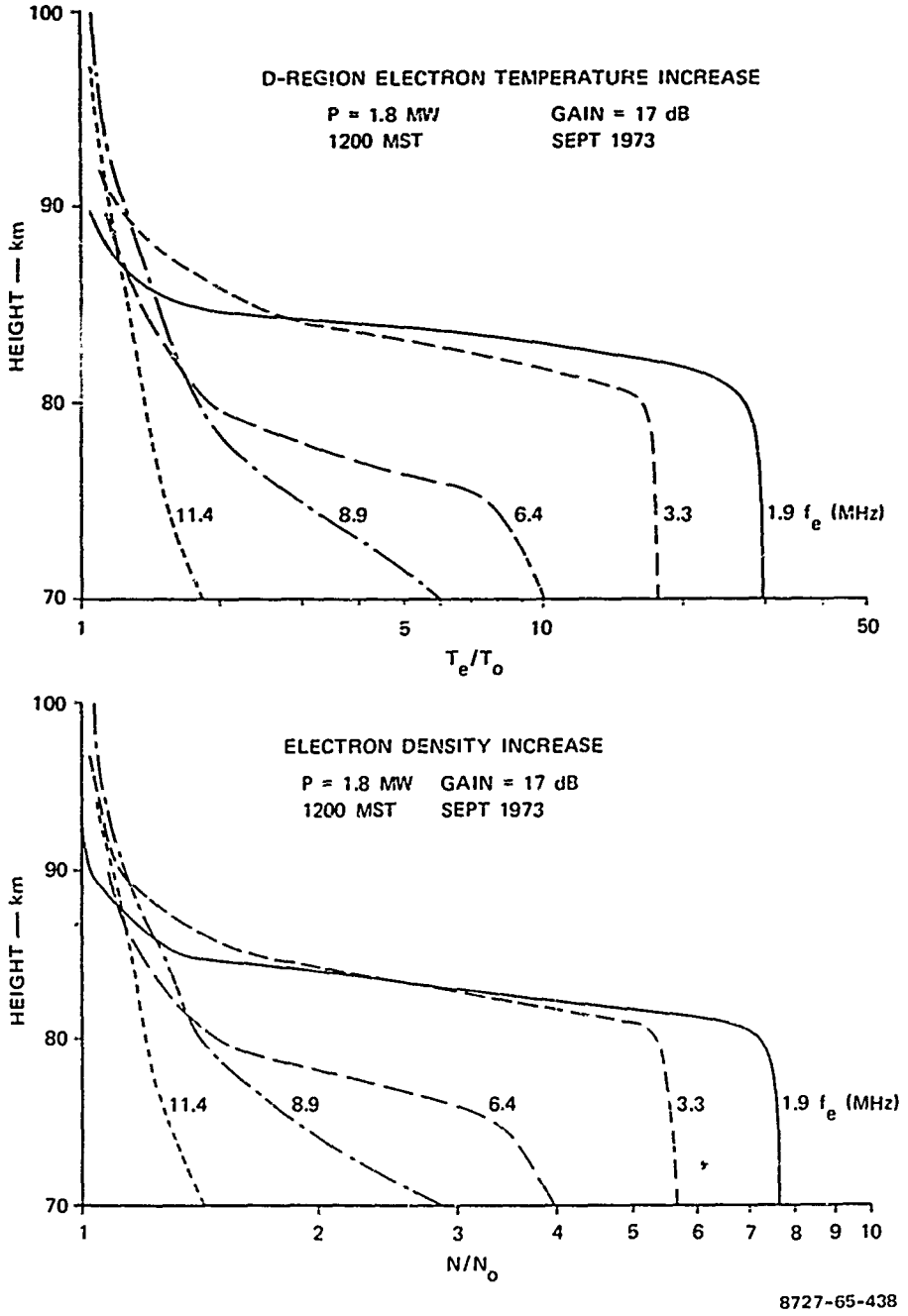

FIGURE 47 PREDICTED STEADY-STATE D-REGION CHANGES FOR MIDDAY HEATING AT VARIOUS EFFECTIVE FREQUENCIES

The predicted midday one-way nonlinear absorption is shown in Figure 48. For O-mode operations the nonlinear absorption onsets between

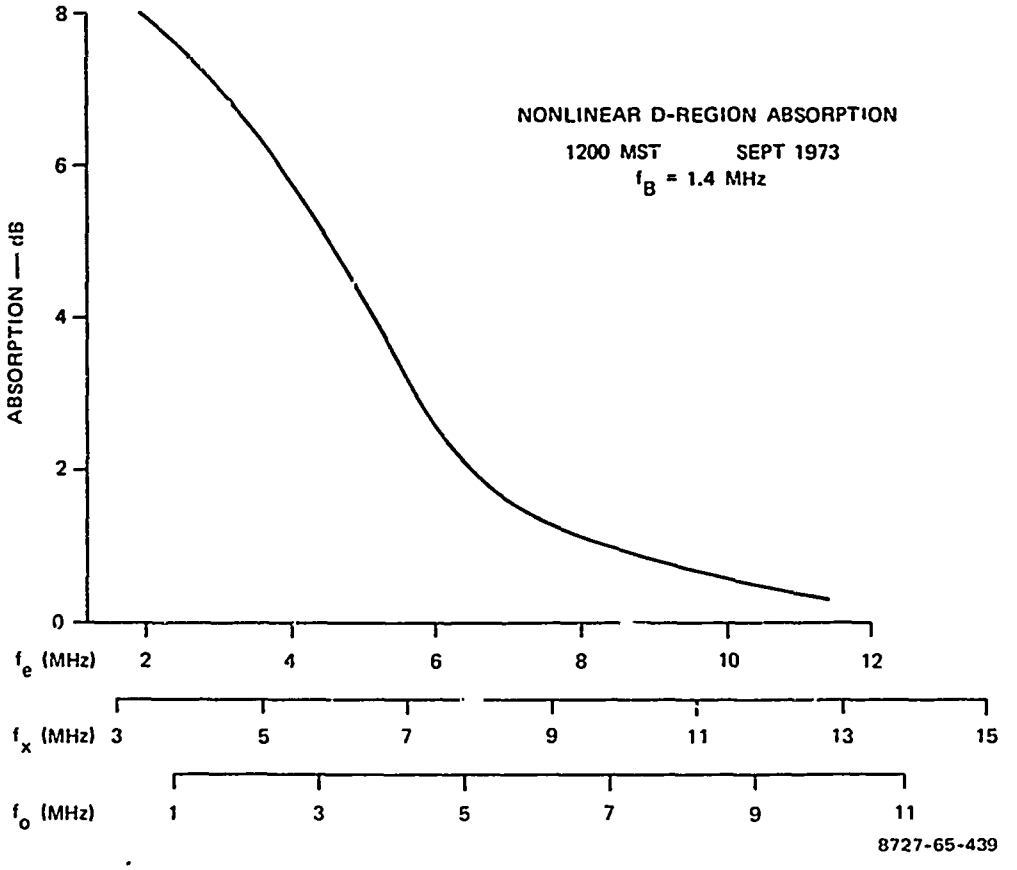

FIGURE 48 INTEGRATED NONLINEAR ONE-WAY ABSORPTION UP TO 100 km AS A FUNCTION OF O- OR X-MODE HEATING FREQUENCY. An electron gyrofrequency of 1.4 has been used in these computations. The illustrated result applies to the model shown in Figure 12.

5 and 7 MHz. Inasmuch as there are uncertainties in the loss rates of about a factor of two, and larger variations in the measured D-layer density profiles from day to day, the estimates of absorption will be uncertain by about 50%. Recent computations of nonlinear D-region effects using about the same ERP but with a typical "quiet sun" density profile derived from rocket measurements (Bowhill) show nonlinear O-mode absorption of 11 dB at f_e = 1.9 MHz and 0.6 dB at f_e = 8 MHz. One can conclude that the amount of nonlinear O-mode absorption above 5 MHz is less than 2 dB!

Up to now we have calculated absorption by assuming that the ambient electron density is unchanged. Although is is true that the electron density will not change due to expansion and fluid motion of the electrons, the chemistry of the D region may be important. This chemistry is known to be very complex and may involve, for example, water-cluster ions and various species of negative ions. However, above 80 km, we may model the chemistry adequately as dissociative recombination, satisfying

$$\frac{dn_e}{dt} = q - \alpha(T)\, n_e^2 \tag{21}$$

where q is the photoionization source of electrons and $\alpha(T)$ is the recombination coefficient. If we assume no increase in q due to the radio heating, the source maintains its equilibrium value, $q = \alpha(T_N)n_o^2$, where n_o is the ambient value of n_e. For NO+ ions, $\alpha = 5 \times 10^{-7}\ (300/T)^{1.2}$ and, if the radio waves suddenly raise the temperature from T_N to T, the electron density will reach an equilibrium density of

$$n_e = \left(\frac{T}{T_N}\right)^{0.6} n_o \tag{22}$$

so that the total absorption will go up as $T^{1.6}$. The steady-state solution is approached after a time on the order of $t_o \sim (2\sqrt{\alpha(T)\alpha(T_N)}n_o)^{-1}$, since the solution of Eq. (21) is

$$n(t)/n_o = [\alpha(T_N)/\alpha(T)]^{1/2} \left(1 - Ae^{-t/t_o}\right) \cdot \left(1 + Ae^{-t/t_o}\right)^{-1} \tag{23}$$

where

$$A = \left(\sqrt{\alpha(T_N)} - \sqrt{\alpha(T)}\right) \cdot \left(\sqrt{\alpha(T_N)} + \sqrt{\alpha(T)}\right)^{-1} \quad . \tag{24}$$

The rate of change of electron density, which is plotted in Figure 49, is inversely proportional to electron density and, therefore, is a sensitive

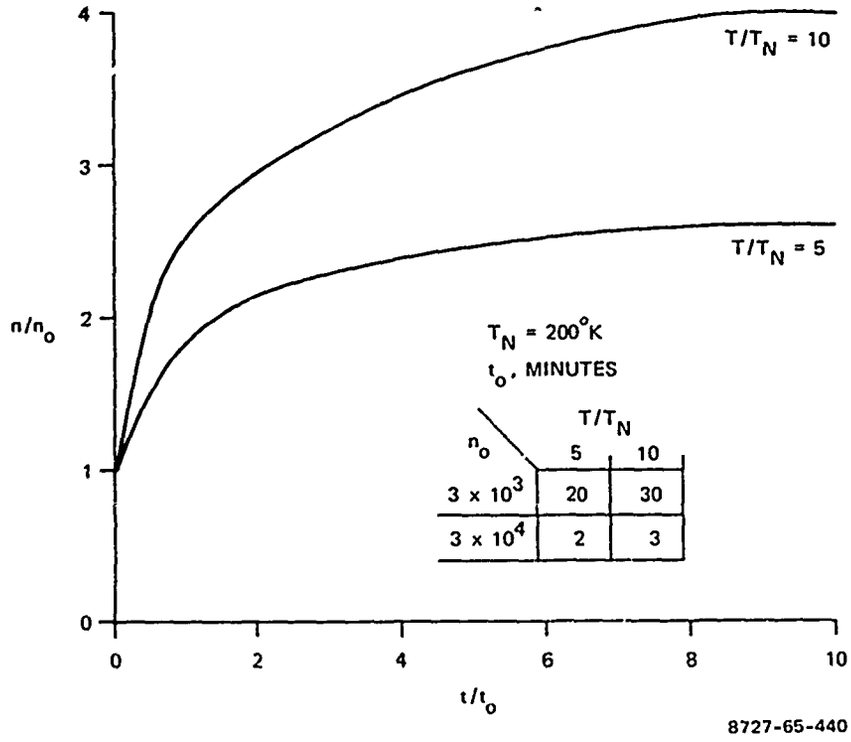

FIGURE 49 RATE OF CHANGE OF ELECTRON DENSITY DUE TO A REDUCTION IN THE RECOMBINATION COEFFICIENT AFTER RF HEATING

function of altitude. This rate of change, which is of the order of minutes, is slow compared with the rate of change of electron temperature which occurs in milliseconds. Note that if $T_e \gg T_n$, then

$$\lim_{t \to o} \frac{dn_e}{dt} = \alpha(T_N)\, N_o^2 \quad ,$$

yielding a direct measurement of the effective recombination coefficient. Similar measurements of $\alpha(T_N)$ can be obtained from the density decay following sustained heating. An independent measurement of T/T_n and N_e/N_o would yield the power-law dependence of $\alpha(T)$, assuming that one species is dominant at the altitude in question.

VI LABORATORY EXPERIMENTS

A. Laboratory Program Motivation and Objectives

In diagnostic field experiments such as those described above, observations of high-frequency ionospheric modification are necessarily limited to the measurement of a relatively small number of parameters in relatively narrow segments of their relevant ranges. The most striking observations--namely, those associated with field-aligned scattering--involve ionospheric structures that develop over a relatively long period of time (fractions of seconds or longer) and hence provide little information concerning the detailed mechanism responsible for the initiation of these structures. Thomson scattering provides information concerning the early-time development but only at a single scattering frequency and with a narrow range of angles so that only a very limited portion of the wave spectrum that exists at altitude can be observed directly.

On theoretical grounds specific physical mechanisms, principally involving parametric instabilities, were proposed.[39] Since direct experimental verification of these hypotheses (for example, by in situ measurements) were not possible, laboratory plasma experiments were initiated to provide at least partial verification of the theoretical pictures. Simulation of the ionospheric phenomena in this way is feasible since many of the critical dimensionless parameters can be at least approximately reproduced in the laboratory. These include the ratios of density gradient length to wavelength (H/λ); cyclotron frequency to plasma frequency (ω_{ce}/ω_{pe}); wavelength to Debye length (λ/λ_D); wave damping (ν/ω); and electromagnetic pump strength ($E^2/4\pi nKT$).

In general, the attempt to verify the theoretical picture has proved successful; even more significantly, the laboratory experiments have revealed the possible critical importance of phenomena not previously considered. Exploitation and application of these new ideas will require an appropriate field experiment to demonstrate that the effects involved occur in the ionospheric plasma as well as in the laboratory plasmas.

B. Program Organization

When the laboratory program was implemented, the most satisfactory available plasma device appeared to be the "Q machine," which has for the last decade served as a work-horse for laboratory plasma investigations. The plasma densities that can be achieved (10^7 to 10^{12} cm^{-3}) correspond to a plasma frequency in a convenient microwave regime, and the electron and ion temperatures are comparable, as is the case in the ionosphere. However, the necessity for a fairly strong magnetic field (5 to 10 kG) results in a value of ω_{ce}/ω_{pe} much larger than in the ionosphere, and the relatively small radial dimensions (typically a few centimeters) preclude large values of H/λ. In addition, the electrostatic modes follow the Gould-Trivelpiece dispersion relation for a bounded plasma rather than the Bohm-Gross dispersion relation characteristic of the ionosphere. These considerations led to the initiation of a parallel effort, involving a much larger quiescent plasma that could operate in a smaller magnetic field. This was achieved by scaling up (by factor of 30 in volume), a type of quiescent plasma device previously developed by Prof. Kenneth McKenzie of UCLA. The details of this facility are described in Table 2 and Figure 50. We simply note here that in addition to permitting a correct ionospheric value of ω_{ce}/ω_{pe} and accommodating Bohm-Gross rather than Gould-Trivelpiece modes, it permits an H/λ ratio of the order of 10^2 and the reasonable matching of ionospheric values. (While this H/λ value simulates the ionosphere in the sense of being very large, it is still

Table 2

TYPICAL OPERATING CHARACTERISTICS*

Density	$n_e \simeq 5.2 \times 10^{10}$ cm^{-3}
Temperature	$kT_e \simeq 1.6$ eV
Low-frequency noise	$\delta n_e / n_e \gtrsim 1\%$ $(0 < f < f_{pi} \sim 7$ MHz)
High-frequency noise	$f \lesssim f_{pe}$, $\Delta f \simeq 200$ MHz
Gradient scale length	$n/\nabla_z n \simeq 100$ cm
	$n/\nabla_r n > 500$ cm
Ambipolar electric field	$E_z \simeq 16$ mV/cm

*For $p \simeq 1.3$ μ (argon), $I_d \simeq 41$ A, $V_d \simeq 35$ V.

somewhat smaller than typical ionospheric values, a fact that must be kept in mind in comparing laboratory and ionospheric results.) In any case, large H/λ is essential in order to have electromagnetic pump waves rather than electrostatic excitation and to allow observations of linear mode conversion, convection of parametric decay waves, and spatial development and localization effects, using suitable probes.

C. Experimental Results

1. QUIPS Results

Electromagnetic-Wave Propagation in Inhomogeneous Plasma. The classical behavior at a cutoff has been verified, including the reduction in group velocity and the increase in phase velocity as the wave approaches the reflection point at $z = z_c$, where z is the axial dimension of the

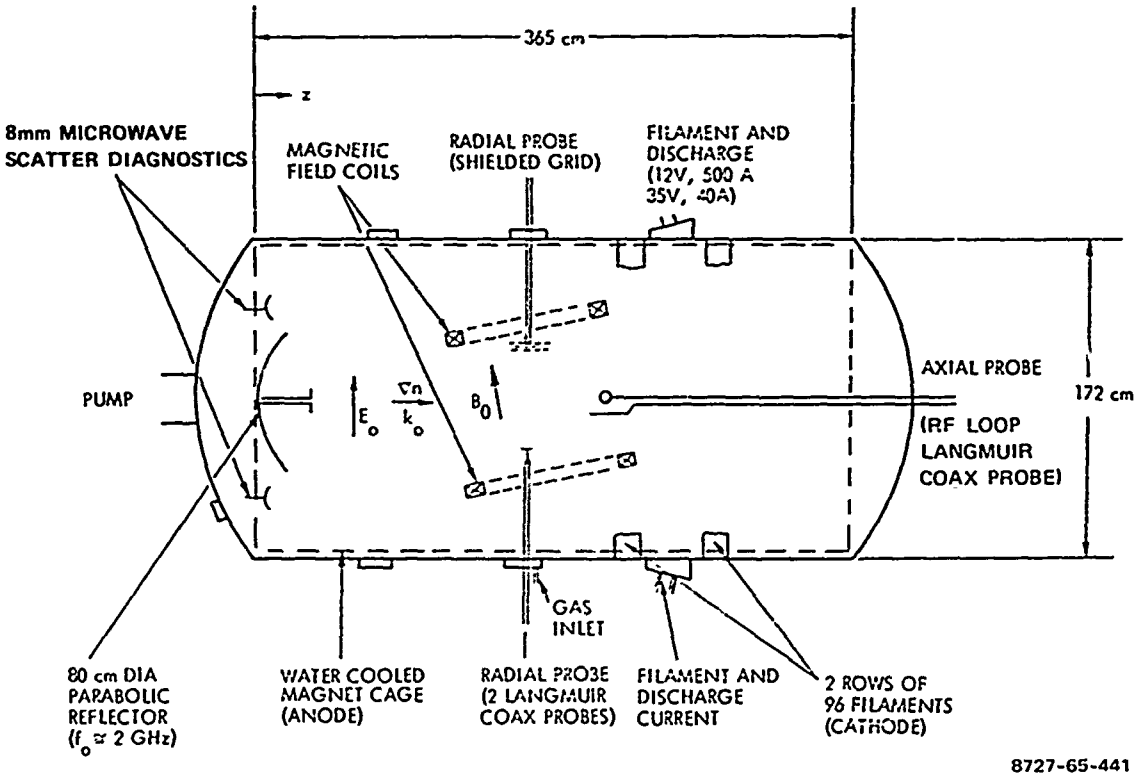

FIGURE 50 SCHEMATIC DIAGRAM OF QUIESCENT PLASMA CHAMBER

chamber, and the wave frequency is $\omega_o = \omega_p(z_c)$. With steady-state excitation, the expected standing-wave pattern associated with wave reflection at the cutoff is observed (Figure 51). However, the spreading of the incident wave due to refraction compensates the expected Airy function swelling. When the transmitter is pulsed on rapidly, temporal development of the propagation process can be followed in detail with no interference from reflection at the chamber walls.

Initial Parametric Instability Results. Parametric decay instabilities have been seen with modest pump powers (1 to 10 W). However, the polarization of the decay waves is completely contrary to initial expectations and the threshold is anomalously low (1 to 2 orders of magnitude less than predicted). Since the electromagnetic pump

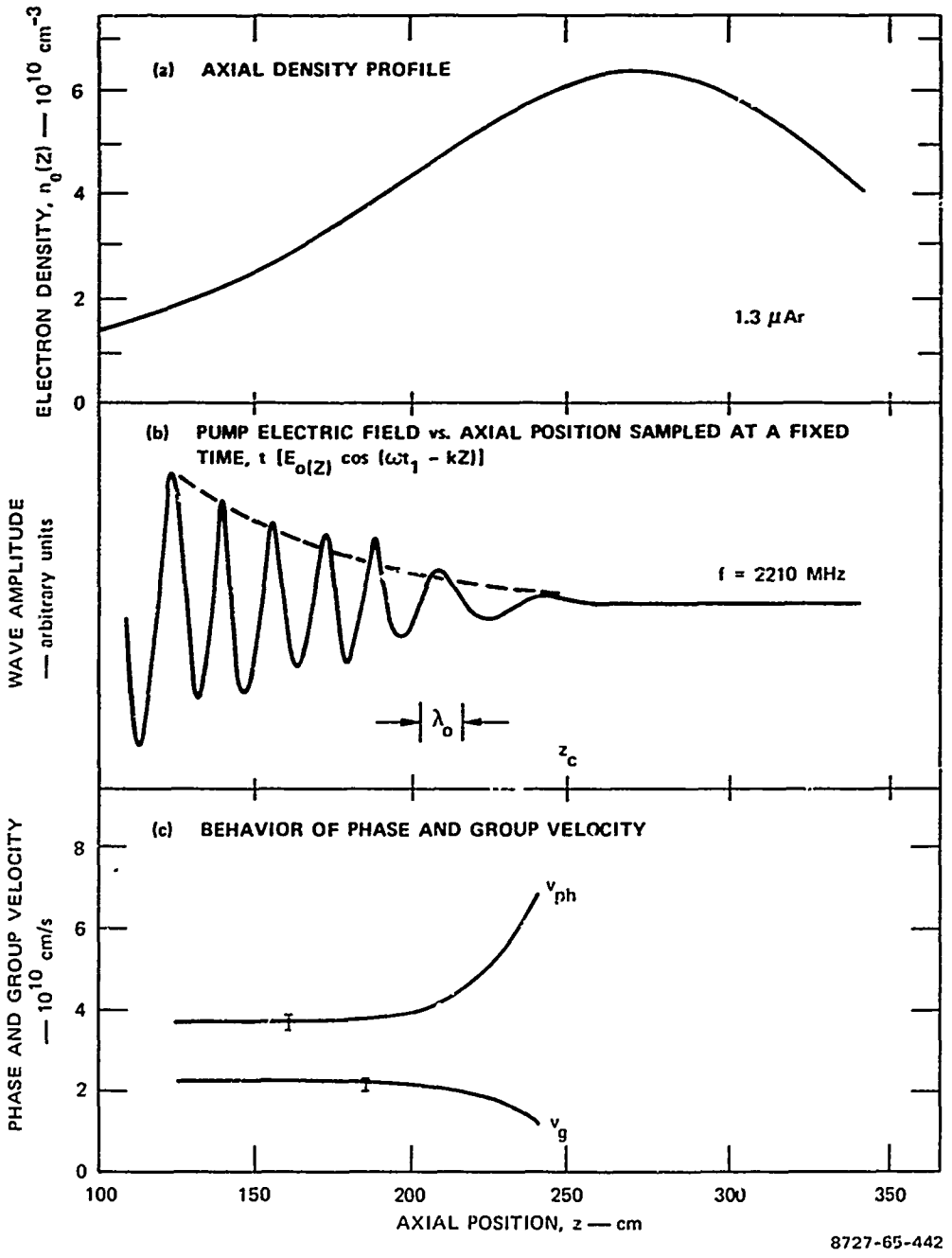

FIGURE 51 AXIAL VARIATION OF CHAMBER PARAMETERS

propagates in the axial direction, its electric field is radial. The consequent radial oscillations of the plasma electrons should then give rise to electrostatic decay waves[40,41] (the ion acoustic wave $\omega_{ia} = kC_s$, and the electron plasma, or Langmuir, wave, $\omega_L = (\omega_{pe}^2 + k^2C_e^2)$ having both wave vector and electric field in the radial direction. However, experimental observations show that both waves propagate in the axial direction.

Linear Mode Conversion. The explanation of the axially propagating plasma waves, described above, is provided by linear mode conversion.[42] Oblique incidence of the electromagnetic wave results in an axial component of the electric field--i.e., a component parallel to the density gradient and hence to an oscillating charge separation that tends to become very large at the resonant point, $\omega_o = \omega_p$. The associated self-consistent short-wavelength axial electrostatic field will be limited in amplitude [by either thermal effects (finite Debye length) or collisional effects], but in both the ionospheric plasma and in QUIPS it can attain a value very much larger than that of the incident electromagnetic wave. Hence, this linearly converted electrostatic wave will serve as the pump for the parametric instability, rather than the incident electromagnetic wave.

Detailed experimental observations[43] of the amplitude and shape of the short-wavelength structure in the electric field at the resonance point support this picture (Figure 52). Theory predicts a shape given by one of the inhomogeneous Airy functions, and the experimental agreement is excellent. Direct measurement of the amplitude of the linearly converted mode has proved very difficult because physical probes sharply reduce it. A very rapid turn-on of the pump (within a few nanoseconds) produces perturbations of plasma density in the resonant region caused by the ponderomotive force $< \nabla E^2/8\pi >$. Since the measured amplitude of

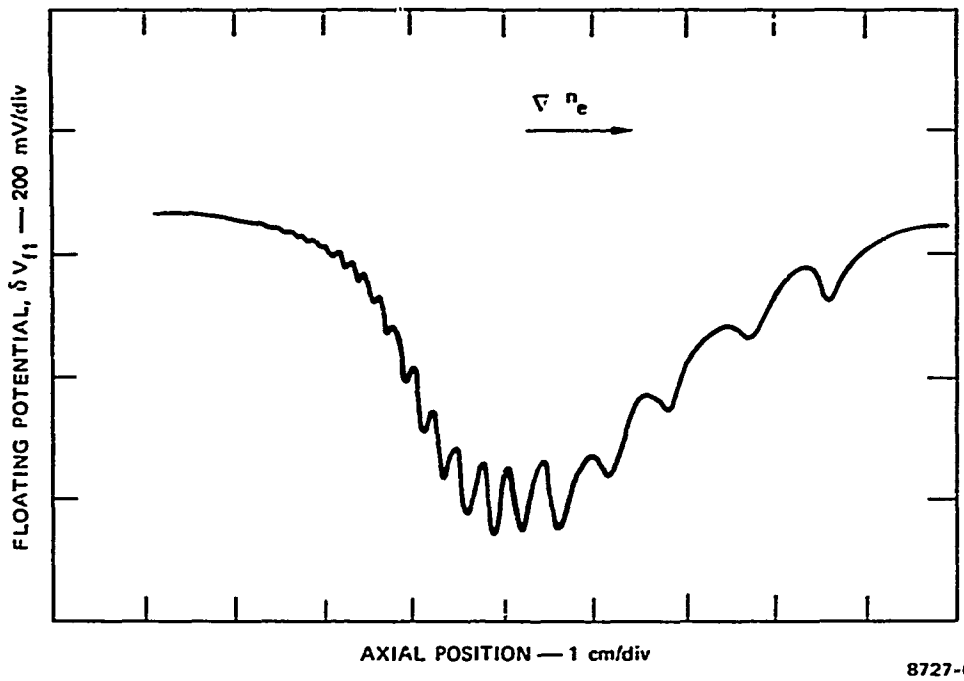

FIGURE 52 CHANGE IN FLOATING POTENTIAL DUE TO RECTIFICATION OF ELECTRON-PLASMA-WAVE SIGNAL ON PROBE SHEATH

the electromagnetic pump is too small by two orders of magnitude to produce the observed density perturbations ($\delta n/n \approx$ 1-5%), we have concluded that the ponderomotive force associated with the linearly converted mode must be responsible. Indeed, the theoretically predicted amplitude for this mode is consistent with that required to produce the observed density perturbations.

Detailed Study of Parametric Instabilities. Both the Langmuir and ion acoustic decay waves have been observed propagating in the axial direction[44] as is expected[45] for the axial electrostatic pump arising from linear mode conversion (Figure 53). A clear threshold can be detected, above which there is frequency broadening as predicted by theory. Pulsing the pump allows observation of the time evolution of the parametric decay process (Figure 54).

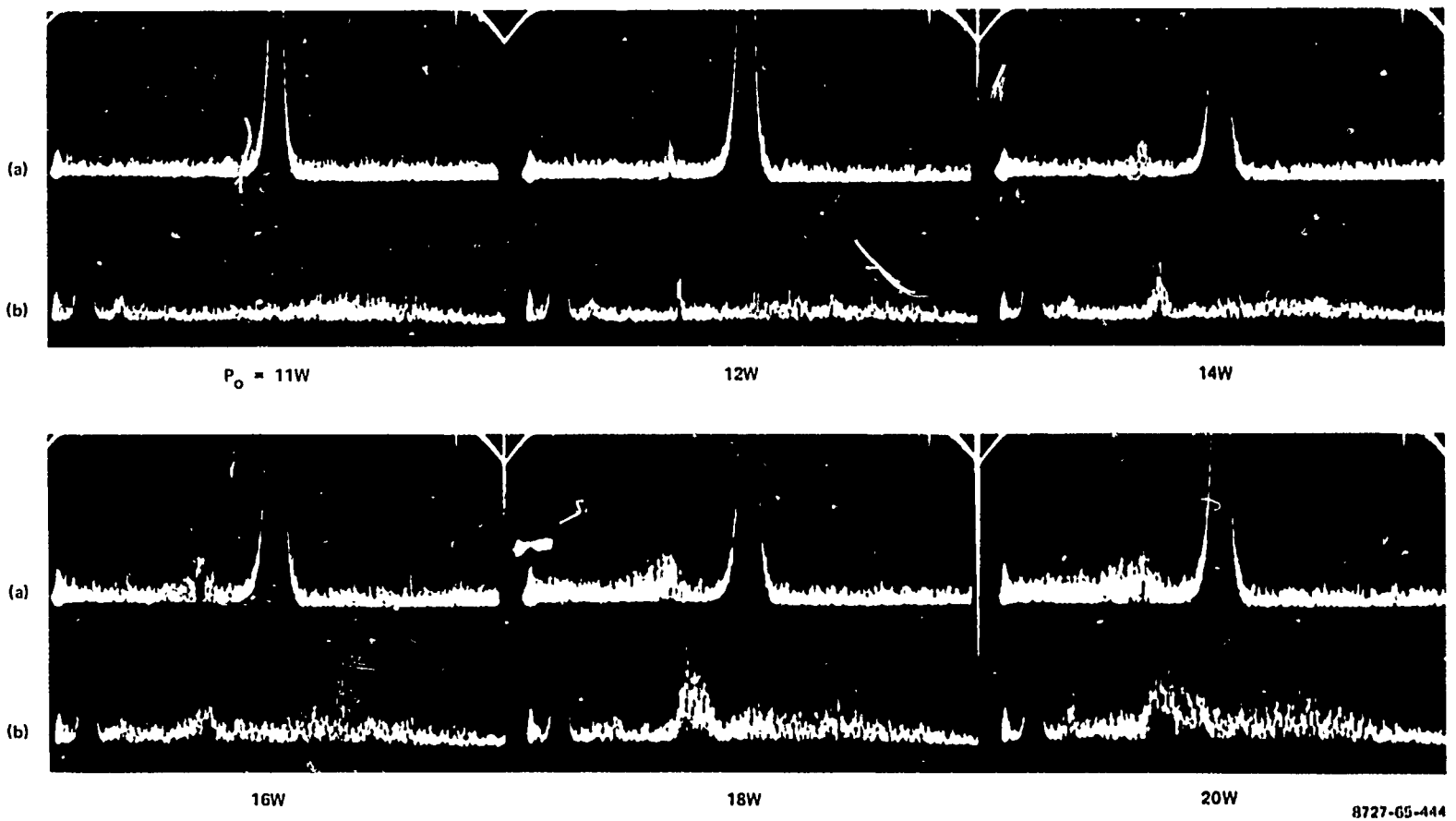

FIGURE 53 SIMULTANEOUS FREQUENCY SPECTRA OF PROBE SIGNALS AT DIFFERENT PUMP POWER LEVELS, P_o. "a" Traces: High-frequency spectrum showing pump line and unstable electron plasma waves below the pump (300 kHz/div). "b" Traces: Low-frequency spectrum with zero-beat line and unstable ion acoustic waves.

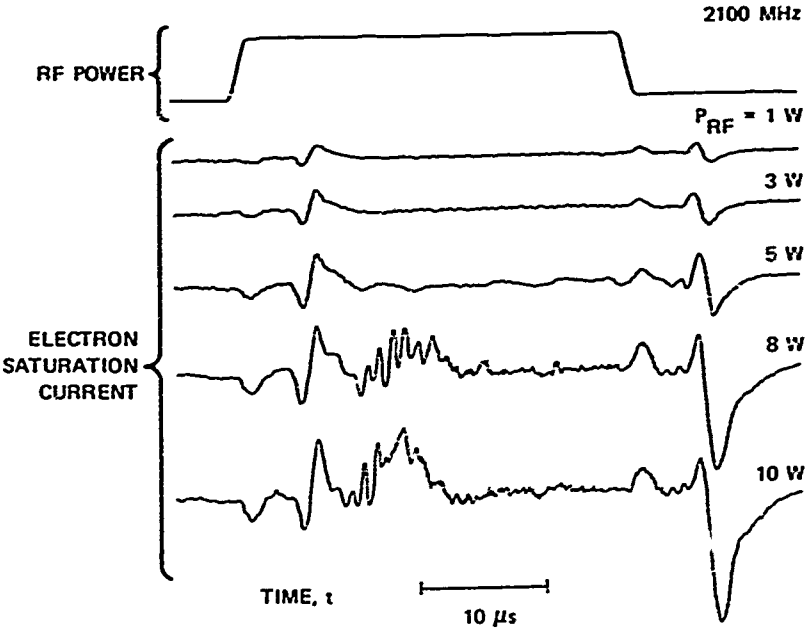

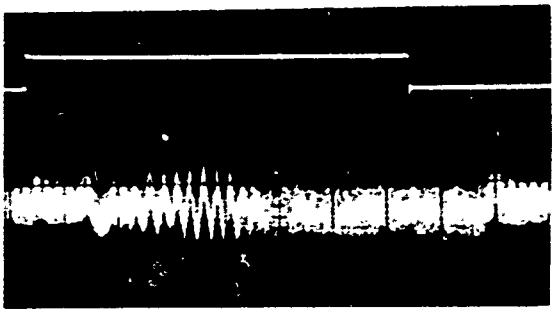

8727-65-445

FIGURE 54 TIME EVOLUTION OF PARAMETRIC ION OSCILLATIONS AND DENSITY PERTURBATION BY PONDEROMOTIVE FORCE

Density Modifications due to the Ponderomotive Force. In view of the large electrostatic field produced by linear mode conversion as discussed above, density perturbations proportional to incident power would be expected and are indeed found (Figure 55). Careful measurements with pulsed pump signals and detailed Langmuir probe observations show that the observed signals are indeed due to changes in density rather than electron temperature or ionization, and the density perturbations are observed to propagate with a speed approximately equal to the ion

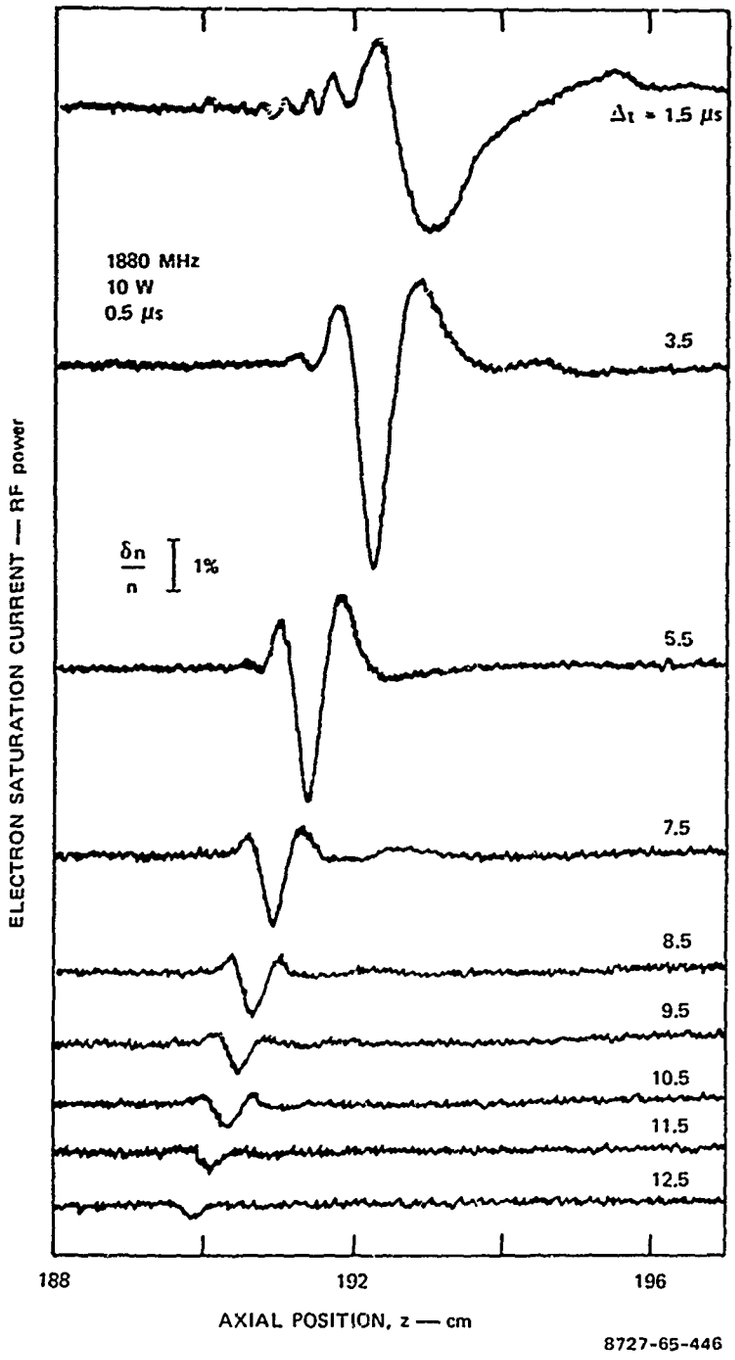

FIGURE 55 DENSITY PERTURBATION AT TIME Δt AFTER TURN-OFF OF MICROWAVE PULSE

acoustic velocity c_s as expected. Under steady-state excitation the peak of the linearly mode-converted electrostatic field coincides with the local (relative) minimum of plasma density. No threshold for these effects is expected or observed, beyond that set by diagnostic limitations; these correspond to power levels of a few watts.

Effect of an External Magnetic Field. Addition of a 200-gauss magnetic field approximately reproduces the ionospheric value of ω_{ce}/ω_{pe}. While further work remains to be done, we have found that addition of the magnetic field does not alter the linear-mode-conversion phenomena or the associated generation of a density perturbation significantly. However, the cross-field perturbations propagate somewhat slower than in the field-free case.

Double-Resonance Phenomena. The use of two electromagnetic pump frequencies separated by a suitably chosen low frequency, ω_1, in the ion acoustic regime has been explored in the QUIPS with a view toward devising suitable ionospheric field experiments.[46] If the separation frequency, ω_1, is chosen to equal the frequency of the ion acoustic waves that occur for single pump parametric instability, the threshold for that instability is greatly reduced. Other choices for ω_1 provide the freedom to select the low frequency generated in the plasma (Figure 56).

Scattering of 8-mm Waves. This system is now operational and several experiments have been carried out. With double-resonance excitation, observation of the ion acoustic component has been successful (Figure 57).

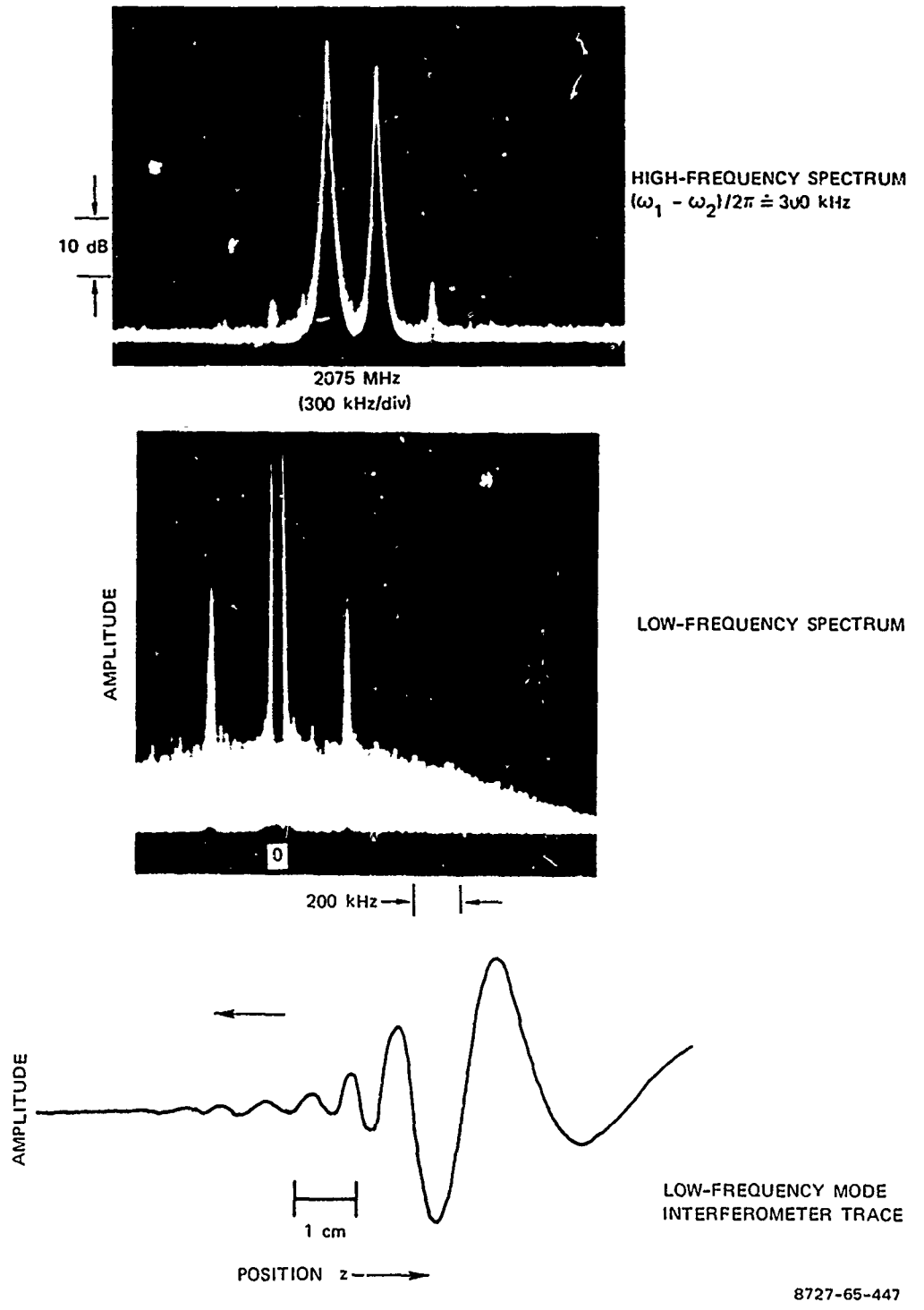

FIGURE 56 DOUBLE-PUMP ION OSCILLATIONS

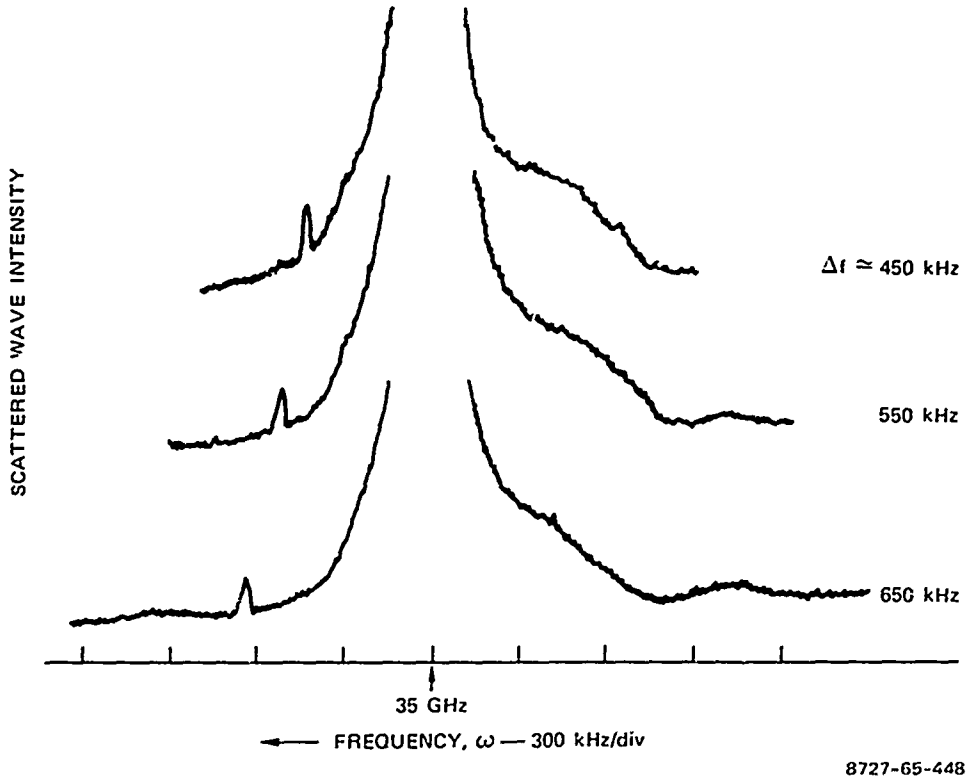

FIGURE 57 35-GHz THOMSON SCATTERING SPECTRUM

2. Q-Machine Results

The Q-machine produces a cylindrical plasma (3-cm diameter, 125-cm length) with comparable electron and ion temperatures; negligible neutral collisions $10^{-1} < \nu_{ci}/\omega_{pi} < 10$; densities in the range $10^{7} < n < 10^{12}$ cm^{-3}; strong axial magnetic field ($\omega_{pe} < \omega_{ce}$); and unmagnetized ions ($\omega_{ci} \ll \omega_{pi} \ll \omega_{pe}$). The parametric decay instability is excited[47] by an RF electric field, $\omega_{pump} \approx \omega_{pe}$, oriented either parallel or perpendicular to the magnetic field, by parallel plates surrounding the plasma. The principal results are:

- Identification of the parametric ion-acoustic decay instability. This is achieved by demonstrating detailed observance of the usual frequency and wave-number sum rules and a density dependence of the instability bandwidth and threshold in agreement with

theory. However, the steady-state (low-frequency/high-frequency) intensity ratio is constant ($\approx 10^{-3}$) and independent of pump intensity, in apparent disagreement with linear theory. We find $E^2_{inst} \propto (E^2_{pump})^n$, with $n \geq 4$ near threshold and $n \simeq 1$ well above threshold.

- Measurements of enhanced absorption of electromagnetic waves and effective collision frequency. Using parallel excitation in a microwave cavity and measuring the Q value we find that onset of the parametric instability coincides with enhanced absorption and electron heating.[47] These can be calculated with the use of an effective pump-power-dependent collision frequency in agreement with a theory involving nonlinear Landau damping.

- Ion heating. Using parallel excitation we observe intense stochastic ion heating, comparable to the electron heating;[48] this was related to the fluctuating electric fields of the decay instability. Ion temperature rise times τ_H exceed somewhat the instability growth times, $1/\gamma$, ($1/\omega_{pi} < 1/\gamma < \tau_H \ll 1/\omega_{ci}$) but are many orders of magnitude smaller than $1/\nu_{ei}$, indicating ion heating by the ion acoustic decay instability. Using perpendicular excitation, just above the lower hybrid frequency, the decay instability is observed to heat the ions to 100 times their initial temperature.[49]

D. Ionospheric Implications of Laboratory Observations

Theoretical arguments,[45,50] now proven by the QUIPS experiments in a magnetic field reported here, indicate that linear conversion may occur in the ionosphere. The resulting electrostatic waves will propagate at a very small angle to the local density gradient (assumed, for the moment, to be predominantly vertical). They would therefore scatter RF waves as from a horizontal mirror in the disturbed region. Estimates of the cross section suggest that it varies as the square of the scattering frequency up to perhaps as much as 1 GHz vertically, and up to a correspondingly higher frequency at other angles; and that it may be quite large. Of course, since this effect is linear, it has no threshold and

hence its observation is limited only by the sensitivity of the scattering link. Thus, if the cross section is sufficiently large--a question that can be resolved only by performing field experiments--scattering from these waves may be observed at reduced pump powers.

Vertically propagating linearly converted waves provide a large field component perpendicular to the magnetic field and hence may drive any of the several unstable perpendicular plasma modes and contribute to aspect-sensitive scattering. Similarly, the ponderomotive forces these waves produce, which in turn produce large density perturbations in the laboratory, may contribute significantly to the field-aligned density perturbations observed in the ionosphere.

If the short-wavelength spectrum of the field-aligned density fluctuations, α_1, is sufficiently large (i.e., $|\nabla \alpha_1|/R_c \ll 1$), then the density gradient will be predominantly perpendicular to the magnetic field and the linearly converted waves will propagate in the perpendicular direction. This may well contribute to the very sharp field-normal VHF and UHF sideband displaced by the heater frequency observed at WSMR.

E. Further Research

The following appear to be potentially fruitful areas of future laboratory research:

- Ponderomotive Force Effects in Magnetic Field. In addition to potentially shedding light on the formation of large magnetic-field-aligned density fluctuations, ponderomotive-force studies may also lead to the discovery of hitherto unanticipated effects such as beam plasma instabilities and wave or particle trapping.
- Bernstein Modes. The threshold for parametric decay into Bernstein waves is theoretically[51] within the capacity of the Boulder antenna. These waves would be short enough to scatter S and C radar waves.

- Variable Ion Damping. By the introduction of a small amount of He in the QUIPS, the ion damping can be varied to better simulate the strong ion damping due to $T_e = T_i$ in the ionosphere. In addition to changing thresholds this can significantly alter thermal transport effects.

- Thermal Effects. It has been suggested that a new thermal instability[52,53] may be responsible for large-scale field-aligned irregularities. The hypothesized interactions have never been explored in the laboratory.

VII CONCLUSIONS AND RECOMMENDATIONS

It can be concluded that the IVORY CORAL program has been very successful in meeting program objectives and in the richness of our scientific results, although several questio. , remain unanswered with regard to ionospheric modification. Our conclusions with regard to ionospheric modification will be briefly presented here, first in somewhat general terms and then somewhat more specifically.

The F region of the ionosphere can be modified in a reproducible manner with RF energy. Conclusive data show that approximately 50 $\mu W/m^2$ of RF energy in the frequency range of 0.8 to 1.1 times the f_oF2 critical frequency are adequate. The absorption of approximately 50% of the incident radiation by ohmic and nonlinear heating in approximately equal amounts results in a modified volume of the ionospheric F region. This modified volume has been investigated extensively, resulting in rather complete physical description of the volume. This physical description has been put in model form (see Section IV), which represents a major output of the program.

Some qualitative concluding remarks about the uses of the model are in order. Intelligible information has been scattered off the modified volume over the horizon using rather modest equipment and power levels. These experiments took place over a range of appro: ately 3000 km. The geometry, power levels, and magnitude of the scattered energy are in agreement with the model within experimental error. The geometric pattern in which the energy is scattered takes the form of east-west paths on the surface of the earth. These paths are about 500 to 800 km in north-south extent and 2000 to 3000 km in east-west extent. Communication outside these zones is not possible. It has been concluded that

for some applications this severe aspect sensitivity limits the usefulness of the IVORY CORAL concept. Limited attempts to reduce this aspect sensitivity have not been successful.

The current state of understanding in several areas of ionospheric modification is briefly summarized below:

- Field-normal scattering and refraction for wavenumbers (k) from 0.01 to 10 m^{-1} are well understood. Scattering during both day and night are included, with highest efficiency occurring at night and lowest at 1400 ± 2 hours local time.
- In the E region, scattering drops off less rapidly for $k > 10\ m^{-1}$.
- Gross changes in electron density (N_e), electron temperature (T_e), and collision frequency (ν) have been produced and are understood in the F region. Generation and understanding of the corresponding quantities for the D and E regions are beginning to emerge.
- Electron-density dependency on heater power has been determined to be

$$\left(\frac{\overline{\Delta N_e}}{N_e}\right)^2 \propto P_H^n$$

where $0.5 \leq n \leq 1.0$ for most cases.

- Characteristics of superthermal plasma waves (except parallel to the geomagnetic field) and electrons that are responsible for the generation of plasma lines, airglow, and parasitic plasma waves are understood. No inconsistencies exist between experimental observation of these quantities at Platteville and at Arecibo.
- The theory of plasma lines is partially understood; however, inconsistencies remain.
- Theory of low-wavenumber (0.01 to 1 m^{-1}) generation and characteristics is not understood. At present, only suggested approaches exist.

- Theory of high wavenumbers ($> 1\ m^{-1}$) is only partially understood. The excitation is not clear.
- Radio-wave scattering and refraction aspects for centerline scattering are fully understood (limited only by our understanding of the scattering irregularities).
- Low wavenumbers (artificial spread F), which produce scintillation, appear through the topside of the F layer, and preliminary data suggest they may extend to the geomagnetic conjugate region.
- Finally, it has been concluded that most of the effects that are presently understood may be valid only at mid-geomagnetic latitudes under quiet and/or moderately disturbed ionospheric conditions. Extrapolations to other latitudes may be subject to question.

The recommended tasks briefly stated below have been proposed in one form or another to various agencies. Only limited interest was generated from the application point of view. However, the implementation of these recommendations would have scientific value and they are included here for this reason and for the sake of completeness. In decreasing order of importance, the tasks are:

- Determination of geographic dependencies of the IVORY CORAL concept.
- Investigation of the possible use of artificial spread-F and field-aligned scattering as an ambient-drift diagnostic.
- Characterization of effects in the E region.
- Continuation of plasma-wave scattering at other frequencies and geometries.
- In situ satellite diagnostic measurements in the modified volume.
- Investigation of natural whistler modification producing enhanced ducts and superthermal electrons.
- Generation of D-region effects.
- Laboratory and field experiments in generation of Bernstein modes (S-band scattering).
- Measurement of forward scattering in the heated D region.

- More accurate determination of tentatively identified conjugate-point effects and addition of topside soundings.
- Determination of the feasibility of using airglow lines as an energy-partition diagnostic.
- Investigation of possible gains to be realized using oblique heating methods.
- Better determination and characterization of small-scale irregularities that are responsible for the aspect sensitivity of the scattering.

Appendix A

DETERMINATION OF SPECULAR SURFACE

The specular surface is defined by a region of points where the external bisector to the angle between the incidence and scattering directions achieves perpendicularity to the direction of the earth's magnetic field. The determination of the specular surface within the volume of the scattering medium for a given radar configuration is one of the main modeling tasks. An analytic solution was obtained to the problem for the case of curved earth and dipole model for the earth's magnetic field but neglecting the ionospheric refraction effects. The solution provides the height of a specular point for a specified location on earth and it results from a cubic equation that is formulated by equating the angle between the incident ray and the magnetic field to that between the scattered ray and the magnetic field. The solution was adapted to a CDC 6700. A more general program has been developed by SRI to compute the specular surface; this program takes the ionospheric refraction effects also into account.

Appendix B

FLOWCHART FOR COMPUTER ADAPTATION OF THE MODEL

Figure B-1 shows a scheme for computer adaptation of the scattering model.

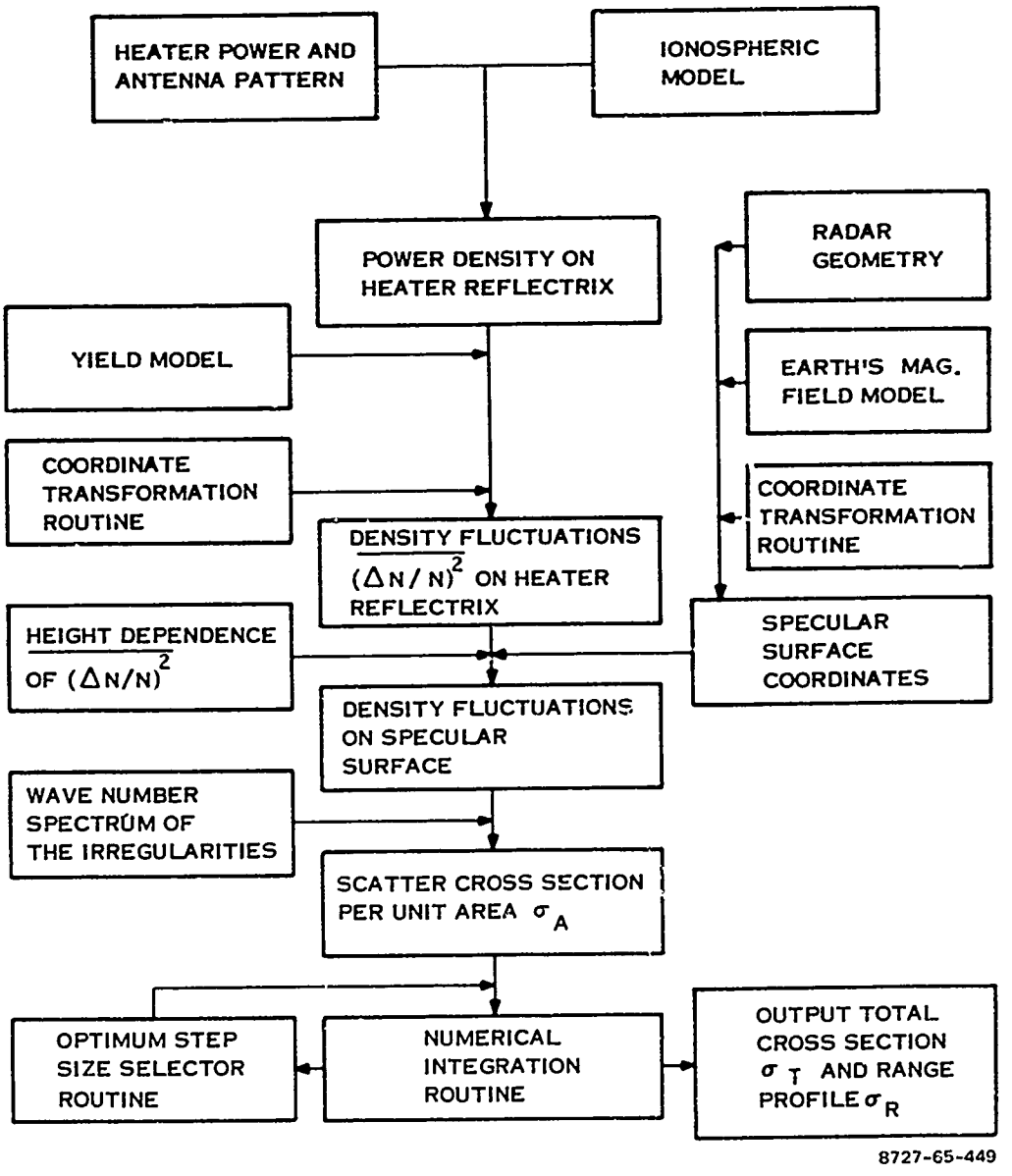

FIGURE B-1 FLOWCHART FOR COMPUTER ADAPTATION OF THE MODEL

REFERENCES

1. W. F. Utlaut, "An Ionospheric Modification Experiment Using Very High Power, High Frequency Transmission," J. Geophys. Res., Vol. 75, pp. 6402-6405 (1970).

2. R. L. Showen, "Artificial Heating of the Lower Ionosphere," J. Geophys. Res., Vol. 77, pp. 1923-1933 (1972).

3. W. F. Utlaut and E. J. Violette, "Further Ionosonde Observations of Ionospheric Modification by a High Powered Ground-Based Transmitter," J. Geophys. Res., Vol. 77, pp. 6804 (1972).

4. Proceedings of the IVORY CORAL 1973 Technical Review Meeting--Vol. II: Experiments, Contract N00014-70-C-0413, Stanford Research Institute, Menlo Park, Calif. (April 1973).

5. P. A. Fialer, "SFCW Observations of Field-Aligned Scattering," in Proceedings of the IVORY CORAL 1973 Technical Review Meeting--Vol. II: Experiments, Contract N00014-70-C-0413, Stanford Research Institute, Menlo Park, Calif. (April 1973).

6. L. B. Wetzel, "NRL Magnetometer Experiments for PRAIRIE SMOKE I," in Proceedings of PRAIRIE SMOKE I RF Measurements Data Workshop, 25, 26, 27 January 1972, Contract N00014-70-C-0413, Stanford Research Institute, Menlo Park, Calif. (March 1972).

7. I. J. Kantor, "Artificial Heating Paradox of the Lower Ionosphere," M.S. Dissertation, Rice University, Houston, Texas (1971).

8. W. E. Gordon, H. C. Carlson, and R. L. Showen, "Ionospheric Heating at Arecibo: First Tests," J. Geophys. Res., Vol. 76, pp. 7808-7813 (1971).

9. Proceedings of PRAIRIE SMOKE V RF Measurements Data Workshop--8, 9 November 1973," Contract N00014-70-C-0413, Stanford Research Institute, Menlo Park, Calif. (March 1974).

10. E. M. Allen and B. R. Pendyala, "Angular Spectrum of Spread-F Ionogram Returns," in Proceedings of the IVORY CORAL 1973 Technical Review Meeting--Vol. II: Experiments, Contract N00014-70-C-0413, Technical Report, Vol. II, Stanford Research Institute, Menlo Park, Calif. (April 1973).

11. T. M. Georges, "Amplification of Ionospheric Heating and Triggering of 'Spread-F' by Natural Irregularities," J. Geophys. Res., Vol. 75, pp. 6436 (1970).

12. I. J. Kantor, "Enhanced Plasma Lines Excited by HF Waves," Ph.D. Dissertation, Rice University, Houston, Texas (1972).

13. F. W. Perkins, C. Oberman, and E. J. Valeo, "Parametric Instabilities and Ionospheric Modification," Report PPL-AP69, Princeton University Plasma Physics Laboratory, Princeton, N.J. (to appear in J. Geophys. Res., 1974).

14. Y.-Y. Kuo and J. A. Fejer, "Spectral Line Structure of Saturated Parametric Instabilities," Phys. Rev. Lett., Vol. 29, p. 1667 (1972).

15. Proceedings of the PRAIRIE SMOKE IV RF Measurements Data Workshop, Contract N00014-70-C-0413, Stanford Research Institute, Menlo Park, Calif. (7 March 1973).

16. B. R. Pendyala and G. D. Thome, "A Model for 'On-Frequency' Field Aligned Scattering," in Proceedings of the PRAIRIE SMOKE Yield Model Workshop, 17-18 July 1973, Contract N00014-70-C-0413, Stanford Research Institute, Menlo Park, Calif. (1973).

17. H. G. Booker, "A Theory of Scattering of Nonisotropic Irregularities with Application to Radar Reflections from the Aurora," J. Atmos. Terr. Phys., Vol. 8, pp. 204-221 (1956).

18. J. Minkoff, "Analysis and Interpretation of Aspect-Dependent Ionospheric Radar Scatter," J. Geophys. Res., Vol. 78, No. 19, pp. 3865-3880 (1973).

19. B. R. Pendyala and G. D. Thome, "An RF Scattering Model for a Random Distribution of Irregularities," in Proceedings of the PRAIRIE SMOKE RF-Scattering Model Workshop, 18-19 July 1972, Contract N00014-70-C-0413, Stanford Research Institute, Menlo Park, Calif. (1972).

20. V. R. Frank, L. E. Sweeney, Jr., and P. A. Fialer, "A Scattering Model Verification Experiment," in Proceedings of the IVORY CORAL 1973 Technical Review Meeting--Vol. II: Experiments, Contract N00014-70-C-0413, Stanford Research Institute, Menlo Park, Calif. (1973).

21. D. F. DuBois, M. V. Goldman, and D. McKinnis, "Nonlinear Wave Optics at Parametric Pump Radiation in an Inhomogeneous Plasma," Report UC-1004, University of Colorado, Boulder, Colo. (to appear in Phys. Fluids, December 1972).

22. G. Meltz and N. M. Tomljanovich, "Deviative and Anomalous Absorption of Radio Waves by Parametrically Excited Regions of the Ionosphere," Summary of Theoretical Meeting of November 17, 1972, pp. 249, Summary Report 2, Contract DAAH01-71-C-0968, Battelle Columbus Laboratories, Columbus, Ohio (December 1972).

23. J. B. Minkoff and P. Kugelman, "Preliminary Summary Results of PRAIRIE SMOKE I Experiments," in Proceedings of PRAIRIE SMOKE I, Contract N00014-70-C-0413, Stanford Research Institute, Menlo Park, Calif. (March 1972).

24. M. V. Goldman and D. F. DuBois, "Stimulated Diffusion Scattering," Summary of Theoretical Meeting of November 17, 1972, pp. 8, Summary Report 2, Contract DAAH01-71-C-0968, Battelle Columbus Laboratories, Columbus, Ohio (December 1972).

25. F. W. Perkins, F. J. Valeo, and G. D. Thome, "Thermal Self-Focusing of Electromagnetic Waves in Plasmas," Report PPL-AP71, Princeton University Plasma Physics Laboratory, Princeton, N.J. (submitted to Phys. Rev. Lett., 1974).

26. E. M. Allen, G. D. Thome, P. B. Rao, and R. L. St. Germain, "The Angular Distribution of Spread-F Returns from an Artificially Modified Ionosphere" (to be submitted to the J. Geophys. Res. (1973)).

27. F. W. Perkins and P. K. Kaw, "On the Role of Plasma Instabilities in Ionospheric Heating by Radiowaves," J. Geophys. Res., Vol. 76, pp. 282 (1971).

28. B. Bezzerides and J. Weinstock, "Nonlinear Saturation of Parametric Instabilities," Phys. Rev. Lett., Vol. 28, pp. 481 (1972).

29. F. W. Perkins, "Parametric Instabilities in Collisional Plasmas," Bull Am. Phys. Soc., Vol. 18, pp. 1335 (1973).

30. J. A. Fejer, "Generation of Large-Scale Field-Aligned Density Irregularities in Ionospheric Heating Experiments," Paper presented at the AGARD Meeting on Nonlinear Effects in Electromagnetic Wave Propagation, Edinburgh (1973).

31. N. M. Tomljanovich, "Self-Focusing of Intense Radio Waves in the Ionosphere," Report M73-108, Mitre Corporation, Bedford, Mass. (October 1973).

32. G. Meltz and R. E. LeLevier, "Heating the F Region by Deviative Absorption of Radio Waves," J. Geophys. Res., Vol. 76, pp. 6406 (1970).

33. W. E. Gordon and H. C. Carlson, "Parametric Instabilities in the Ionosphere Excited by Powerful Radio Waves over Arecibo," Proceedings of the AGARD Conference on Nonlinear Effects in Electromagnetic Wave Propagation, Edinburgh (1973).

34. N. M. Tomljanovich, "Self-Focusing of Electromagnetic Waves in Plasmas," in Summary of Theoretical Meeting of 17 November 1972, Summary Report 2, Contract DAAH01-71-C-0968, Battelle Columbus Laboratories, Columbus, Ohio (1972).

35. L. H. Holway, Jr., and G. Meltz, "Heating of the Lower Ionosphere by Powerful Radio Waves" (to be published in J. Geophys. Res., 1973).

36. R. L. Showen, "Artificial Heating of the Lower Ionosphere," J. Geophys. Res., Vol. 77, pp. 1923 (1972).

37. A. Dalgarno, "Collisions in the Ionosphere," in Advances in Atomic and Molecular Physics, Vol. 4, D. R. Bates, Ed., pp. 381-410 (Academic Press, New York, N.Y., 1968).

38. W. F. Utlaut, "A Survey of Ionospheric Modification Effects Produced by High-Power HF Radio Waves," in Proceedings of the AGARD Conference on Nonlinear Effects in Electromagnetic Wave Propagation, Edinburgh (1973).

39. F. W. Perkins and P. K. Kaw, J. Geophys. Res., Vol. 76, pp. 282 (1971).

40. D. F. DuBois and M. V. Goldman, Phys. Fluids, Vol. 15, pp. 919 (1972).

41. E. Valeo, F. Perkins, and C. Oberman, Phys. Rev. Letters, Vol. 28, pp. 340 (1972).

42. V. L. Ginzberg, Propagation of Electromagnetic Waves in Plasma (Gordon & Breach, New York, N.Y., 1961).

43. R. S. Stenzel and A. Y. Wong, APS Bull., Vol. 18, pp. 1258 (1973).

44. A. Y. Wong and R. S. Stenzel, APS Bull., Vol. 18, pp. 1258 (1973).

45. D. Arnush, B. D. Fried, and K. Nishikawa, APS Bull., Vol. 18, pp. 1258 (1973).

46. D. Arnush, K. Nishakawa, B. D. Fried, C. F. Kennel, and A. Y. Wong, AGARD Conference Proceedings #138, pp. 10-1, Edinburgh (1973).

47. T. K. Chu and H. W. Hendel, Phys. Rev. Lett., Vol. 29, pp. 634 (1972).

48. H. W. Hendel and J. T. Flick, Phys. Rev. Lett., Vol. 31, pp. 199 (1973).

49. T. K. Chu, S. Bernabic, and R. W. Motley, Phys. Rev. Lett., Vol. 31, pp. 211 (1973).

50. R. L. Stenzel, A. Y. Wong, D. Arnush, B. D. Fried, and C. F. Kennel, AGARD Conference Proceedings #138, pp. 4-1, Edinburgh (1973).

51. J. A. Fejer and E. Leer, "Bernstein Waves," Radio Sciences (1972).

52. F. W. Perkins, E. J. Valeo, and G. D. Thome, "Thermal Self-Focussing of Electromagnetic Waves in Plasmas" (submitted for publication).

53. J. A. Fejer, "Generation of Large Scale Field-Aligned Density Irregularities in Ionospheric Heating Experiments" (submitted for publication).

ADDITIONAL SOURCES

Proceedings of the IVORY CORAL 1973 Technical Review Meeting, Volume I: Theory, Contract N00014-70-C-0413, Stanford Research Institute, Menlo Park, Calif. (April 1973).

Proceedings of the PRAIRIE SMOKE II RF Measurements Data Workshop 22-23 June 1972, Contract N00014-70-C-0413, Stanford Research Institute, Menlo Park, Calif. (October 1972).

Proceedings of the PRAIRIE SMOKE III RF Measurements Data Workshop 31 October 1972, Contract N00014-70-C-0413, Stanford Research Institute, Menlo Park, Calif. (January 1973).